

First Principles Study of Some Si-based Type-II Clathrate Materials

by

Dong Xue, M.S.

A Dissertation

In

Physics

Submitted to the Graduate Faculty  
of Texas Tech University in  
Partial Fulfillment of  
the Requirements for  
the Degree of

DOCTOR OF PHILOSOPHY

Approved

Charles W. Myles  
Chair of Committee

Mahdi Sanati  
Vice-chair of Committee

Louis Grave de Peralta

Juyang Huang

Mark Sheridan  
Dean of the Graduate School

August, 2018

Copyright 2018, Dong Xue

## ACKNOWLEDGMENTS

First and foremost I would like to express my earnest gratitude to my distinguished Ph.D. advisor, Dr. Charles W. Myles, for his tremendous and unremitting guidance during my doctoral research time. I sincerely appreciate all his contributions of ideas, considerations, effort and care, which always encourage me and make me to have a wonderful study experience. Besides the good advice, smooth collaboration with Dr. Myles as well as our established friendships, I also deeply learn from my advisor that, how to behave as an honest and integrity person not only during scientific research work but also in the normal daily life.

I also must thank my vice-advisor who is Dr. Sanati since he has provided me for many fruitful discussions about clathrate research along with the excellent programming code (VASP), which serves as the most necessary computation tool throughout my research era.

Additionally, Dr. Louis Grave de Paralta, Dr. Juyang Huang and Dr. Thomas Gibson have contributed immensely to be my Ph.D. committee members.

I am also especially thankful for the Department of Physics and Astronomy at Texas Tech University, where I undergo the joy and enthusiasm associated with my teaching assistant experiences within the past years.

Lastly, I grateful acknowledge the allocation of many hours of computing time at the High Performance Computing Center of Texas Tech University.

## TABLE OF CONTENTS

<b>ACKNOWLEDGMENTS.....</b>	<b>ii</b>
<b>ABSTRACT.....</b>	<b>v</b>
<b>LIST OF TABLES.....</b>	<b>ix</b>
<b>LIST OF FIGURES.....</b>	<b>x</b>
<b>I. INTRODUCTION AND MOTIVATION.....</b>	<b>1</b>
1.1 Brief Introduction to Inorganic Clathrate Materials.....	2
1.2 Brief History of Thermoelectric Materials.....	5
1.3 The Outlook for Inorganic Clathrate as Thermoelectric Materials .....	7
<b>II. GOALS AND DESCRIPTION OF CURRENT WORK.....</b>	<b>11</b>
<b>III. COMPUTATIONAL APPROACH.....</b>	<b>16</b>
<b>IV. STRUCTURAL, ELECTRONIC AND VIBRATIONAL PROPERTIES OF BINARY CLATHRATE SYSTEM <math>A_xM_{136}</math> (A = ALKALINE METAL; M = GROUP IV ELEMENT; <math>0 \leq X \leq 24</math>).....</b>	<b>19</b>
4.1 Structural Properties.....	20
4.2 Electronic Properties.....	24
4.3 Vibrational Properties and Anharmonic Effects.....	28
4.4 Vibrational Anharmonic Effects in the Self-consistent Phonon Model.....	35
<b>V. ELECTRONIC PROPERTY AND PHONON ANHARMONICITY OF CLATHRATE <math>SI_{136-x}Ge_x</math>.....</b>	<b>40</b>
5.1 Structural Properties.....	40
5.2 Electronic Properties.....	42
5.3 Vibrational Properties and Anharmonic Effects.....	45
<b>VI. THE QHA-BASED MODE GRÜNEISEN PARAMETER ANALYSIS..</b>	<b>59</b>
6.1 Summar of Negative Thermal Expansion Studies.....	59
6.2 Discussion of Thermal Performance.....	61
<b>VII. ALLUMINIUM AND ALKALI-DOPED TERNARY AND QUATERNAR CLATHRATE.....</b>	<b>68</b>
7.1 Structural, Electronic and Vibrational Study on Al-substituted Ternary Clathrate Compounds.....	68

7.2 The Quaternary Clathrate Compound $\text{Cs}_8\text{Na}_{16}\text{Al}_{24}\text{Si}_{112}$ .....	78
<b>VIII. CONCLUSIONS.....</b>	<b>83</b>
<b>APPENDIX.....</b>	<b>88</b>
<b>BIBLIOGRAPHY.....</b>	<b>94</b>

## **ABSTRACT**

Two major thermoelectric effects were discovered early in the 19<sup>th</sup> Century. For some conductors, Seebeck (1821) discovered that, when the junction of two conductors is heated, a voltage drop across the junction is produced. This phenomenon is called the Seebeck Effect. Several years later, Peltier (1834) discovered that, for some conductors, when an electric current is passed through a junction of two conductors, a temperature gradient across the junction is produced. This phenomenon is called the Peltier Effect. Taken together, these two phenomena are called thermoelectric effects. It is now understood that these two effects are actually different manifestations of the identical physical process.

Thermoelectric effects have several practical applications. For example, thermoelectric generators, device refrigerators, and some temperature measurement devices operate the way they do because of thermoelectric effects. Because of their practical applications, it is desirable to develop thermoelectric materials for which the thermoelectric efficiency is as large as possible. A primary criterion for maximizing the thermoelectric (TE) efficiency of a material is that the material should have a high electrical conductivity like a metal and that it should also have a low thermal conductivity like a glass. A material which has both high electric conductivity and low thermal conductivity is said to satisfy the “phonon glass-electron crystal” (PGEC) criterion. A promising class of materials that satisfy the PGEC criterion for high thermoelectric efficiency is the semiconducting (or intermetallic) inorganic clathrate

compounds.

In my dissertation, the results of a systematic, theoretical and computational study of several different Type-II inorganic clathrate materials are presented and discussed. All of the first-principles calculations reported here are based on the Local Density Approximation (LDA) to Density Functional Theory (DFT). The Type-II clathrates were chosen for this work, since much less research attention has been given to those materials than for the Type-I clathrate materials. Specifically, my entire dissertation is focused entirely on Si-based Type-II clathrate materials. In this work, I describe the results of a systematic study of the structural, electronic, vibrational and thermodynamic properties of several different Si-based Type-II compounds.

Starting with the “cage-structured” framework in the empty clathrate lattice, I discuss the results of a systematic theoretical study of some of the properties of the compounds, within which various alkali metal atom impurities are encapsulated in the cages of the Si-based Type-II clathrate lattice. The unique structural characteristics of the “guest-free” clathrate framework can lead to a material with very good electrical conductivity. Further, a small lattice thermal conductivity can be achieved by placing various alkali metal atom impurities (“guests”) in the cages present in the Type-II Si framework. This low thermal conductivity can be achieved because the low-lying vibrational (“rattling”) modes of the guests can interfere with and suppress the heat-carrying acoustic phonons of the Si Type-II lattice.

For the binary clathrate compounds  $A_x\text{Si}_{136}$  ( $A = \text{Alkali metal}$ ;  $0 < x \leq 24$ ), my results predict that there should be a lattice contraction for  $0 < x \leq 8$  and a lattice

expansion for  $9 < x \leq 24$ . These results are in quantitative agreement with X-ray diffraction (XRD) data. In addition, my LDA-derived results predict an “off-center” displacement of the Na guest placed inside the 28 atom (hexakeidacahedron) cage of  $\text{Na}_x\text{Si}_{136}$ . This off-center displacement is due to the presence of a dynamically unstable “Mexican-hat”- shaped effective potential energy in  $\text{Na}_x\text{Si}_{136}$  (for  $x = 4, 8, 24$ ). Physically, this unusual shape is due to a strong anharmonic effective potential for the Na guest (“rattler”).

A motivation for studying binary alloy mixtures of Type-II Si and Ge clathrates (with no guests in the cages) is the fact that there have been several first-principles theoretical and experimental studies of pristine  $\text{Si}_{136}$  as well as a smaller number of studies of pristine  $\text{Ge}_{136}$ . I have studied several aspects of the Type-II Si-Ge binary alloy framework  $\text{Si}_{136-x}\text{Ge}_x$  ( $x = 8, 32, 40, 96, 104, 128$ ). Among the interesting predictions that my calculations have shown is that, for some temperatures and compositions  $x$ , the thermal expansion coefficient is negative. This negative thermal expansion (NTE) behavior in  $\text{Si}_{136-x}\text{Ge}_x$  is correlated with anharmonic effects in the phonon modes. I have derived these results using the quasi-harmonic approximation (QHA). The results of this study find that, for low concentrations of Ge ( $x \leq 40$ ), the weighted Grüneisen parameter ( $\gamma(T)$ ) governing the NTE phenomenon is strongly effected by transverse acoustic phonons (TA). Specifically, I have found that all of the vibrational modes in the TA branch have a negative mode Grüneisen parameter (MGP). On the other hand, as  $x$  increases ( $x = 96, 104, 128$ ), the number of Ge-Ge bonds in  $\text{Si}_{136-x}\text{Ge}_x$  also increases. I also find that the NTE effect disappears for low

concentration of Si.

Motivated by recent experimental studies of the Type-II clathrate compounds  $(\text{Cs,Rb})_8\text{Al}_8\text{Si}_{128}$  and  $\text{Cs}_8\text{Na}_{16}\text{Al}_{24}\text{Si}_{112}$ , I have also carried out a theoretical and computational study of some of the properties of these two materials. Among the results are predictions of the temperature-dependent isotropic mean square displacement amplitudes ( $U_{\text{iso}}$ ) for Cs guests in those materials. In comparison with XRD data for those compounds, my predictions slightly overestimate  $U_{\text{iso}}$  in comparison with the results of XRD experiments. This indicates that a temperature-dependent quartic anharmonicity needs to be included for the Cs guest vibrational modes. Further, the reduced lattice thermal conductivity obtained from my LDA-calculations is likely to be caused by an underestimation of the phonon mean free path, in these quaternary clathrate compounds.

**LIST OF TABLES**

4.1	LDA-calculated quasiactivation energy and Fermi level of filled clathrate $\text{Na}_x\text{Si}_{136}$ ( $x = 8, 16$ ), $\text{Na}_{16}\text{Rb}_8\text{Si}_{136}$ and $\text{K}_{16}\text{Rb}_8\text{Si}_{136}$ * denotes the work done by [27].....	27
4.2	The fitting parameters of guest-host interaction energy potentials for $\text{Na}_x\text{Si}_{136}$ ( $x = 4, 8, 12$ ), $\text{K}_x\text{Si}_{136}$ , $\text{Rb}_x\text{Si}_{136}$ ( $0 < x < 24$ ). The isotropic harmonic spring constant $K_{\text{iso}}$ and the lowest order anharmonic interaction constant $\epsilon_{\text{iso}}$ are listed here. The estimated low-lying anharmonic vibrational frequency $\Omega(T = 300\text{K})$ is compared to the phonon frequency $\omega_{\text{ph}}$ calculated by VASP in the harmonic approximation and $(K_{\text{iso}}/M)^{1/2}$ .....	34
5.1	Comparison of mode Grüneisen parameters between experimentally studied $\text{Na}_1\text{Si}_{136}$ clathrate along with diamond phase silicon [80,82] and theoretically explored $\text{Si}_{136-x}\text{Ge}_x$ ( $8 \leq x \leq 128$ ).....	57
7.1	Equation of State (EOS) parameters obtained for filled ternary clathrate $(\text{Rb,Cs})_8\text{Ga}_8\text{Si}_{128}$ and $(\text{Rb,Cs})_8\text{Al}_8\text{Si}_{128}$ .....	70
7.2	LDA-performed rattling mode $\omega$ , group velocity of TA phonons $v_{\text{TA}}$ , group velocity of LA phonons $v_{\text{LA}}$ , sound velocity $v_s$ , phonon mean free path $\lambda$ and lattice thermal conductivity $\kappa_L$ for filled ternary clathrate $(\text{Rb,Cs})_8\text{Al}_8\text{Si}_{128}$ , $\text{Cs}_8\text{Na}_{16}\text{Si}_{136}$ and $(\text{Cs,Rb})_8\text{Si}_{136}$ .....	77
7.3	The occupancy of framework atoms (Al,Si) on different Wyckoff sites including $8a, 32e$ and $96g$ . The LDA-determined structural properties such as lattice constant, bulk modulus and energy difference between the lowest total energy of the energetically stable configuration (the second row) per unit cell and the total energy of other configuration.....	79
7.4	Comparison of nearest-neighbor distances obtained by VASP with that of experimental work for $\text{Cs}_8\text{Na}_{16}\text{Al}_{24}\text{Si}_{112}$ [100].....	80

**LIST OF FIGURES**

4.1	Predicted $x$ dependence of the Lattice Constants for the Type-II Clathrate-Based Compounds $A_xSi_{136}$ ( $A = Na, K, Rb, Cs$ ; $0 \leq x \leq 24$ ).....	22
4.2	Predicted $x$ dependence of the lattice constant for Na-containing clathrate $Na_xM_{136}$ ( $M = Si, Ge$ or $Sn$ , $0 \leq x \leq 24$ ).....	24
4.3	Illustration of electronic density of states in the lower portion of conduction band, with respect to clathrate $Na_8Si_{136}$ and $Na_{16}Si_{136}$ .....	26
4.4	Electronic density of states (DOS) of clathrate system $Na_xSi_{136}$ , where $x = 8, 12, 16$ . The Fermi energy levels ( $E_F$ ) are denoted by dotted lines.....	27
4.5	The predicted vibrational modes for $Na_4Si_{136}$ . The number in parentheses is the mode obtained from inelastic neutron scattering (INS) experiments [46].....	29
4.6	The calculated, isotropic, Mexican hat shaped potential energy curves for Na vibrations in the large 28-atom cages in the clathrate system $Na_xSi_{136}$ ( $x = 4, 8, 24$ ). $X$ represents the motion direction with respect of the Na atom.....	32
4.7	DFT-calculated “Off-centering” displacement of Na in $Si_{28}$ cage as a function of Na composition inside $Na_xSi_{136}$ ( $x = 4, 8, 12, 16$ ), given by DFT prediction and XRD determination [60].....	33
4.8	The potential energy curves for alkali atoms $K, Rb, Cs$ inside Si framework. $X$ and $Z$ represents the motion direction with respect to alkali atom.....	35
4.9	Anharmonic rattling frequency of guest vibrations in a $Si_{28}$ cage as a function of temperature for the filled binary clathrates $Rb_8Si_{136}$ and $Na_{24}Si_{136}$ .....	37

5.1	LDA-determined lattice parameter trends (red squares) as a function of Ge mole fraction for $[\text{Si}_{1-x}\text{Ge}_x]_{136}$ , in comparison with XRD data (open circles). The dashed line drawn for LDA data is from linear fit procedure and acts as a guide for the eye.....	41
5.2	Comparison of predicted band gap (red squares) and experimentally obtained results (open circles) for $\text{Si}_{1-x}\text{Ge}_x]_{136}$ ( $0 < x < 136$ ) [115]. The dashed line drawn acts as a guide for the eye. Mode Grüneisen parameters of TA (1) and LA phonons at L-point of $\text{Si}_{40}\text{Ge}_{96}$ .....	42
5.3	Electronic band structures of $\text{Si}_{128}\text{Ge}_8$ , where the zero of energy is set to be the valence band maximum at L point.....	43
5.4	Calculation of electronic density of states for $\text{Si}_{136-x}\text{Ge}_x$ ( $x = 8,40,104$ ), zero energy is set to be at the maximum of valence band. Mode Grüneisen parameters of TA (1) and LA phonons at X-point of $\text{Si}_{104}\text{Ge}_{32}$ .....	45
5.5	Dispersion relations of $\text{Si}_{136-x}\text{Ge}_x$ ( $x = 8,40,104$ ) obtained from VASP.....	46
5.6	Variation of fractional change in mode frequency with respect to TA(1) phonon branch along $\Gamma$ -L direction, as a function of fractional change in volume.....	48
5.7	Predicted mode Grüneisen parameters in the vicinity of $\Gamma$ -point belonging to TA(1) and LA phonon branch, in the case of $\text{Si}_{128}\text{Ge}_8$ and $\text{Si}_8\text{Ge}_{128}$ respectively. Results are given through finite difference method, while solid and dotted lines represent best linear fit of first-principle data.....	50
5.8	Low-frequency dispersion relation curves of $\text{Si}_{128}\text{Ge}_8$ and $\text{Si}_8\text{Ge}_{128}$ along L- $\Gamma$ -X line, corresponding to optimized geometry (solid line) and dilated configuration (dotted line). Meanwhile, LDA-calculated results on vibrational density of states are also shown. Circled area denotes longitudinal acoustic phonon branch as well as transverse acoustic phonon branch with double degeneracy.....	51
5.9	LDA-calculated specific heat and summation over mode-dependent heat capacity $C_{V,i}(q)$ .....	53

5.10	Predicted weighted Grüneisen parameter regarding to transverse acoustic phonons ( $\lambda_{TA}(T)$ ) and contribution of all phonon modes ( $\lambda(T)$ ), in terms of temperature for $\text{Si}_{136}$ .....	54
5.11	The predicted Mode Grüneisen Parameters for TA (1) and LA phonons confined at the Brillouin zone boundary and center, as a function of Si content $x$ .....	56
5.12	DFT-predicted Grüneisen parameters of $\text{Si}_{104}\text{Ge}_{32}$ , $\text{Si}_9\text{Ge}_{40}$ , $\text{Si}_{40}\text{Ge}_{96}$ , $\text{Si}_{32}\text{Ge}_{104}$ .....	58
6.1	The vibrational entropy at four characteristic temperatures for alloy clathrate $\text{Si}_{128}\text{Ge}_8$ .....	64
6.2	The predominant temperature-dependent contributions to Gibbs free energy per atom, at four characteristic temperatures for alloy clathrate $\text{Si}_{128}\text{Ge}_8$ .....	65
6.3	Predicted vibrational free energy including zero-point contribution for $\text{Si}_{136}$ , subjected to the range 10 ~ 400 K.....	66
6.4	Predicted vibrational entropy at $T = 60\text{K}$ and $T = 120\text{K}$ for $\text{Si}_{104}\text{Ge}_{32}$ .....	67
7.1	Predicted LDA-calculated phonon dispersion curves of $\text{Cs}_8\text{Al}_8\text{Si}_{128}$ .....	72
7.2	Predicted LDA-calculated phonon dispersion curves of $\text{Rb}_8\text{Al}_8\text{Si}_{128}$ .....	73
7.3	Predicted low-frequency vibration spectrum of $\text{Cs}_8\text{Al}_8\text{Si}_{128}$ , $\text{Rb}_8\text{Al}_8\text{Si}_{128}$ and $\text{Al}_8\text{Si}_{128}$ .....	73
7.4	“Avoided-crossing” effect due to encapsulated Cs introduced into $\text{Al}_8\text{Si}_{128}$ . Solid line shows low-frequency dispersion relation curves of $\text{Cs}_8\text{Al}_8\text{Si}_{128}$ along $\Gamma$ -X direction. Dotted lines give dispersion relation curves of $\text{Al}_8\text{Si}_{128}$ .....	76

- 7.5 Theoretically and experimentally estimated isotropic atomic displacement parameters ( $U_{\text{iso}}$ ) of Cs in 28-cage. The open symbols represent the data corresponding to Cs vibration in  $\text{Cs}_8\text{Na}_{16}\text{Ge}_{136}$  [99]. The solid symbol denotes the measured value of  $U_{\text{iso}}$  regarding to Cs rattling in  $\text{Cs}_8\text{Na}_{16}\text{Al}_{24}\text{Si}_{112}$ .....81
- 7.6 Predicted lattice thermal conductivity as a function of Al occupancy on 96g Wyckoff site. The dotted line is used for comparison.....82

## CHAPTER I

### INTRODUCTION AND MOTIVATION

Developing new materials which meet given specifications is difficult. For thermoelectrics, this is further complicated due to seemingly contradictory requirements for such materials. A good thermoelectric material should have a high Seebeck coefficient ( $S$ ), a high electrical conductivity ( $\sigma$ ), similar to that of a metal, and low thermal conductivity ( $\kappa$ ), similar to that of a glass. As a result, there is a strong interest in the development of a fundamental understanding of potential thermoelectric materials, in using theory and modeling in identifying promising candidates, and in suggesting avenues for optimization. Over the last several years, many inorganic semiconductor clathrates based on Si, Ge, and Sn have been synthesized and proposed for use as thermoelectric materials.

In this dissertation, I report the results of a systematic first-principles, theoretical and computational study of the electronic, vibrational, and thermal properties of various Type-II Si-based clathrates. Specifically, I present the results of such a study for some of the guest-atom-containing binary, ternary and quaternary Type-II clathrate compounds as well as of some of the alloy mixtures Si and Ge Type-II materials. The specific materials that were chosen for this work are the compounds  $A_x\text{Si}_{136}$  ( $A = \text{Na}, \text{K}, \text{Rb}, \text{Cs}; 0 < x \leq 24$ ),  $(\text{Cs}, \text{Rb})_8\text{Al}_8\text{Si}_{128}$  and  $\text{Cs}_8\text{Na}_{16}\text{Al}_{24}\text{Si}_{112}$  and the alloy material  $\text{Si}_{136-x}\text{Ge}_x$  ( $x = 8, 32, 40, 96, 104, 128$ ).

## 1.1 Brief Introduction to Inorganic Clathrate Materials

X-ray diffraction studies [1] of the gas hydrate clathrate  $\text{SO}_2(\text{H}_2\text{O})_6$  material have determined the structure of its cubic unit cell. It contains 48 oxygen atoms which form a total of 8 large voids, at the centers of which are eight  $\text{SO}_2$  molecules. The lattice for this material is an example of the geometry of the clathrate configuration. Specifically, the empty clathrate lattice framework is constructed by face-sharing polyhedra which are either dodecahedra (20-atoms), tetrakaidecahedra (24-atoms) or hexakeidacahedra (28-atoms). Each of these polyhedra is capable of housing an encapsulated impurity (or “guest”) atom. In other words, clathrates are “host-guest” complexes in which the guest is in a cage formed by a lattice of host atoms.

In addition to the hydrate clathrates, there also exist several types of inorganic clathrate materials based on Si, Ge, or Sn atoms. Over the past several years, many of the Type-I and Type-II inorganic clathrate compounds have received considerable attention from both the theoretical and experimental points of view [2-6]. Additionally, several first-principles theoretical predictions of the properties of Type-VIII inorganic clathrates [7-11] have been recently reported. Further, some recent reports of the successful synthesis of the Type-VIII clathrate compounds  $\text{Ba}_8\text{Ga}_{16}\text{Ge}_{30}$ ,  $\text{Eu}_8\text{Ga}_{16}\text{Ge}_{30}$ ,  $\text{Sr}_8\text{Ga}_x\text{Si}_{46-x}$  and etc. have been published [12,13]. Other types of crystalline inorganic clathrates including Type-III and Type-IX are briefly discussed in Refs. [14,15].

A description of the crystal structures of the Type-I and Type-II clathrates is as

follows. The unit cell of the pure Type-I clathrate phase contains 46 atoms and the lattice is a simple cubic (SC) structure formed by linking together cages of two different sizes. The small cage contains 20 atoms and is in the shape of a pentagonal dodecahedron ( $5^{12}$ ), while the large cage contains 24 atoms and is in the shape of a tetrakaidecahedron ( $5^{12}6^2$ ). To form the SC lattice framework, 20-atom cages and 24-atom cages are connected periodically in a 2 to 6 ratio. One of the best representatives of Type-I clathrate of recent intensive interest is  $\text{Na}_8\text{Si}_{46}$  [16-20], in which all cages of entire framework are fully occupied by Na “guest” impurities. The center of each dodecahedron cage is denoted in the Wyckoff symmetry notation as a  $2a$  lattice site. The cage size in comparison to the size of a Na atom allows a single Na to reside at this site. The center of each tetrakaidecahedron cage is denoted in the Wyckoff symmetry notation as a  $6d$  lattice site. Using Wyckoff notation to describe the arrangement of the crystallographic positions of the Si host atoms on the lattice framework, it is found that they are arranged at sites  $24k$ ,  $16i$  and  $6c$ .

In the empty framework of the Type-II clathrate, the unit cell of the full cube contains 136 atoms. The lattice structure is face centered cubic (FCC), with a primitive cell that has 34 Si, Ge, or Sn atoms. In analogy to the Type-I material  $\text{Na}_8\text{Si}_{46}$ , the Type-II clathrate compound  $\text{Na}_x\text{Si}_{136}$  ( $0 < x \leq 24$ ) has recently received considerable attention, due to the fact that the Na composition ( $x$ ) can be varied by using a thermal decomposition process [21,22]. For this material, the Si atoms in the FCC unit cell are distributed on the vertices of 4 pentagonal dodecahedra (20 atom cages) and 2 hexakaidecahedra (28 atom) cages. In the FCC primitive cell, the 20-atom cages and

28-atom cages are combined in a 4 to 2 ratio. The pure Type-II clathrate  $\text{Si}_{136}$  lattice is an open framework, with a “cage-structured” lattice in which the cages are  $\text{sp}^3$  covalently bonded to each other. All of the Si cages are capable of trapping selected “guest” atoms and the choice and concentration of the guests are often used to “tune” the material properties.

In the synthesis of these materials, the guest atoms chosen have mostly been alkali metal or alkaline earth atoms. Gryko et al. have reported the successful synthesis of guest-free  $\text{Si}_{136}$  by the continuous removal of Na from  $\text{Na}_x\text{Si}_{136}$  ( $x > 10$ ) single crystals [23]. In  $\text{Na}_x\text{Si}_{136}$ , Nolas et al. have found that Na guest atoms encapsulated inside  $\text{Si}_{20}$  cages occupy the cage centers, whose positions are in Wyckoff  $16c$  sites for a range of guest composition values ( $8 < x \leq 24$ ) [22]. Further, in the case of  $\text{K}_{17.8}\text{Si}_{136}$ , when the potassium guests are placed inside the  $\text{Si}_{28}$  cages, they occupy the sites denoted in Wyckoff notation as  $8b$  sites [24].

By combining first-principles predictions with relevant experimental data [22], in this dissertation, among other properties, we examine how the size difference between the guest atoms inside the  $\text{Si}_{28}$  cages might effect the position of the impurity near the cage center. Specifically, we find that, for a small guest atom such as Na in the 28-atom cages in Type-II Si clathrate, there is a large “excess” volume which will tend to allow the guest to displace to an “off-center” position. Further, we find that such predicted “off-center” displacement of the Na atoms in the  $\text{Si}_{28}$  cages is not apparently significantly affected by changing the guest composition ( $x$ ) in  $\text{Na}_x\text{Si}_{136}$  ( $0 < x < 24$ ). Our predictions of such off-center Na guests in this material are in fair agreement with

the results of recent X-ray diffraction (XRD) measurements [25].

## 1.2 Brief History of Thermoelectric Materials

Thermoelectric (TE) devices fabricated from inorganic clathrate materials are of potential practical importance because of at least two factors. First, it is important that significant attention be paid to environmental conservation world-wide. This motivates technological developments which seek alternative energy resources, which can partially replace fossil fuels. Second, as a promising candidate for TE applications, the clathrate compounds potentially have the ability to convert waste heat to electric energy in a more efficient way than traditional TE materials. Specifically, these materials can optimize the Seebeck effect and they also satisfy the “phonon glass-electron crystal” (PGEC) scheme for thermoelectric materials, which was proposed by Slack [31].

A number of studies have shown that a measure of high TE performance in the inorganic clathrate materials focuses on increasing the dimensionless figure-of-merit parameter ( $ZT$ ) through significantly minimizing the thermal conductivity ( $\kappa$ ) [3,32-35]. To enhance the TE characteristics of a pure clathrate material based on a Group IV element, a “rattler” guest impurity may be inserted and trapped in the cages of these materials. Then, the low-lying vibrational modes of the guests tend to interfere with the heat-carrying acoustic modes of the lattice framework, which can lead to reduced thermal conductivity compared to that of empty clathrate lattice. Theoretical

calculations by Dong, Sankey and coworkers examined the transport features of the Type-I clathrate  $\text{Sr}_6\text{Ge}_{46}$ , which was found to exhibit extremely low lattice thermal conductivity  $\kappa$  ( $1.64 \pm 0.24 \text{ W M}^{-1} \text{ K}^{-1}$ ) at room temperature [3]. That value is approximately reduced by two orders of magnitude in comparison with that of the amorphous-phase analogue of *d*-Ge ( $114 \pm 3 \text{ W M}^{-1} \text{ K}^{-1}$ ). The experimentally determined room-temperature  $\kappa$  of  $\text{Sr}_6\text{Ge}_{46}$  has been reported is  $0.89 \text{ W M}^{-1} \text{ K}^{-1}$  [36, 37].

Besides the capability of converting waste heat into electricity, TE materials can potentially also play essential roles in electronic refrigeration. An example of this is that the cooling of computer processors fabricated by TE materials results in computational speed gains of 30-200%. The achievement of this improved speed is attributable to the complementary metal oxide semiconductor (CMOS) technology employed when manufacturing the processor [38].

The thermoelectric effect involves heat and electric transport processes which are irreversible. Guided by Onsager's approach to transport theory, one can model TE effects by considering the heat flux density  $\mathbf{Q}$  and the non-neutral particle flux density  $\mathbf{J}$ , both of which are recognized as two kinds of "generalized forces". Taking the gradient of the inverse of temperature and the gradient of the electrochemical potential into account, Callen [39] has developed a generalization of the Onsager theory through a mathematical derivation of  $\mathbf{Q}$  and  $\mathbf{j}$  with the following results:

$$\begin{aligned}\vec{j} &= \sigma(\vec{E} - S\vec{\nabla}T) \\ \vec{Q} &= \sigma S T \vec{E} - \kappa \vec{\nabla}T\end{aligned}\tag{1.1}$$

Here,  $\mathbf{j}$  is the particle flux density per unit electric field  $\mathbf{E}$ . The gradient of

electrochemical potential ( $V$ ) has been incorporated into an analogous definition of  $E$ , assuming an that an electromotive force ( $V$ ) is responsible for producing the  $E$  field in an isothermal system. The thermal conductivity  $\kappa$  is associated with the heat current density  $Q$  per unit temperature gradient, in the absence of an electric field  $E$ . Then, defining the Seebeck coefficient  $S$  allows one to recognize that a temperature gradient can yield a similar electromotive force, in addition to  $E$ . From the above relations, the Peltier coefficient  $\Pi$  can be derived by taking into account the form  $Q = TSj$ , in the presence of zero temperature gradient. Overall, the Seebeck effect and Peltier effect are related in a unified equation of the form:  $\Pi = ST$

### 1.3 The Outlook for Inorganic Clathrates as Thermoelectric Materials

It is worth of discussing some recent developments in the field of TE materials in more detail. As mentioned above, the theoretical goal of improving the energy conversion efficiency of TE materials is to increase the unitless figure of merit ( $ZT$ ). Here,  $T$  is the absolute temperature and  $Z$  is given by  $Z = S^2 \sigma / \kappa$ , whereas  $\sigma$  denotes the electrical conductivity and  $\kappa$  remains to be the thermal conductivity,  $S$  is the Seebeck coefficient. It has been reported that the largest  $ZT$  obtained at room temperature is close to 1.54 in the superlattice  $\text{Bi}_2\text{Te}_3/\text{ZrB}_2$  films, which is the best reported TE performance up to the present [40]. There are a wide variety TE materials which have been synthesized from various chemical substances. These range from low-dimensional materials, to bulk materials, to novel bulk compounds such as the

clathrates. They also include half-Heusler intermetallic materials and complex chalcogenides [41].

Researchers searching for high-performance TE materials have discovered that the best TE material should have very low, glass-like thermal conductivity along with a very high, crystal-like electrical conductivity. This idea was initially proposed by Slack, who named it the “phonon glass electron crystal” (PGEC) concept [31]. Therefore, when designing good TE materials, it is necessary to minimize the thermal conductivity linked with the heat conduction processes and to simultaneously maintain high electrical conductivity along with a large thermopower factor.

Myles et al. have studied the Type-I semiconducting clathrate  $\text{Cs}_8\text{Ga}_8\text{Sn}_{38}$ . They have found that loosely bound Cs guest atoms in the “over-sized” (24-atom) cages in that material can produce very “low-lying” rattling vibrational modes, which can scatter the heat-carrying acoustic phonons of the host [43]. It is the interaction between the guest atom vibrations and the acoustic modes of the host framework that potentially takes part in reducing the thermal conductivity ( $\kappa$ ). Specifically, many semiconducting clathrates possess a low lattice thermal conductivity ( $\kappa_L$ ) that controls the heat conduction properties, while they also possess an extremely small electronic thermal conductivity ( $\kappa_E \ll \kappa_L$ ) so that the heat conduction properties are controlled by the lattice thermal conductivity.

Compounds based on the Type-II inorganic clathrates have not been as extensively studied, experimentally or theoretically, as those of the Type-I variety. Many compounds of the Type-I clathrate family have been synthesized [44-46].

Specifically, K. Kishimoto, et al. prepared  $\text{Sr}_8\text{Al}_x\text{Ga}_{16-x}\text{Si}_{30}$  and  $\text{Si}_{46-x}\text{P}_x\text{Te}_8$  ( $0 \leq x \leq 16$ ) through powder metallurgy [47-50]. The synthesis of the compounds  $\text{Ba}_{8-x}\text{Si}_{46}$ ,  $\text{Si}_{46-x}\text{P}_x\text{Te}_8$ ,  $\text{Ba}_8\text{Si}_{46}$ ,  $\text{Sn}_{24}\text{P}_{19.3}\text{I}_8$ ,  $\text{Sn}_{24}\text{As}_{19.3}\text{I}_8$  and others has been described in references [51-53].

Several Type-II inorganic clathrate compounds have been synthesized and measurements have been reported of their structural, vibrational, and electrical transport properties. For example, Nolas and Beekman have produced  $\text{Na}_8\text{Si}_{36}$  via oxidation of  $\text{Na}_4\text{Si}_4$ , in the form of both single crystals and microcrystalline samples [29]. In such experimental studies, the vibrations of the guest atom “rattlers” have also been extensively studied. For instance, the structural stoichiometry of the ternary compounds of the form  $\text{A}_8\text{X}_{16}\text{M}_{120}$  and  $\text{A}_8\text{X}_8\text{M}_{128}$  has attracted much attention. Here, A is a Column II alkaline earth atom, such as Ba and Sr, which are introduced as rattling guests in the cages formed by the Column IV atoms M (Si, Ge, Sn) on the host lattice. Further, A is a Column I alkali metal atom (Na, K, Rb, Cs) and X is an atom from Column III (Al, Ga). The purpose of substituting Al or Ga for some of the Si framework atoms is to compensate for the excess valence electrons which are donated to the material conduction bands by the alkali or alkaline earth atom guests. Making such substitutions causes the material to remain semiconducting.

Because optimizing the TE performance of the clathrate materials is focused on the PGEC criteria, a series of Type-I Si- Ge- and Sn-based semiconducting clathrates have been synthesized and thoroughly studied in order to find materials with low lattice thermal conductivity ( $\kappa_L$ ) [3, 26, 36, 54-55]. Nolas, Gryko, and Myles et al.

have reported experimental and theoretical studies of the transport properties of the Type-I clathrate compounds  $\text{Sr}_8\text{Ga}_{16}\text{Si}_{30}$ ,  $\text{Ba}_8\text{Al}_{16}\text{Si}_{30}$ ,  $\text{Ba}_8\text{Ga}_{16}\text{Ge}_{30}$ ,  $\text{Sr}_8\text{Ga}_{16}\text{Ge}_{30}$ ,  $\text{Eu}_8\text{Ga}_{16}\text{Ge}_{30}$ ,  $\text{Cs}_8\text{Sn}_{44}$ ,  $\text{K}_8\text{Ga}_8\text{Sn}_{38}$ , and  $\text{Ba}_8\text{Ga}_{16}\text{Sn}_{30}$  [37,56-59]. They have also measured the temperature-dependent lattice thermal conductivity of several of these Type-I materials. For comparison, results for the measured temperature-dependent thermal conductivity in amorphous  $\text{SiO}_2$  was also presented in their study. The results of this study show that the thermal conductivity of the n-type single crystals of  $\text{Ba}_8\text{Al}_{16}\text{Si}_{30}$ ,  $\text{Ba}_8\text{Ga}_{16}\text{Ge}_{30}$ ,  $\text{K}_8\text{Ga}_8\text{Sn}_{38}$ , and  $\text{Sr}_8\text{Ga}_{16}\text{Si}_{30}$  exhibit a  $T^{-1}$  dependence on temperature, which is an indication of the fact that phonon scattering is dominated by Umklapp processes.

## CHAPTER II

### GOALS AND DESCRIPTION OF CURRENT WORK

A number of Type-II inorganic clathrate compounds have been synthesized. However, for most of these materials, very little is known, experimentally or theoretically, about their electronic, vibrational, structural, thermal or transport properties. The fact that some of these clathrates have the potential to be excellent thermoelectric materials is a strong motivation for a systematic theoretical and computational investigation of such materials. A major motivation for my dissertation work comes from the fact that the cage-like lattice framework in these materials contains voids capable of housing different alkali metal or alkaline earth guest atoms. Altering the concentration of guest atoms as well as the species of the guest atoms allows the systematic tuning of the various clathrate material properties.

One goal of my first-principles computational study is to try to provide theoretical predictions which can be compared with experimental measurements, so that the thermoelectric properties of some of these materials can be better understood. Our predictions of the composition dependence of the lattice constant in  $A_x\text{Si}_{136}$  ( $A$  = alkaline metal atom;  $0 < x \leq 24$ ) correlate well with recent XRD observations, which have shown that the lattice framework contracts as  $x$  increases for  $0 < x < 8$  and subsequently expands as  $x$  increases for  $8 < x < 24$ . Our calculations have shown that this can happen only if, as  $x$  is increased, the Na atoms first occupy all of the  $\text{Si}_{28}$  cages before they begin to occupy the smaller  $\text{Si}_{20}$  cages. Further, as is

discussed in a later chapter, our predicted “off-center” displacement of the Na guests in the 28 atom (hexakeidecahedron) cages in  $\text{Na}_x\text{Si}_{136}$  ( $0 < x < 24$ ) has been confirmed in X-ray diffraction (XRD) measurements [25,60]. Also, our predictions for the temperature dependent atomic displacement parameters  $U_{\text{iso}}$  compare favorably with XRD data for the quaternary clathrate compound  $\text{Cs}_{16}\text{Na}_8\text{Al}_{24}\text{Si}_{112}$ . Another goal of my work is to utilize first principles computational methods to systematically investigate the details of the structural, electronic, vibrational, thermal and transport properties of several of these Type-II Si-based clathrates. As is also discussed in a later chapter, my primary computational tools for this investigation are based on density functional theory (DFT) within the local density approximation (LDA).

As also discussed later, I have also used the quasiharmonic approximation (QHA) scheme combined with the finite difference method (FDM) to study the anharmonic vibrational properties of some of these materials. Specifically, I have focused on using these methods to study both the microscopic and total Grüneisen parameter trends for various clathrate materials. For some cases, I have also calculated the lattice thermal conductivity including these anharmonic effects. Specifically, I have used these methods to study these effects in the Type-II Si-Ge alloy framework and in the compound  $\text{Cs}_{16}\text{Na}_8\text{Al}_{24}\text{Si}_{112}$ . For the latter material, underestimation on its predicted thermal conductivity allows us to reconsider validity of primitive model, whereas the phonon mean free path needs to be recalculated from phonon lifetime rather than relying on nearest neighbouring distance between rattler impurity (Cs).

As already stated, the reason that the inorganic clathrate compound family is of

great thermoelectric importance is that these compounds can potentially combine a low, glass-like thermal conductivity with both a high electric conductivity and a large Seebeck coefficient. That is, these clathrates are prospective thermoelectric materials, because their ability to convert a temperature gradient into electric power can be enhanced by the judicious introduction of guest atoms into the lattice cages. In fact, it is this fascinating guest-host structure that makes the clathrates attractive and also different from other, traditional thermoelectric materials [90-95].

Another interesting clathrate system with very interesting physics is the alloy  $\text{Si}_{136-x}\text{Ge}_x$  ( $x = 8, 32, 40, 96, 104, 128$ ) without “rattling” guests. Another portion of my dissertation work has concentrated on studying the effects of phonon anharmonicity in this alloy. Specifically, my calculations predict that these anharmonic effects give rise to a negative thermal expansion (NTE) at low temperatures. Also, my predictions on temperature profiles of overall Grüneisen parameters as a function of Ge composition  $x$  suggest that, the increased number of Ge-Ge bond might correlates to the vanishingly small NTE phenomenon.

Another part of my dissertation focuses on the binary clathrate system  $\text{A}_x\text{Si}_{136}$  ( $\text{A} = \text{alkali metal atom}; 0 < x \leq 24$ ). In particular, I have carried out a systematic theoretical and computational study of the structural, electronic, vibrational and thermal properties of these materials. As previously mentioned, this system shows an unusual lattice response to filling the polyhedron cages of the Si framework with alkali metal atoms and my calculations are in good agreement with these observations. However, in addition to these interesting results for  $\text{Na}_x\text{Si}_{136}$  ( $x = 8, 16$ ), I have also

performed calculations focusing on the  $x$  dependence of the quasiaction energy ( $\Delta E$ ) between the adjacent peaks in the DFT-calculated electronic density of states (EDOS). One of the most intriguing features of the EDOS is that my calculations predict that the Fermi energy level ( $E_F$ ) increases with increasing composition ( $x = 8, 12, 16$ ) of Na. Further, in my study of the “rattling” vibrational properties of these binary materials, I have found that the quartic anharmonic effects are gradually weakened as the guest atom mass is raised for the fixed  $x$ . Specifically, using an LDA-calculated guest-host potential energy function, I predict that, for the smaller mass guest atoms, the guest vibrations in these materials should have a relatively large fourth-order anharmonic potential coefficient  $\epsilon_{\text{iso}}$ .

The remaining part of my dissertation is devoted to a systematic theoretical and computational investigation of some selected Al-substituted ternary and quaternary clathrate compounds. Specifically, for this portion of my work, I have chosen some compounds  $(\text{Cs}, \text{Rb})_8\text{Al}_8\text{Si}_{128}$ ,  $\text{Al}_8\text{Si}_{128}$ ,  $\text{Cs}_{16}\text{Na}_8\text{Al}_{24}\text{Si}_{112}$  and I have focused on calculations of their structural, vibrational and thermal properties. My results for the vibrational dispersion relations of the ternary compound  $(\text{Cs}, \text{Rb})_8\text{Al}_8\text{Si}_{128}$  predict that the Rb rattling mode frequency is about 23.8% smaller than that of Cs, which is likely due to the fact that the Rb guest atom is only weakly bound in the 28-atom framework cages. Further, after having placed Al atoms on the framework sites suggested by experimental XRD data [80], my DFT calculations for the optimized geometry of  $\text{Cs}_{16}\text{Na}_8\text{Al}_{24}\text{Si}_{112}$  predict isotropic atomic displacement parameters at room temperature which is slightly higher than the measured results.

Accordingly, this small overestimation is anticipated to relate to temperature-dependent rattling frequency and small nominal composition deviation from refined data of  $\text{Cs}_{16}\text{Na}_8\text{Al}_{24}\text{Si}_{112}$  framework.

## CHAPTER III

### COMPUTATIONAL APPROACH

All of the first-principles calculations reported here are based on the Local Density Approximation (LDA) to Density Functional Theory (DFT). For most of my calculations, the Vienna *ab-initio* Simulation Package (VASP) [102-104] has been used and I have employed the Ceperley-Alder [108] exchange-correlation potential along with pseudo-potentials obtained using the projector augmented wave (PAW) method. Details of similar LDA-based calculations for many different clathrate systems are described in [2-5,27-28,43]. Using the Pulay mixer and an iterative matrix diagonalization scheme, VASP develops a self-consistency cycle to determine the Kohn Sham (KS) ground state, for which the structural, vibrational and thermodynamic properties of a material can be quantitatively computed. It should be noted that VASP can be used to predict many kinds of materials properties at temperature  $T = 0$ .

The application of the computational procedure just described investigates the structural and electronic properties of a material has specified sequence. Normally, all structures are optimized with respect to volume and atomic positions at the very beginning. This geometric optimization is accomplished through initially relaxing the internal coordinates of the atoms confined in a fixed unit cell. Then, the LDA-calculated free energy versus volume ( $E, V$ ) can be determined. It needs to be

mentioned that, the conjugate gradient (CG) method is used to evaluate atomic forces. This process is capable of obtaining the energy versus volume curve and is repeated several times with a number of different unit cell structures. The next step allows several energy-volume ( $E, V$ ) curves to be generated and to be fitted to a 3<sup>rd</sup> order Birch-Murnaghan equation of state (EOS) [105], before achieving the global minimum energy and the optimized lattice parameter. In addition, the bulk modulus and the pressure derivative of the bulk modulus  $K' (\equiv dK/dP)$  can also be determined by this same process. For each case, a 4x4x4 Monkhorst-Pack  $k$ -point grid [106] has been used to carry out the Brillouin zone integration. The free energy convergence criterion was adjusted to be  $10^{-7}$  eV. Electronic properties, including the Fermi energy level ( $E_F$ ), the electronic band structure (BS) and the electronic density of states (EDOS) are calculated after the geometric optimization is completed.

Similarly, vibrational properties, including the vibrational normal modes, the vibrational density of states, and the material elastic constants are also calculated after this optimization process is finished. To gain insight into the vibrational and thermal properties of these Si-based clathrate compounds, a 2x2x2 Monkhorst-Pack  $k$ -point grid combined with a 150 eV cutoff energy were applied to obtain  $\Gamma$  point normal mode vibrational frequencies. Using 245.7 eV (default value for clathrate compounds in this work) cutoff energy does not yield appreciable difference in the acoustic phonon branch of framework, in the presence of any guest impurity arising from Group I. For the similar reason, flat and low-lying rattling mode of guest is still not highly sensitive to choice of the increased cutoff energy.

These modes are obtained by first moving each atom in the face centered cubic (FCC) unit cell by a small finite displacement ( $U_0 = 0.02 \text{ \AA}$ ). This makes it convenient to calculate the vibrational dynamical matrix  $D(\mathbf{q})$ . Some work on the dynamical matrix is evaluated at the gamma ( $\Gamma$ ) point [ $\mathbf{q} = (0,0,0)$ ]. The dynamical matrix  $D(\mathbf{q})$  for non-zero  $\mathbf{q}$  is obtained assuming that the coordinate space matrix elements of  $D(\mathbf{q})$  vanish for atoms that are separated by a distance greater than the third nearest neighbor distance [107]. Eventually, the diagonalization process  $D(\mathbf{q})$  results in finding the vibrational eigenvalues (squared frequencies) and eigenvectors.

## CHAPTER IV

### **STRUCTURAL, ELECTRONIC AND VIBRATIONAL PROPERTIES OF THE BINARY TYPE-II CLATHRATE MATERIALS $A_xM_{136}$**

As discussed above, inorganic compounds which have the Type-II, Group 14, clathrate lattice structure have generated considerable research interest over the past couple of decades and several experimental and theoretical studies of this family of materials have been carried out. A primary reason that such materials are interesting is that they have very good electrical transport properties while simultaneously having glass-like thermal transport properties. As discussed above, materials with both good electrical transport properties and poor thermal transport properties are not very common. However, it is well-known that materials which simultaneously satisfy both criteria have potential applications in thermoelectrics. There have been several experimental and theoretical investigations of both “guest-free” clathrates, formed by face-shared polyhedron cages of Group 14 atoms [3,36,43,96] and of the compounds formed when alkali metal impurities (guests) are put inside the lattice cages. It has been shown that the presence of these guest atoms can improve the material thermoelectric (TE) performance. This better TE performance is qualitatively attributable to an increase in the thermoelectric figure-of-merit ( $ZT$ ) [109,110] of the guest-containing clathrates in comparison with the guest-free counterparts. From a theoretical viewpoint, achieving a large  $ZT$  requires that the total thermal conductivity (including the lattice and electronic contributions) to be minimized. Previous studies

of the guest-containing Type-II clathrate compounds [36,43] have shown that their low lattice thermal conductivity is due to the presence of low-lying guest atom-induced vibrational (“rattling”) modes, which can scatter from the heat carrying acoustic phonon modes of the host lattice, thus suppressing the phonon contribution to the material heat conduction.

#### 4.1 Structural Properties

Since the discovery of the crystalline form of the Type-I clathrate compound  $\text{Na}_x\text{Si}_{136}$  ( $3 < x < 11$ ) in 1965 [16], a variety of theoretical and experimental studies of Na-containing Type-I and Type-II clathrates have been carried out. For instance, Nolas and co-workers used a two-step process to synthesize the Type-II clathrate compound  $\text{Na}_x\text{Si}_{136}$  ( $x = 2.9, 5.1, 8.2, 14.7$ ). These researchers also performed low-temperature transport measurements on polycrystalline specimens [22]. In this regard, the synthesis of the binary clathrate  $\text{Na}_x\text{Si}_{136}$  with controlled Na content ( $x$ ) was accomplished by using a thermal decomposition method, in which the  $\text{Na}_{24}\text{Si}_{136}$  single crystals can lose a desired number of Na atoms. For the single crystal growth of  $\text{Na}_{24}\text{Si}_{136}$ , the Zintl-type compound  $\text{Na}_4\text{Si}_4$  was used and decomposed under argon at high vacuum [29]. Their first step is to allow the vapor phase of  $\text{Na}_4\text{Si}_4$  to react with spatially separated graphite in a closed volume, for the purpose of forming  $\text{Na}_{24}\text{Si}_{136}$ . Then, single crystal  $\text{Na}_{24}\text{Si}_{136}$  was exposed to thermal decomposition in a nitrogen environment with  $P = 10$  torr and  $T = 405$  K for a controlled period of duration, leading

to continuous loss of Na until the desired guest content ( $x$ ) is achieved.

Many reports of the results of XRD measurements on the Type-II clathrate compound  $\text{Na}_x\text{Si}_{136}$  have been presented and discussed in Refs. [22, 26, 29, 30]. In [25], which focuses on the Si framework contraction in  $\text{Na}_x\text{Si}_{136}$  ( $0 < x < 24$ ), as  $x$  increases from 0 to 8, the Na guests have been shown to preferentially fill the 28-atom polyhedron until all such cages are full. Then, as  $x$  continuously increases beyond  $x = 8$ , the 20-atom cages start to be filled by Na guests. Further, in [25], it is shown that as  $x$  increases from 0, the lattice framework contracts for  $0 < x < 8$  and expands for  $8 < x < 24$ . It was found in [25] that the lattice contraction is directly connected to the preferred occupation of Na in the  $\text{Si}_{28}$  cages [61-65]. Choosing the larger  $\text{Si}_{28}$  cage rather than  $\text{Si}_{20}$  in which to place the Na atoms as  $x$  increases led us to wonder if this non-monotonic structural change to guest filling will also happen if the Si host material is replaced by Ge or Sn. As reported in [25], our calculated lattice constant trends with increasing  $x$  for both  $\text{Na}_x\text{Ge}_{136}$  and  $\text{Na}_x\text{Sn}_{136}$  predict no lattice contraction for any  $x$  for either case. However, our calculations also show that replacing the Na guests with the heavier alkali metal atoms K or Rb or Cs in  $\text{Si}_{136}$  results in much weaker lattice contraction as  $x$  changes from 0 to 8 than is found for  $\text{Na}_x\text{Si}_{136}$ .

Our predicted lattice parameters as a function of  $x$  for  $\text{Na}_x\text{Si}_{136}$ ,  $\text{K}_x\text{Si}_{136}$ ,  $\text{Rb}_x\text{Si}_{136}$  and  $\text{Cs}_x\text{Si}_{136}$  ( $0 \leq x \leq 24$ ) are shown in Figure 1. Clearly, for all four materials, the portion of the curves for  $0 \leq x \leq 8$  shows a lattice contraction as  $x$  increases, while the portion of the curves for  $8 < x \leq 24$  shows a lattice expansion with increasing  $x$ . The relationship between this unusual change is interpreted as due to the guest-host

interaction in the  $\text{Si}_{28}$  cage. Also, the predicted minimum lattice constant is 14.558 Å for  $\text{Na}_8\text{Si}_{136}$ , 14.564 Å for  $\text{K}_8\text{Si}_{136}$ , 14.572 Å for  $\text{Rb}_8\text{Si}_{136}$ , and 14.582 Å for  $\text{Cs}_8\text{Si}_{136}$ .

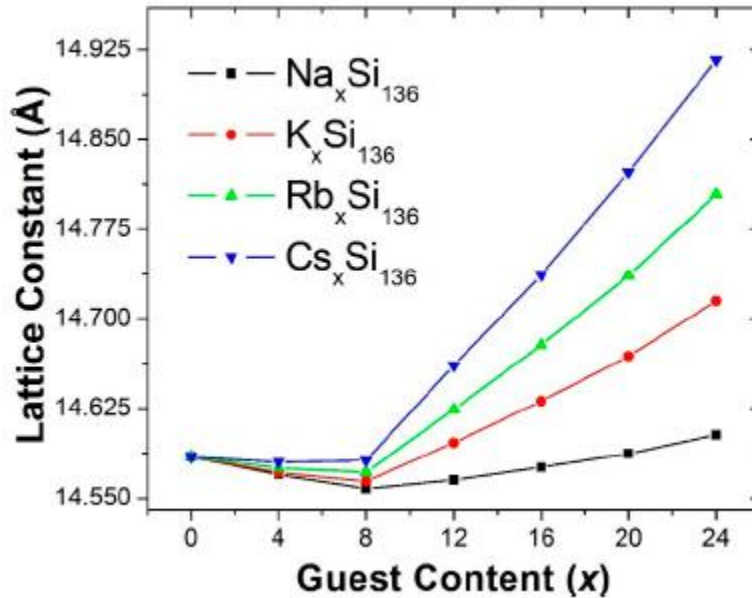


Figure 4.1: Predicted  $x$  dependence of the lattice constants for the Type-II clathrate-based compounds  $\text{A}_x\text{Si}_{136}$  ( $\text{A} = \text{Na}, \text{K}, \text{Rb}, \text{Cs}; 0 \leq x \leq 24$ )

To understand this result, it is helpful to quantitatively consider the relative size difference between the guest atom and the Si cage, which can be correlated with information about how “tightly” or “loosely” the encapsulated guest atom can fit inside the polyhedron. A simple model which explains how “tight” of a Cs rattler in a cage framework was suggested in [5]. Therefore, an “excess” radius  $\Delta r [\equiv r_{\text{cage}}(\text{Cs-X}) - (r_{\text{X}} + r_{\text{Cs}})]$  is defined, where  $r_{\text{X}}$  denotes the covalent radius of a host atom ( $\text{X} = \text{Si}, \text{Ge}, \text{or Sn}$ ),  $r_{\text{Cs}}$  is the ionic radius of Cs and  $r_{\text{cage}}(\text{Cs-X})$  is the LDA-calculated average

radius of the cage. Guided by such model, it was found in [5] that the covalent radius of silicon in the Si<sub>28</sub> cage is  $r_{\text{Si}} \approx 1.17 \text{ \AA}$ , while an estimate of the ionic radius of Cs gives  $r_{\text{Cs}} \approx 1.69 \text{ \AA}$  [66]. Our LDA-determined distance between a Cs atom in a Si<sub>28</sub> cage and its nearest neighboring framework atom Si (3.93 Å) is approximated as the average radius of the hexakeidacahedron cage. In this simple model, the resulting “excess” radius for Cs vibration in Si<sub>28</sub> polyhedron is  $\Delta r = r_{\text{cage}}(\text{Cs-Si}) - (r_{\text{Si}} + r_{\text{Cs}}) = 1.07 \text{ \AA}$ . In comparison with the “over-sized” Si<sub>28</sub> cage, the “excess” radius for Cs in the small cage (20-atom cage) is similarly found to be 0.39 Å. This clearly shows the relatively limited room in the Si<sub>20</sub> cage for the Cs guest to move around. Using this same kind of model, the predicted “excess” radius for the Na guest inside the Si<sub>28</sub> cage gives  $\Delta r = 1.83 \text{ \AA}$ . This leads us to predict that, for  $0 < x < 8$ , the relatively large  $\Delta r$  in Na<sub>x</sub>Si<sub>136</sub> induces a stronger lattice contraction than it does for the similar structural response to Cs filling in Cs<sub>x</sub>Si<sub>136</sub> (see Figure 4.1).

My results for predicted  $x$  dependence of the lattice constant for the Na-containing clathrates Na<sub>x</sub>M<sub>136</sub> (M = Si, Ge or Sn,  $0 \leq x \leq 24$ ) are shown in Figure 4.2. As may be seen in that figure, the lattice constant is predicted to monotonically expand for both filled clathrates Na<sub>x</sub>Ge<sub>136</sub> and Na<sub>x</sub>Sn<sub>136</sub>. However, as  $x$  increases for Na<sub>x</sub>Si<sub>136</sub>, the inset figure shows the predicted lattice contraction for  $0 < x < 8$  and a lattice expansion for  $8 < x < 24$ , in agreement with the results shown in Figure 4.1. In other words, my results predict that replacement of the Si<sub>28</sub> cage by a Ge<sub>28</sub> or Sn<sub>28</sub> cage results in no lattice contraction in Na<sub>x</sub>Ge<sub>136</sub> and Na<sub>x</sub>Sn<sub>136</sub> for any  $x$ .

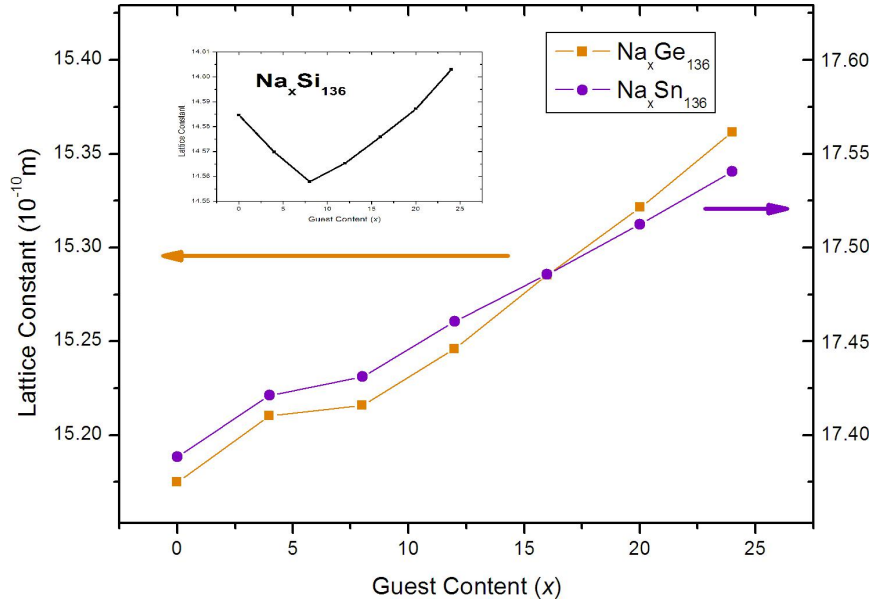


Figure 4.2: Predicted  $x$  dependence of the lattice constant for the Na-containing clathrates  $\text{Na}_x\text{M}_{136}$  ( $\text{M} = \text{Si}, \text{Ge}$  or  $\text{Sn}$ ,  $0 \leq x \leq 24$ ).

## 4.2 Electronic Properties

I have also used the VASP code to investigate the electronic properties of the binary clathrates  $\text{Na}_x\text{Si}_{136}$  ( $x = 8, 12, 16$ ). When discussing my results for electronic properties of the clathrates, it should be noted that it is well known that density functional theory underestimates the bandgap energy of diamond structure Si. The reasons for this involve technical details about the DFT that are beyond the scope of my work [27]. For this reason, my results, especially for properties of the conduction bands, should be viewed as predictions of trends rather than as quantitative results.

My results for  $\text{Na}_x\text{Si}_{136}$  predict that the Fermi energy  $E_F$  is pushed upward into the conduction band as the Na content ( $x$ ) increases from 8 to 12 to 16. Further, I find that the direct “pseudogap” located at the L point increases from 0.45 eV to 0.79 eV

as  $x$  is changed from 8 to 16. These values are smaller than the predicted indirect band gap of about 1.24 eV found for guest-free  $\text{Si}_{136}$ . My first-principles studies of the electronic properties of  $\text{Na}_x\text{Si}_{136}$  ( $8 \leq x \leq 16$ ) have been carried out at the optimized geometries of the relevant materials.

Biswas and Myles [27,67] have previously calculated the electronic structure of  $\text{Na}_{16}\text{Rb}_8\text{Si}_{136}$  and  $\text{K}_{16}\text{Rb}_8\text{Si}_{136}$  and have extensively discussed their results. Specifically, they calculated the electronic density of states (EDOS) for these materials and have found that it contains two neighboring sharp peaks along with a dip near the Fermi level. I note also that their predicted energy separation ( $\Delta E$ ) between these adjacent peaks is about twenty  $k_B T$  at room temperature. As they have discussed, this two-peaked structure and the existence of the “dip” near the Fermi level will lead to  $T$ -dependent Knight shift at higher temperatures. Such predicted EDOS for  $\text{Na}_{16}\text{Rb}_8\text{Si}_{136}$  provides good agreement for the temperature-dependent Knight shift observed in nuclear magnetic resonance (NMR) of the same material [68].

My results for the EDOS in  $\text{Na}_{8(16)}\text{Si}_{136}$  are shown in Figure 4.3. Similar to the Biswas-Myles results for the EDOS in  $\text{Na}_{16}\text{Rb}_8\text{Si}_{136}$  [27,69], my results predict a quasiactivation energy ( $\Delta E$ ), which lies in the range of about 0.4 eV and 0.46 eV. In addition to the EDOS calculated in the lower portion of the conduction band of  $\text{Na}_8\text{Si}_{136}$  and  $\text{Na}_{16}\text{Si}_{136}$ , Figure 4.3 also shows the corresponding Fermi levels, which are denoted by  $E_{F,2}$  and  $E_{F,4}$ .

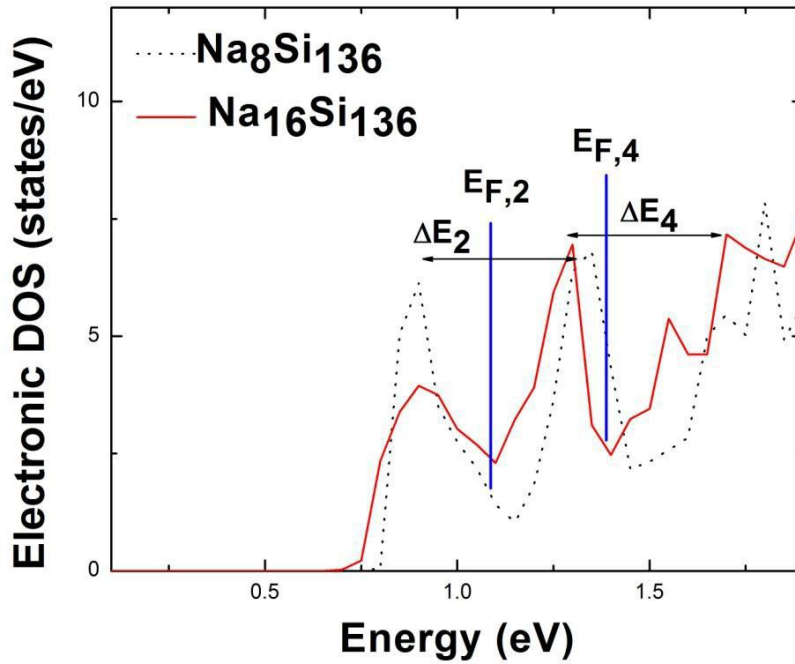


Figure 4.3: Illustration of electronic density of states in the lower portion of conduction band, for the clathrates  $\text{Na}_8\text{Si}_{136}$  and  $\text{Na}_{16}\text{Si}_{136}$ .

My predicted results for the EDOS of  $\text{Na}_x\text{Si}_{136}$  ( $x = 8, 12, 16$ ) in both the valence band and the lower part of conduction band are shown in Figure 4.4. As can be seen in that figure, the Fermi energy is predicted to be shifted slightly upward into the conduction band as  $x$  increases from 8 to 12 and 16. In general, the shapes of the predicted EDOS for the three filled clathrates are almost identical and are also almost independent of guest composition  $x$ . Table 4.1 gives my predicted  $\Delta E$  for  $\text{Na}_x\text{Si}_{136}$  ( $x = 8, 16$ ) as well as that of  $\text{Na}_{16}\text{Rb}_8\text{Si}_{136}$  and  $\text{K}_{16}\text{Rb}_8\text{Si}_{136}$  from the work of Biswas and Myles [27]. The determination of Fermi level of electronic structure is also listed in that table for each filled clathrate.

Table 4.1: LDA-calculated quasiactivation energy and Fermi level of the filled clathrate  $\text{Na}_x\text{Si}_{136}$  ( $x = 8, 16$ ),  $\text{Na}_{16}\text{Rb}_8\text{Si}_{136}$  and  $\text{K}_{16}\text{Rb}_8\text{Si}_{136}$ . The symbol \* denotes the work done in [27].

	$\Delta E$ (eV)	$E_F$ (eV)
$\text{Na}_8\text{Si}_{136}$	0.40	1.10
$\text{Na}_{16}\text{Si}_{136}$	0.45	1.38
$\text{Na}_{16}\text{Rb}_8\text{Si}_{136}$ *	0.25	1.41
$\text{K}_{16}\text{Rb}_8\text{Si}_{136}$ *	0.41	1.61

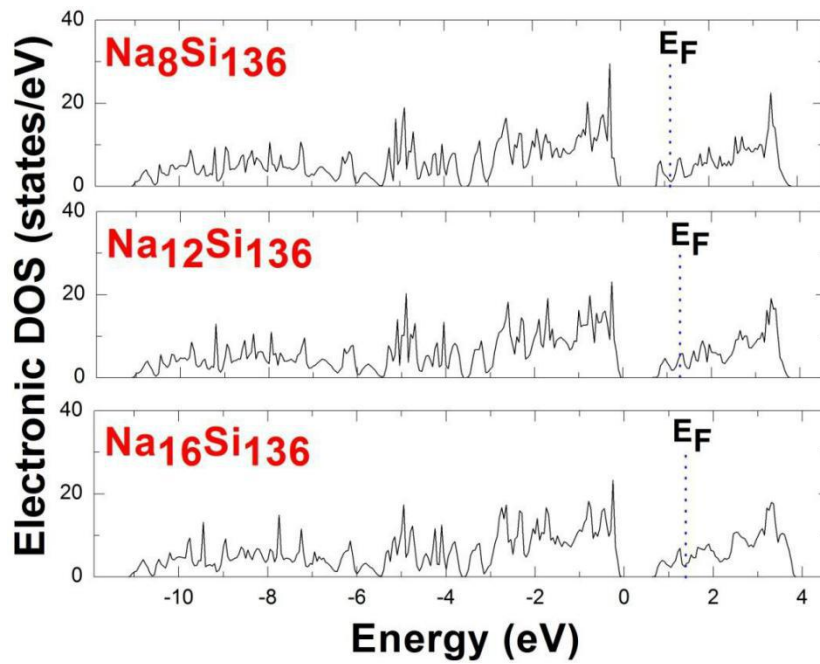


Figure 4.4: Electronic density of states (DOS) of clathrate system  $\text{Na}_x\text{Si}_{136}$ , where  $x = 8, 12, 16$ . The Fermi energy levels ( $E_F$ ) are denoted by dotted lines.

### 4.3 Vibrational Properties and Anharmonic Effects

Calculations of the “rattling” vibrational modes of the alkali metal atom guests in  $A_x\text{Si}_{136}$  ( $A = \text{Na, K, Rb, Cs}$ ;  $0 < x < 24$ ) can reveal very interesting basic physics, such as lattice dynamics and guest-host coupling. The main idea of the “rattler” concept originates from the fact that loosely bound guest atoms encapsulated in the “over-sized” (28 atom) cages in the Type-II clathrates vibrate and produce “localized” modes which are capable of efficiently scattering heat-carrying acoustic phonons [5,70]. Thus, the “rattling” behavior of the alkali metal atom guests can potentially participate in reducing the material thermal conductivity to a glass-like level, as suggested by Slack’s PGEC criteria [31].

My calculations of the vibrational properties of the filled clathrate  $A_x\text{Si}_{136}$  may be divided into two parts, as follows. First, the VASP code was used to calculate the phonon dispersion curves within the harmonic approximation (HA) at zero temperature. Second, the significant anharmonicity of the motion of the Na rattling guests in the  $\text{Si}_{28}$  cages in  $\text{Na}_x\text{Si}_{136}$  has been studied in some detail. The results are the prediction that these anharmonic effects can strongly affect the force constants for the guest vibrational modes.

The LDA-calculated results for the phonon dispersion relations (in the HA) in  $\text{Na}_4\text{Si}_{136}$  are shown in Fig 4.5. The low-lying vibrational (“rattling”) modes of the Na guests occur in a narrow band around  $50 \text{ cm}^{-1}$ . An effective force constant  $K$  for the rattling frequencies in the HA may be obtained by assuming that they can be approximated as  $\omega = (K/M)^{1/2}$ , where  $M$  is atomic mass of the guest. For  $\text{Na}_4\text{Si}_{136}$ ,

doing this for the Na vibrations in the  $\text{Si}_{28}$  cages gives  $K = 0.44 \text{ eV/\AA}^2$  from first-principle viewpoint.

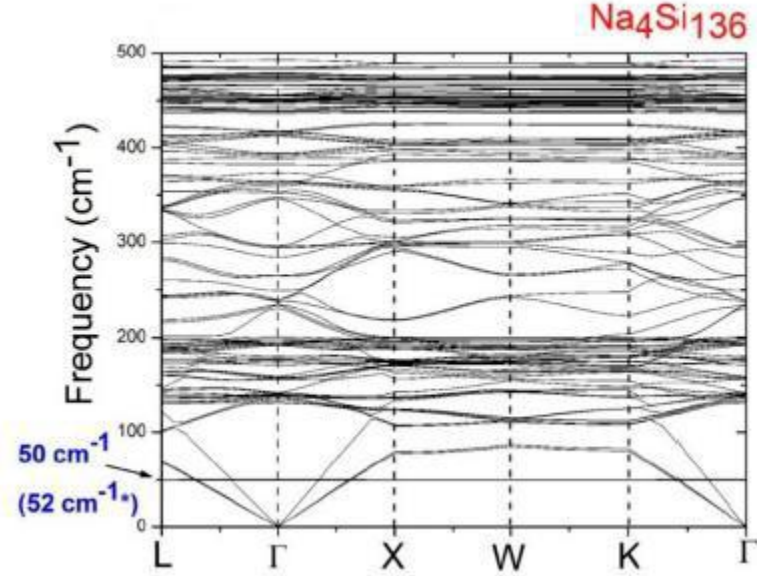


Figure 4.5: The predicted (in the HA) vibrational dispersion relations for  $\text{Na}_4\text{Si}_{136}$ . The number in parentheses is the mode obtained for this material from inelastic neutron scattering (INS) experiments [46].

To study the anharmonic effects associated with the Na guest vibrations in the  $\text{Si}_{28}$  cages, I have used a method which can be summarized as follows. I first used the LDA to calculate the effective guest-host potential energy for a Na guest in a  $\text{Si}_{28}$  cage. Then, in order to approximately treat the lowest order anharmonic effects present in the guest-host interaction, I have expanded this effective potential in a power series in the guest atom displacements, keeping the lowest order (4<sup>th</sup> order) anharmonic terms. That is, I assume that the guest-host potential energy  $V_{\text{eff}}$  can be approximately written as  $V_{\text{eff}} = \frac{1}{2} K_{\text{iso}} r^2 + \frac{1}{4} \epsilon_{\text{iso}} r^4$ , where  $r$  is the displacement from equilibrium and  $K_{\text{iso}}$  and

$\varepsilon_{\text{iso}}$  are empirical constants determined by fitting to the LDA calculated effective potential. Only even order terms are kept in this polynomial expansion because of the symmetry of the effective potential energy curve.

The procedure used to calculate the guest-host framework effective potential energy curves in the LDA was to displace one guest Na atom inside a  $\text{Si}_{28}$  cage, while keeping all remaining atoms in the unit cell fixed. Specifically, each Na was displaced a distance from the center of the  $\text{Si}_{28}$  cage. In all cases, the displacement distance was restricted to the range 0 to  $\Delta r$ , where  $\Delta r$  is the previously discussed “excess” radius of that cage. Our LDA results [5,71] have shown that the “excess” radius of the  $\text{Si}_{28}$  cage is  $\Delta r = 1.83 \text{ \AA}$ , for the case of the Na vibrations. This kind of calculation has been performed in  $\text{Na}_x\text{Si}_{136}$  for Na guests moving in both the X and Z directions (see the discussion of the coordinate system below) and it has also been repeated for guest compositions  $x = 4, 8, \text{ and } 24$ . In the coordinate system considered here, the X and Y axes are chosen to be aligned in a plane that is parallel to the plane of the hexagon, while the Z axis is perpendicular to the hexagon in the 28-atom cage. The resulting effective potential energy curves for the compositions  $x = 4, 8, \text{ and } 12$  are shown in Figure 4.6. Results for motions along the X direction are shown. By symmetry, the effective potential energy for Y-directed and Z-directed motions are identical to that for X-directed motions.

As can be seen in Figure 4.6, for  $\text{Na}_4\text{Si}_{136}$  and  $\text{Na}_8\text{Si}_{136}$ , the results of this procedure predict that the effective potential energy has a “bump” at the cage center. Thus, each of the effective potential energy curves in Figure 4.6 has a “Mexican-hat”

(double valley) shape. This form of the potential energy shows that Na guests in the  $\text{Si}_{28}$  cages are dynamically unstable at the cage center. Thus, these calculations predict that, at elevated temperatures, thermal excitation can induce the Na guests to move off the cage center to a site with a lower potential energy. Specifically, these calculations find that the “localized” off center minimum valley of the effective potential curve is about 0.017 eV and 0.01 eV below zero, for  $\text{Na}_4\text{Si}_{136}$  and  $\text{Na}_8\text{Si}_{136}$ , respectively. That is, the effective potential energy valley depth is predicted to be about  $0.66 k_{\text{B}}T$  and  $0.39 k_{\text{B}}T$  at room temperature for  $\text{Na}_4\text{Si}_{136}$  and  $\text{Na}_8\text{Si}_{136}$ , respectively. This kind of effect might be correlated with the measured strong temperature dependence of isotropic atomic displacement parameter  $U_{\text{iso}}$ , reported in [72,73].

This predicted “off-center” position for Na in the  $\text{Si}_{28}$  cages in  $\text{Na}_x\text{Si}_{136}$  can, in principle, be correlated with the experimentally measured guest equilibrium location at various temperatures. However, the disorder of the guest position makes the understanding of such “off-center” sites complex. Similar effects have been observed in some Type-I clathrates, including  $\text{Sr}_8\text{Ga}_{16}\text{Ge}_{30}$ ,  $\text{Ba}_8\text{Ga}_{16}\text{Ge}_{30}$ ,  $\text{Eu}_8\text{Ga}_{16}\text{Ge}_{30}$  [66-73]. The arrow in the inset figure of Figure 4.6 indicates that, the “localized” off center minimum valley is shifted towards the cage center when the Na content is changed from 4 to 8 to 24.

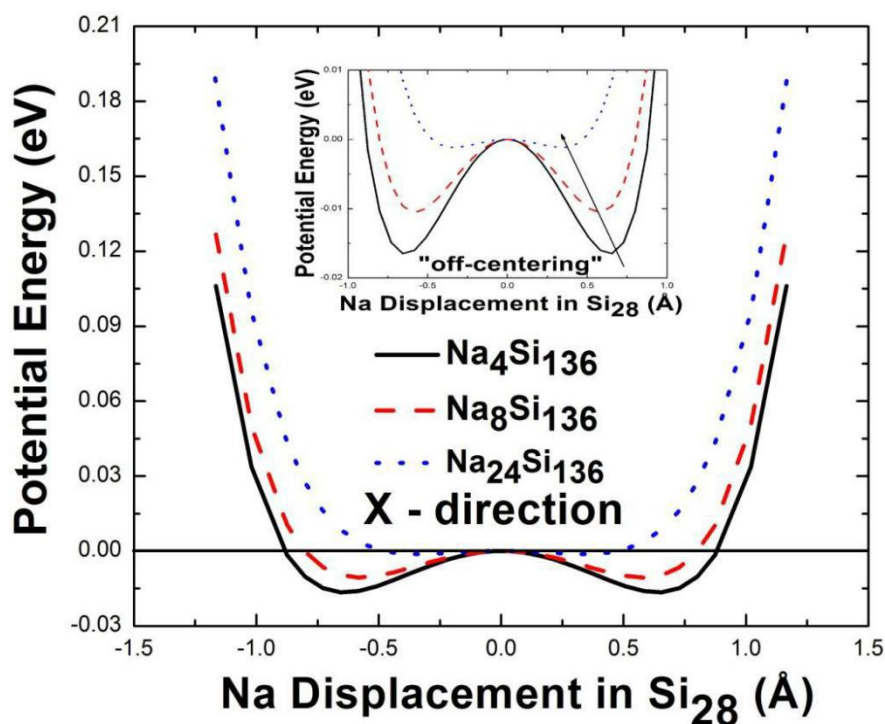


Figure 4.6: The calculated, isotropic, Mexican hat shaped potential-energy curves for Na vibrations in the large 28-atom cages in the clathrate system  $\text{Na}_x\text{Si}_{136}$  ( $x = 4, 8, 24$ ). X represents the motion direction with respect of the Na atom.

Considerable experimental work by Beekman and collaborators for  $\text{Na}_x\text{Si}_{136}$  was focused to detecting the isotropic, “off-center” displacement of Na in  $\text{Si}_{136}$  and studying this system in considerable detail [25,60,74-76]. An early report by Beekman on the Na vibrations in  $\text{Si}_{28}$  shows a nearly  $x$ -independent “off-center” displacement, which is measured to be about 0.4-0.5 Å [60]. My first-principles calculations correlate well with these experimental results. This is shown Figure 4.7, where XRD data on the “off-center” displacement of Na is shown, along with my first-principles predictions of the Na displacements in the  $\text{Si}_{28}$  are given. For  $x = 12$  and  $x = 16$ , my calculations predict an isotropic displacement which ranges from 0.50 Å for  $\text{Na}_{12}\text{Si}_{136}$  to 0.42 Å for  $\text{Na}_{16}\text{Si}_{136}$ . It should be noted that an attractive interaction occurs between

the Na guests in the presence of the above discussed anharmonic guest-host potential energy, which causes the “off-center” displacement of the guests.

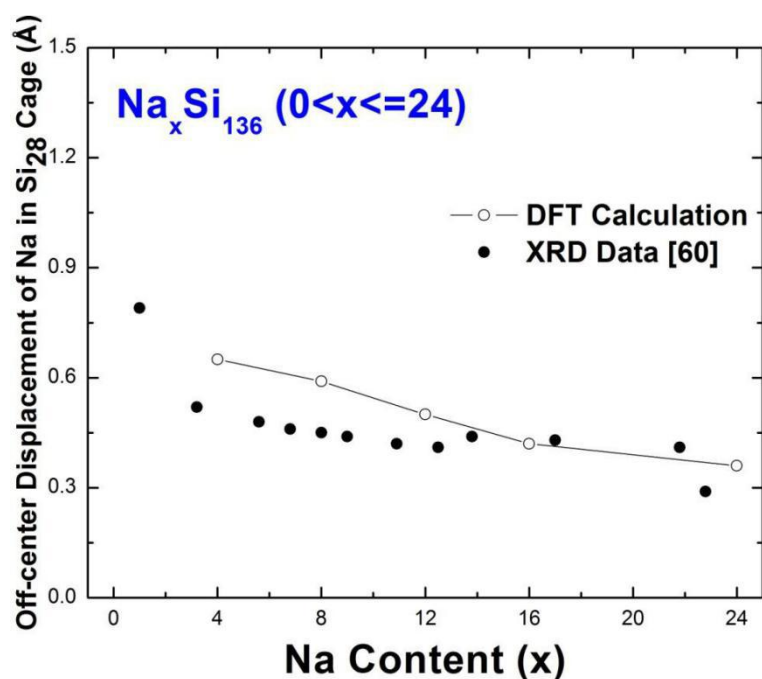


Figure 4.7: DFT-calculated “off-center” displacements of Na in the Si<sub>28</sub> cages in Na<sub>x</sub>Si<sub>136</sub> as a function of Na composition ( $x = 4, 8, 12, 16, 24$ ), along with XRD measured displacements by Beekman et. al. [60].

I have used a similar method to study anharmonic effects associated with the rattling guest atoms K, Rb, and Cs in Si<sub>136</sub>. Figure 4.8 shows the LDA-calculated isotropic guest-framework effective potentials for each of these three guests in Si<sub>28</sub> cages. The effective potential energy is again symmetric, so that only the spring harmonic constant  $K_{iso}$  and the quartic anharmonic coefficient  $\epsilon_{iso}$  need to be considered. That is, the LDA-calculated effective potential energy has been fit to the equation for  $V_{eff}$ , discussed above. I have found that increasing the atomic mass of

the rattling guest results in a higher potential energy at a given displacement. After fitting the LDA effective potential to  $V_{\text{eff}}$  the resulting second order and 4-th order coefficient for the guest-framework interaction potential (Figure 4.6) are summarized in Table 4.2.

Table 4.2: Fitting parameters of guest-host interaction energy potentials for  $\text{Na}_x\text{Si}_{136}$  ( $x = 4, 8, 24$ ),  $\text{K}_x\text{Si}_{136}$ ,  $\text{Rb}_x\text{Si}_{136}$  ( $0 < x \leq 24$ ). The isotropic harmonic spring constant  $K_{\text{iso}}$  and the lowest order anharmonic interaction constant  $\epsilon_{\text{iso}}$  are listed here. The estimated low-lying anharmonic vibrational frequency  $\Omega(T = 300\text{K})$  is compared to the phonon frequency  $\omega_{\text{ph}}$  calculated by VASP in the harmonic approximation and  $(K_{\text{iso}}/M)^{1/2}$

Materials	$K_{\text{iso}}$ (eV/Å <sup>2</sup> )	$\epsilon_{\text{iso}}$ (eV/Å <sup>4</sup> )	$\omega_{\text{ph}}$ (cm <sup>-1</sup> )	$\Omega(T=300\text{K})$ (cm <sup>-1</sup> )	$(K_{\text{iso}}/M)^{1/2}$ (cm <sup>-1</sup> )
$\text{K}_4\text{Si}_{136}$	0.209	1.106	38.05	45.79	38.03
$\text{K}_8\text{Si}_{136}$	0.292	1.095	47.12	50.54	44.95
$\text{K}_{12}\text{Si}_{136}$	0.359	1.063	51.85	52.55	49.84
$\text{K}_{16}\text{Si}_{136}$	0.415	1.029	56.94	57.13	53.58
$\text{K}_{20}\text{Si}_{136}$	0.446	0.998	59.40	58.70	55.55
$\text{K}_{24}\text{Si}_{136}$	0.484	0.956	59.41	60.60	57.87
$\text{Rb}_4\text{Si}_{136}$	0.482	1.399	33.03	41.67	39.06
$\text{Rb}_8\text{Si}_{136}$	0.565	1.389	37.59	44.41	42.29
$\text{Rb}_{12}\text{Si}_{136}$	0.596	1.353	39.81	45.37	43.43
$\text{Rb}_{16}\text{Si}_{136}$	0.645	1.281	40.68	46.85	45.18
$\text{Rb}_{20}\text{Si}_{136}$	0.676	1.211	41.21	47.74	46.26
$\text{Rb}_{24}\text{Si}_{136}$	0.699	1.162	41.71	48.40	47.04
$\text{Cs}_4\text{Si}_{136}$	0.977	1.861	40.31	45.68	44.60
$\text{Cs}_8\text{Si}_{136}$	1.035	1.857	43.61	46.90	45.90
$\text{Cs}_{12}\text{Si}_{136}$	0.999	1.776	43.53	46.10	45.09
$\text{Cs}_{16}\text{Si}_{136}$	0.966	1.691	44.76	45.35	44.34
$\text{Cs}_{20}\text{Si}_{136}$	0.925	1.568	45.17	44.38	43.39
$\text{Cs}_{24}\text{Si}_{136}$	0.909	1.427	43.98	43.95	43.01
$\text{Na}_4\text{Si}_{136}$	-0.176	0.458	50.00	24.79	----
$\text{Na}_8\text{Si}_{136}$	-0.143	0.456	33.59	26.31	----
$\text{Na}_{24}\text{Si}_{136}$	-0.061	0.467	36.27	31.43	----

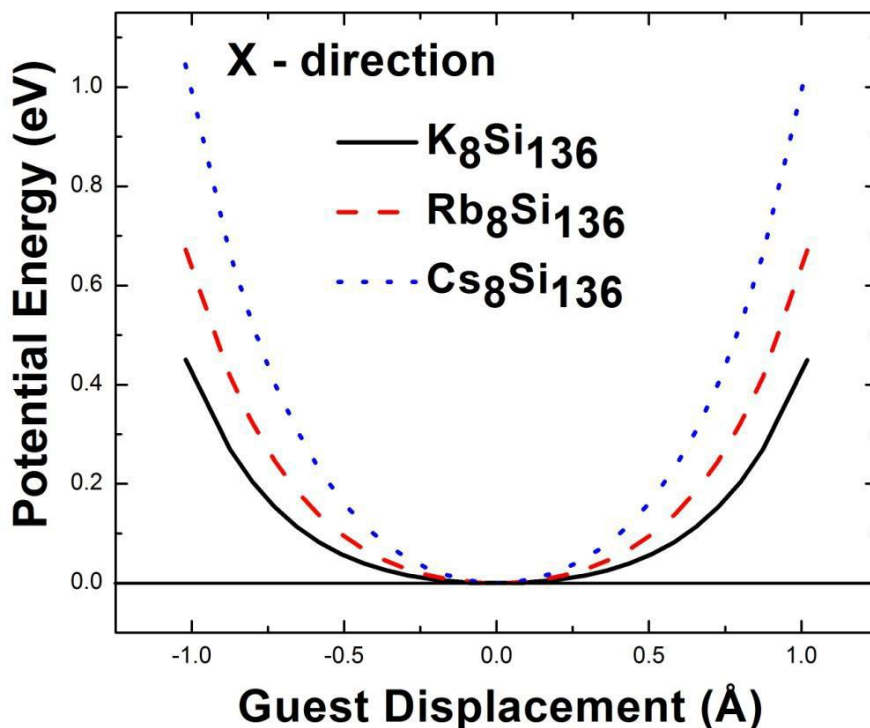


Figure 4.8: The potential energy curves for alkali atoms K,Rb,Cs inside Si framework. X and Z represents the motion direction with respect to alkali atom.

#### 4.4 Vibrational Anharmonic Effects in the Self-consistent Phonon Model

A second method I have used to examine anharmonic effects in the guest-host interaction is to use the self-consistent phonon (SCP) model [111]. That approach is different from conventional lattice dynamics tools which analyze the lattice vibrations in the harmonic approximation at  $T = 0$ . This method includes anharmonic effects in a general, systematic way. In what follows, I give an overview of this method.

The anharmonic nature of the phonon rattling modes at nonzero temperature can be quantitatively understood by introducing the displacement  $U$ . Considering the periodic boundary conditions, it has the form

$$U = \frac{\sqrt{\langle u^2(\vec{k}, j) \rangle}}{\sqrt{M}} \exp[2\pi i(\vec{k} \cdot \vec{R} - \phi(\vec{k}, j))] \quad (4.1)$$

Here, the mean square amplitude of the phonon atomic displacement is defined by using the Debye model [67]:

$$U_{iso} = \langle u^2(\vec{k}, j) \rangle = \frac{\hbar}{2M\omega(\vec{k}, j)} \coth\left(\frac{\hbar\omega(\vec{k}, j)}{2k_B T}\right) \quad (4.2)$$

where the vibrational frequency  $\omega(\vec{k}, j)$  is denoted SCP-based frequency

$\Omega_k^{QHA}(T) (= \Omega^{QHA}(T))$ , remaining independent of volume, wavevector ( $\vec{k}$ ) and phonon branch ( $j$ ). Making use of diagonalization process applied to dynamic matrix  $D_{\mu\nu}$ ,

one relates spring constant and quartic anharmonic coefficient to  $\Omega^{QHA}(T)$  and

thermal displacement :

$$M\Omega^{QHA}(T) = K_{iso} + \varepsilon_{iso} \langle u^2(\vec{k}, j) \rangle \quad (4.3)$$

$K_{iso}$  along with  $\varepsilon_{iso}$  can be obtained by fitting LDA energy to polynomial function

$V_{eff} = \frac{1}{2}K_{iso}x^2 + \frac{1}{4}\varepsilon_{iso}x^4$ . Following lists our DFT calculation on predicting lowest-

lying, anharmonic phonon mode for two various rattlers (Na,Rb) in 28-atom cage of silicon.

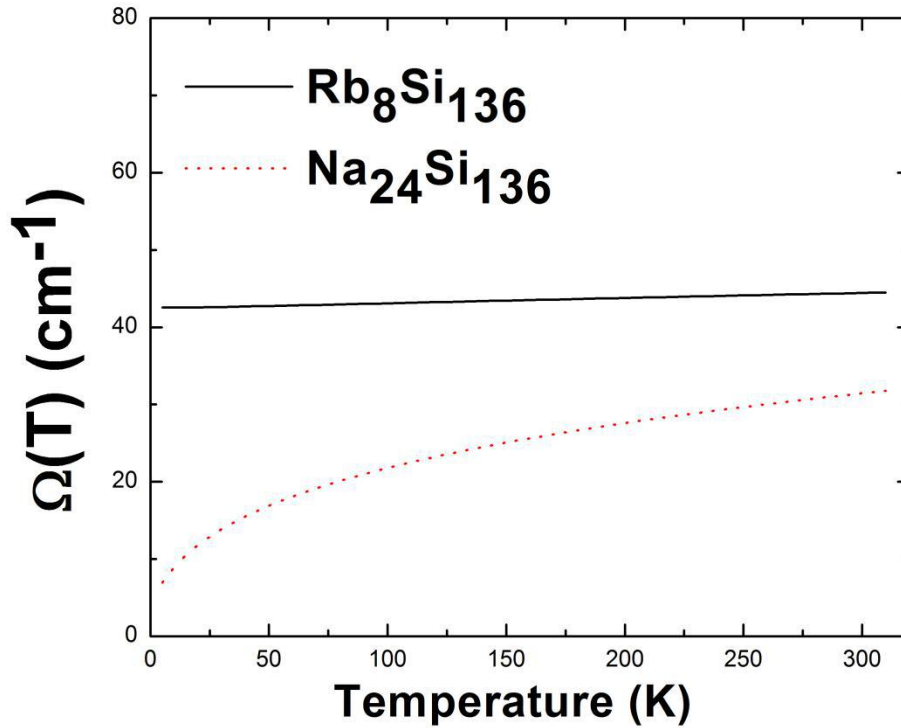


Figure 4.9: Anharmonic rattling frequency of guest vibrations in a Si<sub>28</sub> cage as a function of temperature for the filled binary clathrates Rb<sub>8</sub>Si<sub>136</sub> and Na<sub>24</sub>Si<sub>136</sub>.

In contrast to vibration of Na rattling mode in the Si<sub>28</sub> polyhedron cage, very slight discrepancy on temperature-dependent  $\Omega^{OHA}(T)$  has been captured for localized Cs impurity. It is noted that the guest “off-center” displacement has larger impact on its anharmonic rattling frequency and correlating thermal average of  $u^2$ . Our results in Figure 4.9 give about 42.55 cm<sup>-1</sup> ( $\approx$  5.27 meV) for Rb vibration frequency at  $T=0$ , leading to roughly 4.2% smaller than that obtained at  $T=300$  K. However, the predicted  $\Omega^{OHA}(T)$  at 300 K are significantly higher than that at absolute zero for sodium filled clathrate. Such strong temperature dependence of the result indicates static disorder effects do influence the isotropic displacement parameters (ADPs). In

other words, mean square isotropic atomic displacement for Na which resides in “off-centered” system is boosted, compared to  $\langle u^2 \rangle$  for “on-center” vibration at the same temperature. Our calculation points out that, this difference on thermal average  $\langle u^2 \rangle$  is nearly close to the square of “off-centering” displacement discussed above (see Figure 3.7).

Previous XRD report proposed by M. Beekman *et. al.* [73] also stated that, the strong  $T$ -dependence of  $\langle u^2 \rangle$  for Na@Si<sub>28</sub> in Na<sub>x</sub>Si<sub>136</sub> might be attributable to thermal excitation, which causes the guest to explore minimum of the “Mexican-hat” shape potential (see Figure 3.6). That is to say, the quite anharmonic and dynamically unstable guest-host interaction facilitates the rattler to seek larger volume to vibrate at elevated temperatures. For the case of Na<sub>24</sub>Si<sub>136</sub>, our DFT-determined result predicts the harmonic rattling frequency  $\omega_{ph}$ , resulting in approximately 15% larger than the anharmonic counterpart  $\Omega^{QHA}(T)$  at 300 K. This differed frequency can be interpreted in the picture of thermal displacement parameter, while taking “off-centered” displacement due to static disorder into account. Mathematically, the

relation  $U_{iso}(\Omega_{T=300K}^{QHA}) \approx U_{iso}(\omega_{ph}) + d^2$  is used to account for the existence of extremely strong ADPs observed by means of XRD, INS and temperature-dependent heat capacity ( $C_p$ ) measurement [72,73,112]. Numerical values of  $\Omega_{T=300K}^{QHA}$  and  $\omega_{ph}$

computed by SCP model and VASP code can be plugged into classical equation

$$U_{iso}(\omega) = \frac{k_B T}{M \omega^2}$$

within high temperature approximation [113], leading to the

corresponding ADPs which display about 0.497 Å<sup>2</sup> and 0.122 Å<sup>2</sup> for Na<sub>4</sub>Si<sub>136</sub>.

Therefore, the calculated off-centered displacement  $d$  is approximately equal to about

0.61 Å, which is reasonably comparable to the data ( $\sim 0.52$  Å) in Figure 3.7. Similarly, our performed calculation on  $d$  value for  $\text{Na}_{24}\text{Si}_{136}$  shows 0.28 Å, which makes good agreement with the result estimated by Rietveld analysis [114]. The DFT-calculated “off-centering” displacement of Na vibration shows about 0.36 Å, which is higher than SCF-determined  $d$ .

Now, considering the rattler’s concentration impact on room temperature quartic anharmonicity, we found that  $\Omega_{T=300K}^{OHA}$  basically get close to their LDA-determined  $(K_{iso} / M)^{1/2}$ , as atomic content of tuned guest element is raised. Comparably small ratio of forth-order coefficient  $\epsilon_{iso}$  to  $K_{iso}$  with increased  $x$  of  $\text{A}_x\text{Si}_{136}$  correlates to slight quartic anharmonicity. Following table lists our systematic comparison among harmonic spring constant, quartic anharmonic coefficient, anharmonic rattling frequency, LDA-calculated phonon frequency and  $(K_{iso} / M)^{1/2}$ , with respect to  $\text{A}_x\text{Si}_{136}$  clathrate ( $A = \text{K}, \text{Rb}, \text{Cs}; 0 < x \leq 24$ ) and x-axis directed motion. Discussion on how temperature-dependent rattling frequency effects mean atomic displacement parameters as well as the attractive coupling for guest-host pair will be given in Chapter VII.

## CHAPTER V

### ELECTRONIC PROPERTY AND PHONON ANHARMONICITY OF $\text{Si}_{136-x}\text{Ge}_x$ ALLOYS

In the presence of suggested Si/Ge arrangements among framework Wyckoff sites for  $\text{Si}_{136-x}\text{Ge}_x$  ( $0 < x \leq 128$ ) system [77], our theoretical work accounts for physical origin of low-temperature negative thermal expansion (NTE), which is intrinsically affected by phonon anharmonicity arising mostly from transverse acoustic (TA) branch. One primitive model to survey anharmonic thermodynamics exploits the volume-dependent mode Grüneisen parameter, which quantifies how collective vibration of lattice structure deviates from simple harmonic oscillations. Measured shift of Raman lines under varied pressure also provides an approach to examine Grüneisen parameters, pertinent to low-lying optical and acoustic modes of  $\text{Na}_1\text{Si}_{136}$  [80].

#### 5.1 Structural Properties

Empty alloy clathrate are a class of materials possessing crystalline or amorphous framework made of more than one Group IV element (*e.g.* Si, Ge or Sn). These “guest-free” alloy clathrates are formulated by covalently bonding configuration exhibiting  $sp^3$  hybridized geometry, in viewpoint of structural characteristics. At present, limited number of reports have existed to reveal electronic, vibrational and transport properties of Type-II SiGe alloy clathrate. Among them,

synthesis work of  $\text{Si}_{136-x}\text{Ge}_x$  done by L. L. Baranowski et. al. classifies their phase structures into two categories depending on guest composition  $x$  [115]. Their study pointed out the stoichiometric amount ( $x$ ) of Si for amorphous formation ranges approximately from 17 to 28.9 . And the likely cause of amorphous region is due to a miscibility gap. Following figures list our first-principles work on composition-dependence of lattice parameter and optical bandgap for semiconducting  $[\text{Si}_{1-x}\text{Ge}_x]_{136}$ .

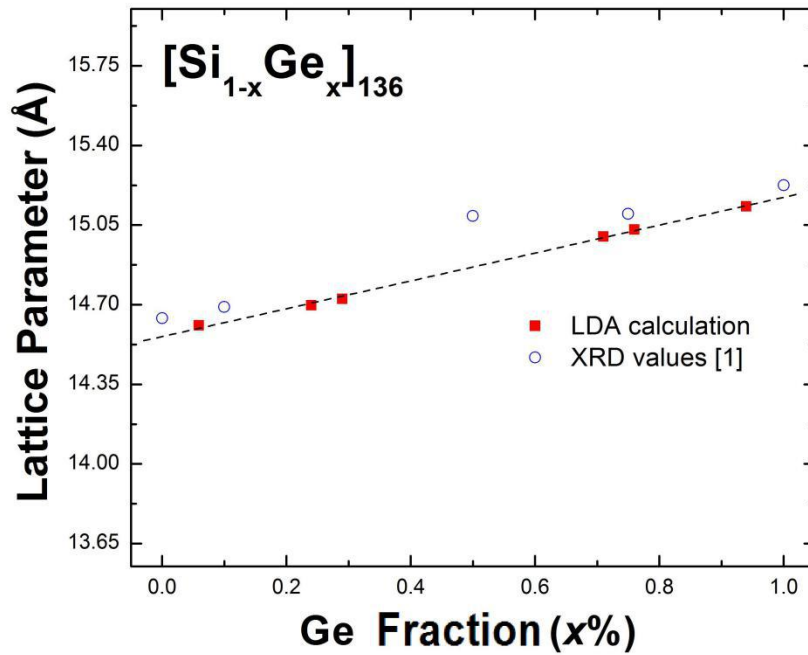


Figure 5.1: LDA-determined lattice parameter trends (red squares) as a function of Ge mole fraction for  $[\text{Si}_{1-x}\text{Ge}_x]_{136}$ , in comparison with XRD data (open circles). The dashed line drawn for LDA data is from linear fit procedure and acts as a guide for the eye.

## 5.2 Electronic Properties

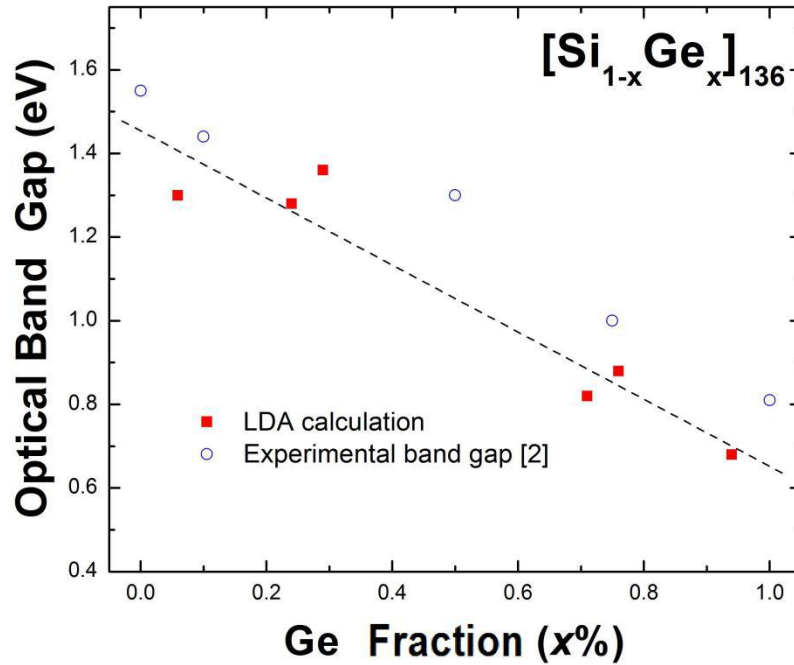


Figure 5.2: Comparison of predicted band gap (red squares) and experimentally obtained results (open circles) for  $[\text{Si}_{1-x}\text{Ge}_x]_{136}$  ( $0 < x < 136$ ) [115]. The dashed line drawn acts as a guide for the eye.

As can be shown in Figure 5.1, an increase of lattice parameter is found with increasing Ge content, on the basis of first-principles calculation. Similar agreement is observed between XRD data and our LDA work in the absence of amorphous region ( $0.15 \leq x \leq 0.5$ ). At certain composition of added Ge atoms (*e.g.*  $x = 0.15$  and  $x = 0.5$ ), the formation of SiGe clathrate alloy exhibits mostly crystalline phase but a slightly small amount of amorphous background [115]. A lower calculated optical bandgap in

Figure 5.2 is expected for  $x \sim 0.77$ . It seems not surprised, because LDA method always underestimates the fundamental bandgap energy [27,28].

Following results are our calculated electronic band structures of SiGe clathrate possessing structural symmetries ( $Fd-3m$ ). All energies are measured from the top of valence band located at L, zero of which remains stably fixed and independent of Ge concentration. Calculations are performed at optimized geometry for each SiGe alloy material. Our determined bandgap energy for  $x = 8$  case of  $\text{Si}_{136-x}\text{Ge}_x$  is about 1.27 eV, agreeing quantitatively well with previous DFT result ( $\sim 1.23$  eV) obtained by CASTEP code [77]. In addition, the top of the valence band and the bottom of the conduction band occurs at L and  $\Gamma$  high symmetry point, enabling bandgap of  $\text{Si}_{128}\text{Ge}_8$  to be in between “nearly-direct” and indirect manner. The valence maximum at L is 100 meV higher than that at  $\Gamma$  point, resembling the experimental work in a excellent manner.

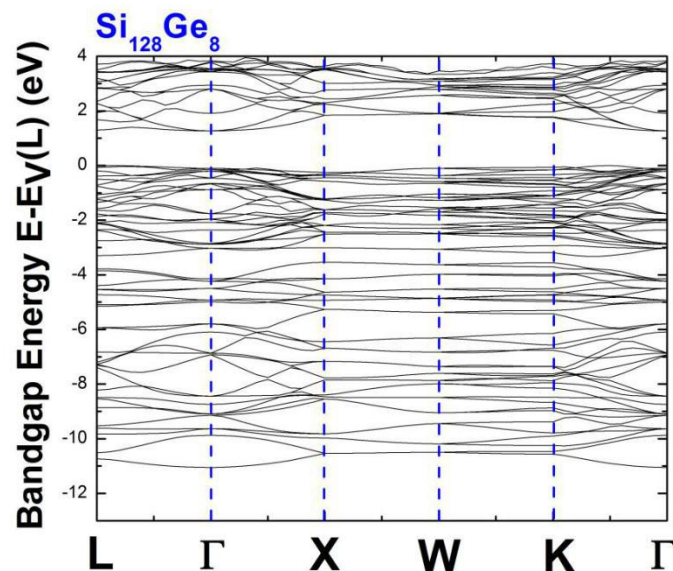


Figure 5.3: Electronic band structures of  $\text{Si}_{128}\text{Ge}_8$ , where the zero of energy is set to be the valence band maximum at L point.

Figure 5.3 thus provides feasible theoretical approach to turn indirect band gap to direct after tuning Ge doping concentration, as detailed discussion is found elsewhere [115]. Ground state computation can facilitate informative study on such materials electronic properties. For Ge-containing Si clathrate of Type-II, several compounds  $\text{Si}_{136-x}\text{Ge}_x$  ( $x = 8, 40, 104$ ) are investigated through their LDA-calculated electronic density of states (EDOS). With no guest insertion, “empty” cage framework of  $\text{Si}_{136-x}\text{Ge}_x$  behaves as four-fold-coordinated  $sp^3$  structure, while all valence electrons are fulfilling the Zintl-Klemm concept to form covalent bonds [116]. For the same reason, no charge transfer occurs because all valence electrons are used to build charge-balanced composition, making the material to be semiconductor which plays potential role in thermoelectric application. We found that, electronic properties of SiGe alloys are sensitive to composition  $x$ , especially existence of the fully occupied 96g Wyckoff sites by Ge. Our DFT calculation in Figure 5.4 examines the electronic density of states as a function of Ge composition., considering unit cell symmetry which allows any number of the three inequivalent sites ( $8a$ ,  $32e$ ,  $96g$ ) are completely filled by the same Group IV atom. Here, no big difference has been found between EDOS of  $\text{Si}_{128}\text{Ge}_8$  and that of  $\text{Si}_{96}\text{Ge}_{40}$ , when null and quite small number of Ge-Ge bond exists in both materials. But for Ge-dominant alloy  $\text{Si}_{32}\text{Ge}_{104}$ , it is noticed that lower portion of conduction band in EDOS curve experiences “downshift”, leading to reduced optical band gap. Additionally, tail part of EDOS for conduction

band indicates those energy states surrounding minimum at about 1.15 eV are becoming sparsely populated.

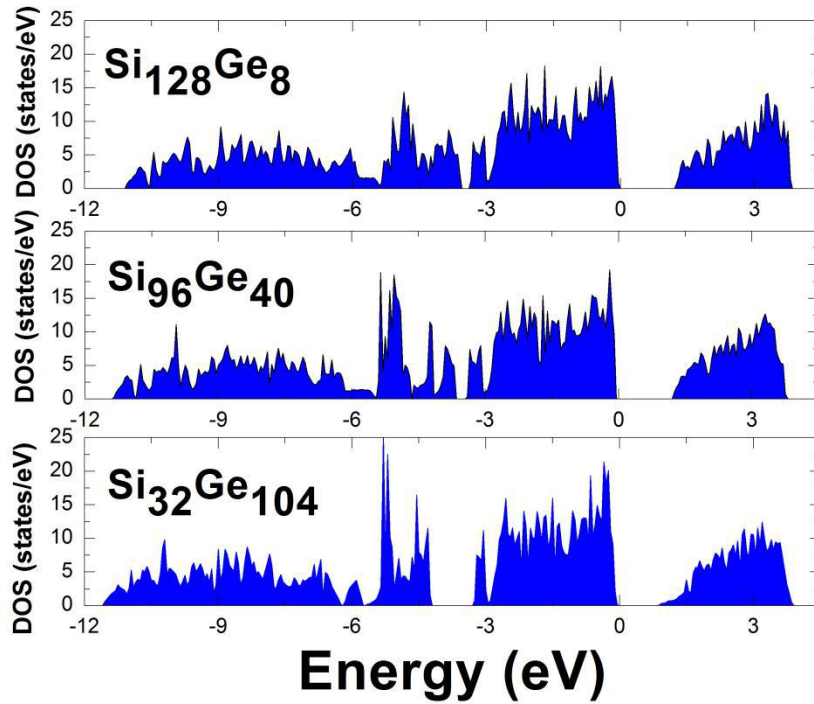


Figure 5.4: Calculation of electronic density of states for  $\text{Si}_{136-x}\text{Ge}_x$  ( $x = 8, 40, 104$ ), zero energy is set to be at the maximum of valence band.

### 5.3 Vibrational Properties and Anharmonic Effects

Before talking about the features of lattice phonon spectra in the high-symmetry directions, we emphasized that the low-lying acoustic and optic mode regions are of greater importance than others. In other words, six phonon branches are mainly discussed for each  $\text{Si}_{136-x}\text{Ge}_x$  material: longitudinal acoustic (LA), transverse acoustic (TA(1) & TA(2)) with double degeneracy along specific direction,

longitudinal optical and transverse optical TO(1) & TO(2)) branches which might be coinciding at certain  $\vec{q}$ -points.

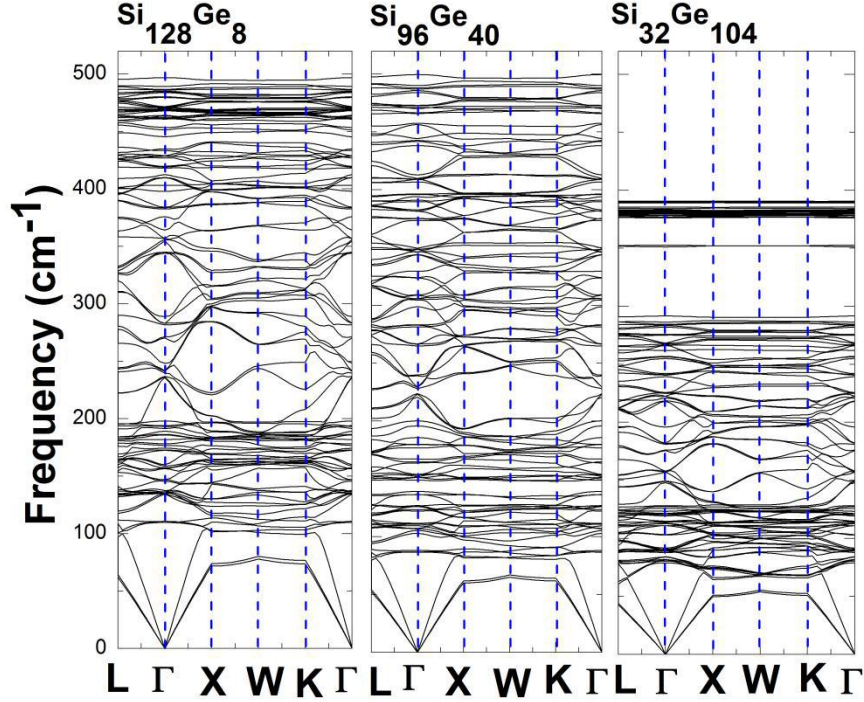


Figure 5.5: Dispersion relations of  $\text{Si}_{136-x}\text{Ge}_x$  ( $x = 8, 40, 104$ ) obtained from VASP.

It is worthwhile to postulate that collective motion of framework atoms at optimized geometry are effected by the numbers of Ge-Ge bonds, from both vibrational and transport point of view. Our adopted models considered here for  $\text{Si}_{136-x}\text{Ge}_x$  system have been suggested by K. Moriguchi et. Al., stating how host atoms reside at three inequivalent sites ( $8a$ ,  $32e$ ,  $96g$ ) [77]. Besides, it is noted that the number of Ge-Ge bonds in 34-atom unit cell ranges from 0 in  $\text{Si}_{128}\text{Ge}_8$  to 8 in  $\text{Si}_{96}\text{Ge}_{40}$  and 36 in  $\text{Si}_{32}\text{Ge}_{104}$ , in an ascending order. Displayed dispersion spectrum for

$\text{Si}_{32}\text{Ge}_{104}$  in Figure 5.5 demonstrates its compressed optic band region ( $71 \text{ cm}^{-1} \sim 390 \text{ cm}^{-1}$ ), which maximum is reduced by 21% approximately in contrast to that of  $\text{Si}_{128-x}\text{Ge}_x$  ( $x = 8, 40$ ). Near the top of optic bands exists extremely flat and dense phonon mode region in Ge-dominant alloy  $\text{Si}_{32}\text{Ge}_{104}$ . Such apparent reduction of the highest optic band in  $\text{Si}_{32}\text{Ge}_{104}$  might be attributable to somewhat loosely bonding behavior of Ge-Ge bond, when compared to “rigid” Si-Si bond which effective force constant is about  $24 \text{ eV/\AA}^2$  in  $\text{Si}_{136}$  [78]. Further, comparably weak coupling inside Ge-Ge bond might help suppress the localized, quantized collection motion of lattice framework atoms in  $\text{Si}_{32}\text{Ge}_{104}$  upon structural expansion. Clearly saying, fractional change in mode frequency of TA(1) phonons is more slowly increasing in the view of ascending  $\frac{\Delta V}{V_0}$ . Below diagram (Figure 5.6) shows Ge-Ge bond effect on mode Grüneisen parameter of the TA (1) phonon at L-point in  $\text{Si}_{136-x}\text{Ge}_x$  ( $x=32, 104$ ). The determined ratio of  $\gamma_{TA(1)}(L)$  for  $\text{Si}_{32}\text{Ge}_{104}$  to  $\gamma_{TA(1)}(L)$  for  $\text{Si}_{104}\text{Ge}_{32}$  is about equal to 0.72, indicating that lattice framework is accompanied by weak vibrational response upon geometry dilation when Ge content dominates.

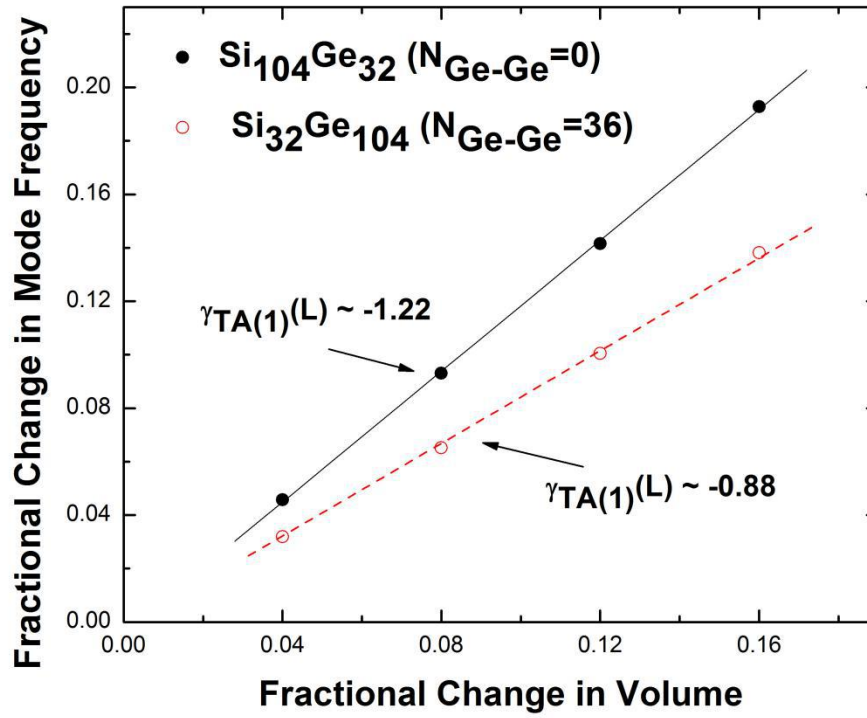


Figure 5.6: Variation of fractional change in mode frequency with respect to TA(1) phonon branch along  $\Gamma$ -L direction, as a function of fractional change in volume.

Furthermore, the vanishingly small NTE effect is also expected to be due to increased number of Ge-Ge bond in  $\text{Si}_{136-x}\text{Ge}_x$ . We will be presenting the detailed  $x$ -dependence impact on low-temperature NTE for silicon germanium alloys in the flowing chapter.

In the picture of quasi-harmonic approximation (QHA), anharmonicity of the vibrations in the crystalline solid is inspected by considering mode-specific Grüneisen parameters  $\gamma_i(\vec{q})$ , corresponding to the wave vector  $\vec{q}$  and phonon branch  $i$ . Therefore, irrespective of the temperature dependence of phonon vibration frequency at state  $(i, \vec{q})$ , the fractional change in material geometry leads to the mode Grüneisen

parameter when taking finite difference method (FDM) into account:

$$\omega_i(\vec{q}) = \omega_i^0(\vec{q}) \left( 1 - \gamma_i(\vec{q}) \frac{\Delta V}{V} \right) \quad (5.1)$$

Here, primitive definition of mode Grüneisen parameter is introduced within the QHA formalism:  $\gamma_i(\vec{q}) \equiv -\frac{d \ln \omega_i(\vec{q})}{d \ln V}$ .  $\omega_i^0(\vec{q})$  and  $\omega_i(\vec{q})$  are wave-vector dependent phonon vibration mode for equilibrium geometry ( $V_0$ ) and strained configuration  $V$  ( $\Delta V = V - V_0 \neq 0$ ) respectively. Figure 5.7 shows the estimated  $\gamma_{TA(1)}(\Gamma)$  and  $\gamma_{LA}(\Gamma)$  at the neighboring  $\vec{q}$ -points of  $\Gamma$  point for  $\text{Si}_{136-x}\text{Ge}_x$  ( $x = 8, 128$ ). These results are computed at specialized wavevector rather than  $(0,0,0)$ , due to existence of diverging mode Grüneisen parameters at  $\Gamma$  point. It is also noted that the solid and dotted lines represent linear fit for  $\frac{\Delta V}{V}$ -dependence of fractional change in mode frequency, which positive slope indicates negative  $\gamma_i(\Gamma)$ . Consequently, according to finite different approach  $\gamma_i(\vec{q}) = -(\Delta \omega_i(\vec{q}) / \Delta V) / (\omega_i(\vec{q}) / \Delta V)$ , the determined mode Grüneisen parameters are shown to be -1.51 and 0.93 for TA(1) and LA phonon at  $\Gamma$  point in  $\text{Si}_{128}\text{Ge}_8$  (-1.04 and 0.98 for  $\text{Si}_8\text{Ge}_{128}$ ).

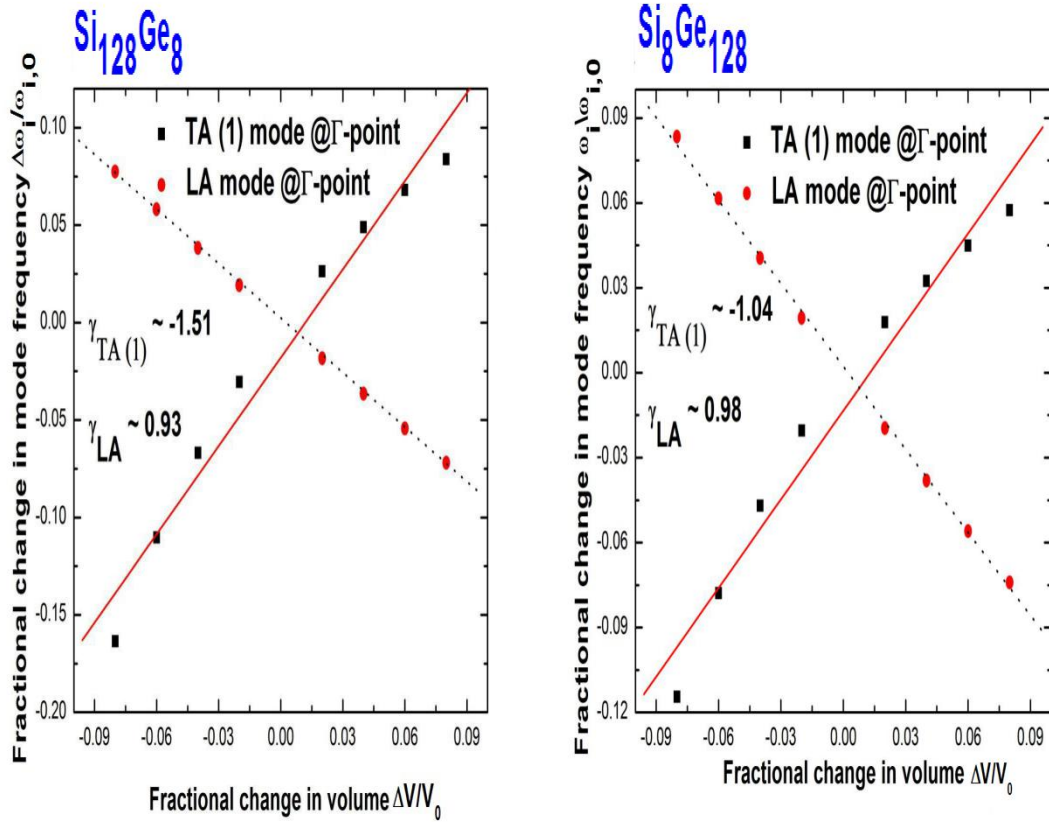


Figure 5.7: Predicted mode Grüneisen parameters in the vicinity of  $\Gamma$ -point belonging to TA(1) and LA phonon branch, in the case of  $\text{Si}_{128}\text{Ge}_8$  and  $\text{Si}_8\text{Ge}_{128}$  respectively. Results are given through finite difference method, while solid and dotted lines represent best linear fit of first-principle data.

Furthermore, following first-principles calculation (Figure 5.8) demonstrates low-frequency ( $0 - 150 \text{ cm}^{-1}$ ) band structure of phonon dispersions along the L- $\Gamma$ -X line.

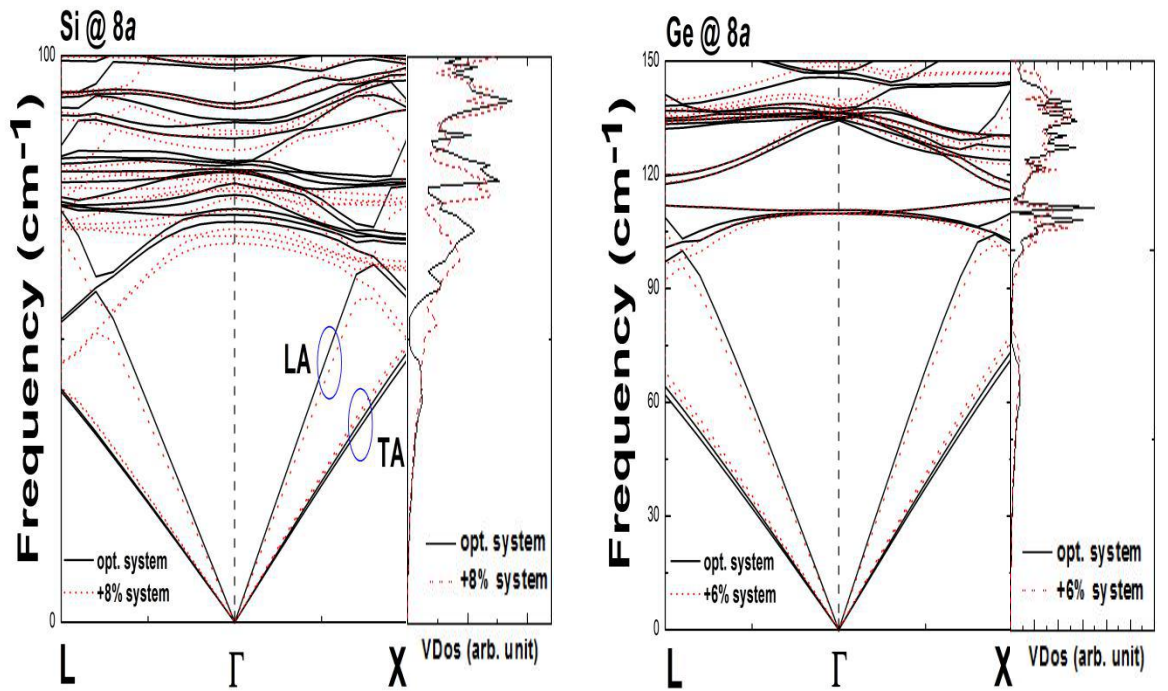


Figure 5.8: Low-frequency dispersion relation curves of  $\text{Si}_{128}\text{Ge}_8$  and  $\text{Si}_8\text{Ge}_{128}$  along L- $\Gamma$ -X line, corresponding to optimized geometry (solid line) and dilated configuration (dotted line). Meanwhile, LDA-calculated results on vibrational density of states are also shown. Circled area denotes longitudinal acoustic phonon branch as well as transverse acoustic phonon branch with double degeneracy.

To better illustrate the dilation geometry effect on lattice framework anharmonicity, our plotted phonon spectrum (dashed line) are shown using an expanded unit cell which is +8% and +6% larger than its optimized structure for comparison, concerning to  $\text{Si}_8\text{Ge}_{128}$  and  $\text{Si}_{128}\text{Ge}_8$  respectively. Otherwise, extremely low resolution of variation on  $\omega_i(\vec{q})$  is not sensitive to identify, if fractional change in equilibrium volume ( $\frac{\Delta V}{V_0}$ ) is deviated from zero to be less than 4% in the previously discussed frequency regime. It is found that, the “red-shift” for the peak of vibrational

density of states (VDOS) at about  $67 \text{ cm}^{-1}$  in expanded  $\text{Si}_{128}\text{Ge}_8$  unit cell is attributable to suppression of lowest-optic modes (TO branch). Thereby, apparent reduction of mode frequency values for degenerate TO band spanning over Brioullion zone yields positive mode Grüneisen parameters. On the other hand, elevated phonon frequency for TA branch has been obtained for enlarged geometry, in contrast to its optimized counterpart. This is an indicative of negative  $\gamma_i(\vec{q})$ , which is substantially responsible for causing low-temperature negative thermal expansion (NTE) phenomenon to be available.

One way to testify that our QHA-based approach gives rise to reliable prediction on phonon anharmonicity is characterized by isochoric specific heat:

$$C_{V,i}(\vec{q}) = k_B \frac{(\hbar\omega_i^0(\vec{q}))^2 \exp(\hbar\omega_i^0(\vec{q})/k_B T)}{(k_B T)^2 (\exp(\hbar\omega_i^0(\vec{q}) - 1))^2} \quad (5.2)$$

which summation ( $C_V(T) = \frac{1}{\rho V_0} C_{V,i}(\vec{q})$ ) excluding the  $\Gamma$ -point associated term

becomes comparable to LDA-calculated heat capacity at constant volume.  $\rho$  here

denotes the density of clathrate alloy of interest. Figure 5.9 gives our comparison

between QHA-derived specific heat ( $C_V(T) = \sum_{\vec{q},i} C_{V,i}(\vec{q})$ ) and LDA-calculated results

obtained within harmonic approximation at  $T = 0$ . Both of these two approaches

agrees extremely well with each other.

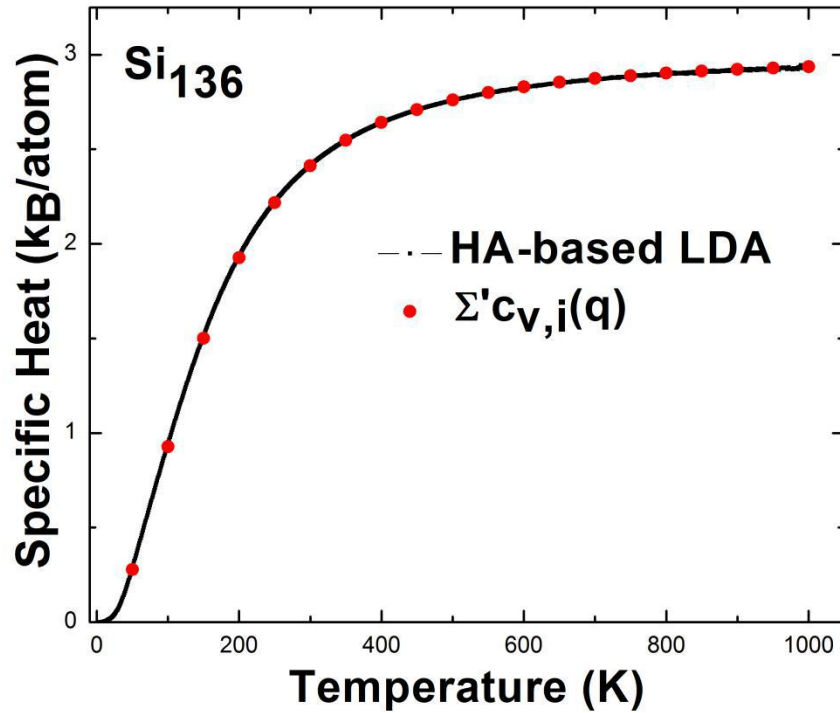


Figure 5.9: LDA-calculated specific heat and summation over mode-dependent heat capacity  $C_{v,i}(q)$ .

We decouple the effect of lowest-lying phonon branches which contribute to producing negative mode-dependent Grüneisen parameter from the contribution of all different phonon modes along all possible high symmetry directions, leading to  $\gamma_{\langle\omega\rangle}(T)$  in Figure 5.10 for  $\text{Si}_{136}$ . We found that a large contribution to low- $T$  NTE behavior arises from the soft, lowest-lying modes, in contrast to those of optic phonon modes localized within  $100\text{-}180\text{ cm}^{-1}$ . For most of the phonons lying between  $180\text{ cm}^{-1}$  and about  $500\text{ cm}^{-1}$ , the  $\gamma_i$  values are all positive but provides vanishingly small contribution to  $\gamma(T)$  due to extremely low weights.

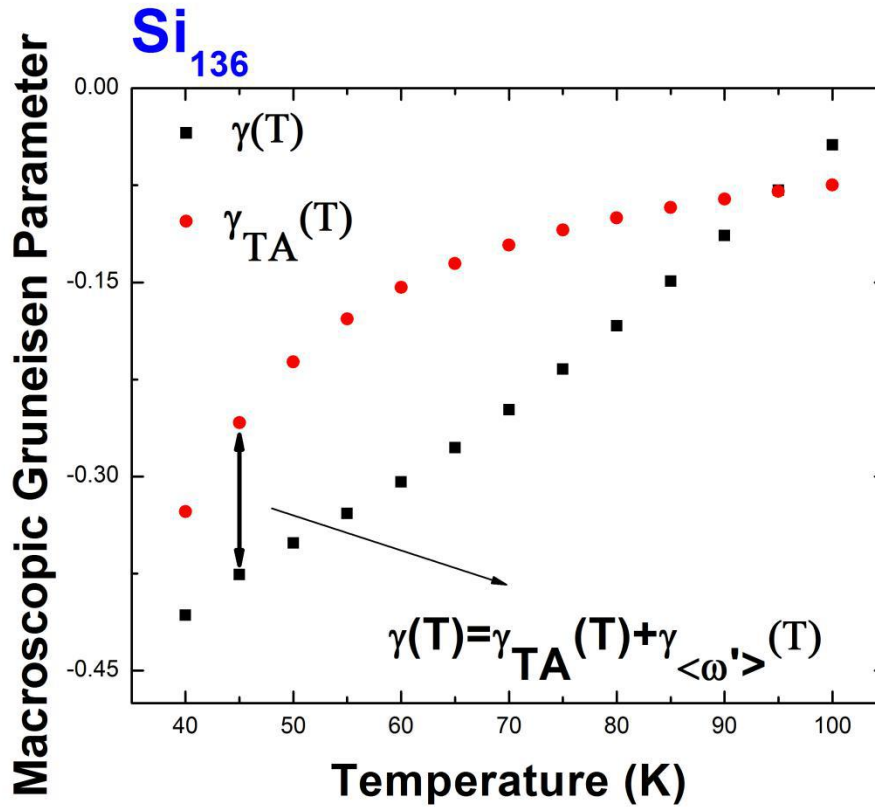


Figure 5.10: Predicted weighted Grüneisen parameter regarding to transverse acoustic phonons ( $\gamma_{TA}(T)$ ) and contribution of all phonon modes ( $\gamma(T)$ ), in terms of temperature for  $\text{Si}_{136}$ .

There exists a series of experimental method to synthesize Si-based clathrate of Type-II structure. Traditionally, thermal decomposition from the ionic Zintl phase  $\text{Na}_4\text{Si}_4$  proves to be one of the efficient ways in obtaining guest-free  $\text{Si}_{136}$ , as well as  $\text{Na}_x\text{Si}_{136}$  clathrate samples [22,23,29,30]. To capture the low- $T$  (5-300 K) thermal expansion properties of  $\text{Si}_{136}$ , J. J. Dong and X. L. Tang used powder diffractometer operated in transmission geometry to carry out the Raman measurement, for the purpose of determining lattice phonon spectra [78]. In addition, detailed experimental determination of zone-center frequencies and their pressure derivatives (referred as

mode Grüneisen parameters) of  $\text{Si}_{136}$  is given in [80]. It is found that the  $\gamma_i$  values of  $\text{Si}_{136}$  remain to be negative for TA modes along the L- $\Gamma$ -X line. Their determined MGP indicate that  $\gamma_i$  values lie within a narrow range (-1.2 to 0). On the other hand, LA and optic phonon bands show only positive MGPs. Similarly, there is some work on Raman shift of the Si-based Type-II clathrate [117,118]. The  $\gamma_i$  values predict the negative feature of acoustic phonons at the critical point  $\Gamma$ , by means of Raman scattering.

After determining the predicted  $\gamma_i$  values of TA (1) and LA phonons located within Brillouin zone boundary (L or X points) and center ( $\Gamma$  point), the Si-concentration dependence of MGP trends are displayed below. It is found that anharmonicity of TA (1) phonons is somewhat connected to producing negative  $\gamma_i$ , which values are limited to the range of -0.75 and -1.6. The calculated MGP of LA phonons at Brillouin zone boundary are approximately decreasing in a linear manner with ascending Si content. On the other hand, predicted positive  $\gamma_i$  values for LA phonons whose wavevectors are confined around Gamma point remains nearly independent of Si fraction  $x$ .

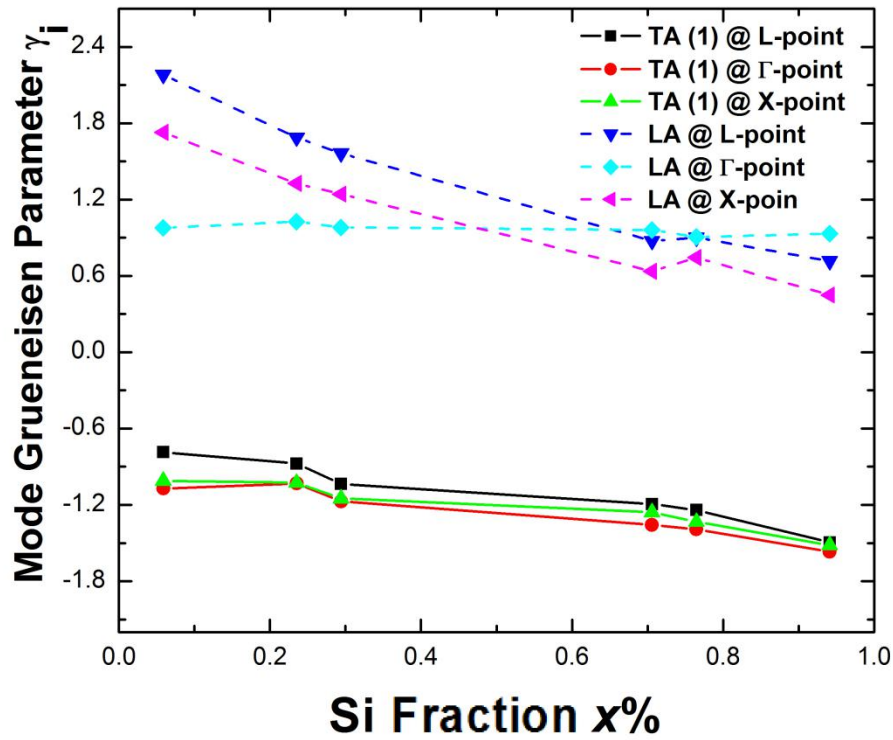


Figure 5.11: The predicted Mode Grüneisen Parameters for TA (1) and LA phonons confined at the Brillouin zone boundary and center, as a function of Si content  $x$ .

The detailed LDA determination on mode Grüneisen parameters ( $\gamma_i$ ) of specific phonon mode is listed in Table 5.1. The measured or theoretically estimated values are obtained at different points  $\Gamma$ , X, L of the dispersion curves, in the presence of different directions ( $[100]$ ,  $[111]$ ). It is noted here only the transverse acoustic phonons possess  $\gamma_i$  values that lie below zero. The calculation of  $\gamma_i$  at X and L point concerning  $\text{Si}_{128}\text{Ge}_8$  yields better agreement with the experimentally determined  $\gamma_i$  obtained for diamond-phase silicon. Meanwhile, the MGP of LA phonon at  $\Gamma$  point lies between 0.90 and 1.03 for a series of  $\text{Si}_{136-x}\text{Ge}_x$ , resulting in fair comparison with the value 1.18 determined for  $\text{Na}_1\text{Si}_{136}$  from Raman-scattering experiments. Thus

calculated results can also correlate to the value 1.1 obtained experimentally for diamond-phase silicon.

Table 5.1: Comparison of mode Grüneisen parameters between experimentally studied  $\text{Na}_1\text{Si}_{136}$  clathrate along with diamond-phase silicon [80,82] and theoretically explored  $\text{Si}_{136-x}\text{Ge}_x$  ( $8 \leq x \leq 128$ ).

Direction	Mode	Critical points	$\text{Si}_8\text{Ge}_{128}$	$\text{Si}_{32}\text{Ge}_{104}$	$\text{Si}_{40}\text{Ge}_{96}$	$\text{Na}_1\text{Si}_{136}^*$ ( $T = 298\text{K}$ )
[100]	TA (1)	X	-0.99	-1.00	-1.11	---
[111]	TA (1)	L	-0.76	-0.85	-1.00	---
	TA (1)	$\Gamma$	-1.04	-1.01	-1.14	-0.13
[100]	LA	X	1.72	1.33	1.25	---
[111]	LA	L	2.18	1.68	1.57	---
	LA	$\Gamma$	0.98	1.03	0.98	1.18

Direction	Mode	Critical points	$\text{Si}_{96}\text{Ge}_{40}$	$\text{Si}_{104}\text{Ge}_{32}$	$\text{Si}_{128}\text{Ge}_8$	$d\text{-Si}^*$ ( $T = 298\text{K}$ )
[100]	TA (1)	X	-1.22	-1.29	-1.45	-1.4
[111]	TA (1)	L	-1.16	-1.20	-1.43	-1.3
	TA (1)	$\Gamma$	-1.32	-1.35	-1.51	-0.05
[100]	LA	X	0.63	0.74	0.44	0.9
[111]	LA	L	0.87	0.90	0.71	0.9
	LA	$\Gamma$	0.96	0.90	0.93	1.1

The overall Grüneisen parameter  $\gamma(T)$  serves as a measurement of anharmonicity of lattice vibrations. Our first-principles method utilizes weighted average to obtain  $\gamma(T)$  for  $\text{Si}_{136-x}\text{Ge}_x$  ( $x = 32, 40, 96, 104$ ) in Figure 5.12, whereas  $T$  is limited to 3K and 99K. It is clearly seen that Grüneisen parameters of  $\text{Si}_{104}\text{Ge}_{32}$  and  $\text{Si}_{96}\text{Ge}_{40}$  have similar temperature profiles and are always negative from 3K to about 80K, under the circumstance of null formation of Ge-Ge bonding. On the contrary, increased number of Ge-Ge bond in  $\text{Si}_{40}\text{Ge}_{96}$  and  $\text{Si}_{32}\text{Ge}_{104}$  causes NTE effect to be

strongly weakened. Specifically, the predicted Grüneisen parameters for  $\text{Si}_{40}\text{Ge}_{96}$  and  $\text{Si}_{32}\text{Ge}_{104}$  stay negative from 3K to about 20K.

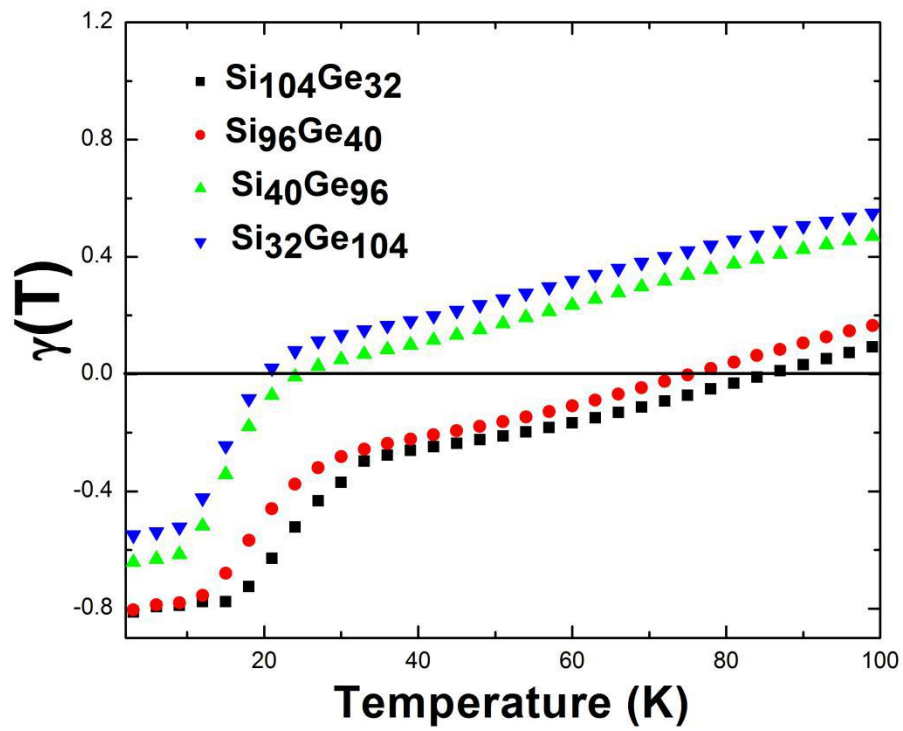


Figure 5.12: DFT-predicted Grüneisen parameters of  $\text{Si}_{104}\text{Ge}_{32}$ ,  $\text{Si}_{96}\text{Ge}_{40}$ ,  $\text{Si}_{40}\text{Ge}_{96}$ ,  $\text{Si}_{32}\text{Ge}_{104}$ .

## CHAPTER VI

### THE QHA-BASED MODE GRÜNEISEN PARAMETER ANALYSIS

#### 6.1 Summary of Negative Thermal Expansion Studies

Since the experimentally discovered negative thermal expansion (NTE) phenomenon of  $\text{ZrW}_2\text{O}_8$  in 1968 [83], abundant research efforts have been devoted to properties of these prototype materials within anomalous NTE temperature range (0 to 1080 K) [84,85]. Besides, many compounds including  $\text{PbTiO}_3$ ,  $\text{BiNiO}_3$ ,  $\text{ReO}_3$ ,  $\text{ScF}_3$ ,  $\text{HfW}_2\text{O}_8$ ,  $\text{ZrMo}_2\text{O}_8$  and etc. are found to show such unusual thermal performance [119-123]. Recent first-principles work [86] focusing on different crystalline phase of pure Si clathrate (framework I, II, IV, V, VII, VIII and H) also predicts low-temperature NTE behavior, which resembles that of diamond-phase silicon according to measurements in 1971 [124].

With the breakthrough in modern computing technique, many *ab-initio* lattice dynamics codes are developed and able to predict the unique thermal characteristics manifested by negative mode Grüneisen parameter (MGP), negative overall Grüneisen parameter, negative linear or volumetric coefficient of thermal expansion (CTE) and etc [78,86-87]. These quantities play substantial role in probing and capturing NTE which occurs within relevant temperature range to a sophisticated extent. Besides, NTE is experimentally characterized by an anharmonic effect where a material experiences contraction rather than expansion when heated to elevated temperatures. Accordingly, our implemented quasi-harmonic approximation (QHA)

scheme, combined with lattice dynamics package which employs harmonic approximation, is used to provide reasonable descriptions for NTE-related MGP and relevant thermal performances in  $\text{Si}_{136-x}\text{Ge}_x$  ( $0 \leq x < 136$ ) as long as phonon anharmonicity is weakly dependent on temperature.

Our work targets at exploring connection between low-lying acoustic phonon modes and NTE effect confined within low temperature regime ( $< 110\text{K}$ ) for  $\text{Si}_{136-x}\text{Ge}_x$  ( $0 < x < 136$ ). Motivation of our study emerges from the fact, diamond silicon is experimentally observed to display low- $T$  NTE but diamond phase germanium shows no evidence of this in  $\text{Si}_{1-x}\text{Ge}_x$  ( $0 \leq x \leq 1$ ) [124,125]. Similarly, our first-principles calculation on clathrate phase structure predicts that NTE significantly prevails in  $\text{Si}_{136-x}\text{Ge}_x$  with low concentration  $x$ . The physical origin that accounts for this is worth of detailed exploration, stimulating us to carry out our DFT study. Other related thermal properties on empty  $\text{Si}_{136}$  framework are found in [126,127]. In addition, the detailed theoretical preparation on this chapter is referred to Appendix.

## 6.2 Discussion of Thermal Performance

To theoretically understand the existence of NTE, only the static and vibrational contributions appearing in Gibbs free energy  $G$  (or Helmholtz free energy  $F$ ) are taken into consideration. On the other hand, electronic contributions are too small to be eliminated unless the high temperature scale has been approached. One way to examine the ground state properties at  $T = 0$  arises from the thermodynamics viewpoint:

$G = U - TS + PV = F + PV$ , here  $P, U, S, V$  represents pressure, internal energy, entropy and crystal volume. It is noted that Helmholtz free energy is the sum over its vibrational contribution and static contribution to internal energy:

$$F = F^{vib} + E^{static}, \quad (6.1)$$

in which the LDA-calculated  $E_{LDA}^{static}$  versus volume is fitted to a third order Birch-Murnaghan equation of state (BM-EOS) model to compute  $E^{static}$ . It is also noticed that the stably atomic structure follows from the minimum of Gibbs free energy [128]. Consequently, the volumetric coefficient of thermal expansion (VCTE) ((A.11) in Appendix) is recovered from the condition  $\frac{dG}{da} = 0$ , where  $a$  is the lattice constant corresponding to related geometry ( $a \equiv V^{1/3}$  for face center cubic structure). Our first-principles computation evaluates  $E_{LDA}^{static}$  at each optimized structure and  $T = 0$ .

Therefore, shift of LDA-determined Gibbs energy minimum towards different configuration is possible at nonzero temperature ( $T > 0$ ). Seeking new minimum lies in predominant temperature-dependent contribution to Gibbs free energy ( $-S^{vib}T$  term). This statement is valid assuming:

- (1) DFT calculations are carried out under  $P = 0$  pressure, leading to zero  $PV$  term in Gibbs free energy..
- (2)  $E^{static}$  is always set to be optimized at minimum for every geometry point, while the effect of zero-point vibrational modes is excluded from  $F^{vib}$  due to temperature-independent phonon frequency according to QHA scheme.

Therefore, the thermal expansion is understood as entropy-driven effect. It will be seen that  $-S^{vib}T$  must increase with increasing volume for NTE to occur. It is also

worthwhile to mention that the entropy-driven contribution to Gibbs free energy dominates over vibrational free energy without zero-point vibrations. Through investigation on this will be presented in the following.

Within harmonic approximation (HA), the electron ground-state energy can be evaluated as  $U^{static}\{\vec{R}_\mu\}$  for designated lattice parameter, before the dynamic matrix  $D_{\mu\nu} = d^2U^{static} / d\vec{R}_\mu d\vec{R}_\nu$  and associated phonon frequencies  $\omega_i^{HA}(\vec{q})$  are ready to determine. Additionally, the Helmholtz free energy is divided into two ingredients: the static contribution ( $U^{static}(V)$  referred to (6.1)) and vibrational contribution

$$F^{vib}(T) = \sum_{\vec{q},i} \left( \frac{1}{2} \hbar \omega_i^{HA}(\vec{q}) + k_B T \ln \left\{ 1 - \exp\left( \frac{\hbar \omega_i^{HA}(\vec{q})}{k_B T} \right) \right\} \right) \quad (6.2)$$

Figure 6.1 shows the predicted vibrational entropy which correlates to dominant temperature-dependent contribution to Gibbs free energy, at  $T = 40$  K, 80 K, 130 K, 300 K. The linearly increase behavior of  $S^{vib}$  depending on lattice volume is found in the right bottom, when  $T = 300$  K is beyond upper limit of NTE temperature range ( $\sim 120$  K) [78]. Negative slopes of upper two graphs are indicative of lattice contraction when heated from lower temperature. This is to say, there exists another way of linking variation of vibrational entropy to thermal expansion coefficient.

According to phonon mode Grüneisen parameter and Maxwell relation

$$\left( \frac{\partial P}{\partial T} \right)_V = \left( \frac{\partial S}{\partial V} \right)_T, \text{ we recover the VCTE which is proportional to sums of mode}$$

contributions to vibrational entropy:

$$\alpha_V = \frac{1}{B} \frac{\partial \left( \sum_{\vec{q},j} S_j(\vec{q}) \right)}{\partial V} \quad (6.3)$$

Our figures display macroscopic vibrational entropy  $S = \sum_{\vec{q},j} S_j(\vec{q})$ , of which calculation the wavevector sampling are spanning over 255 points within Brillouin zone for  $q$ -integration. The finer the k-points, the more reliable prediction.

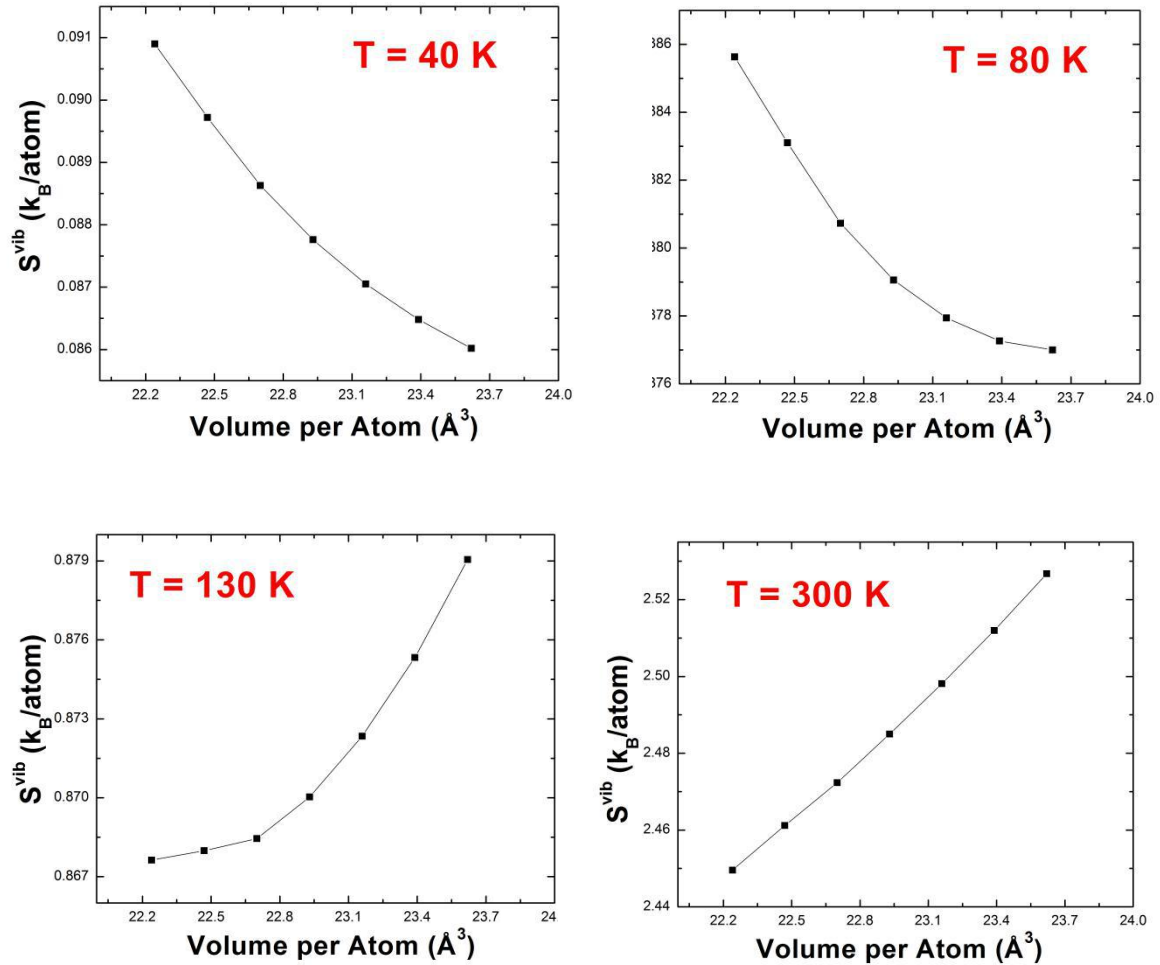
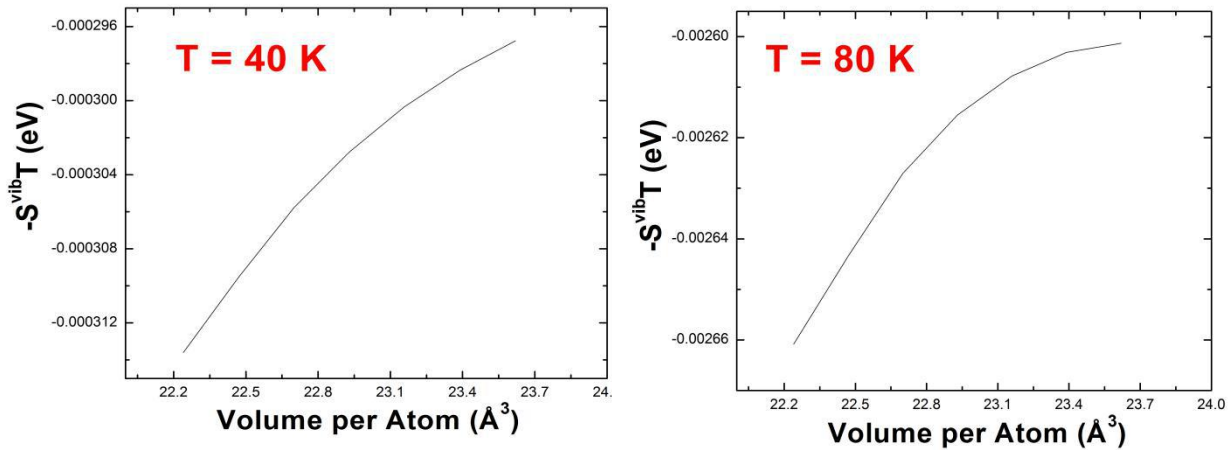


Figure 6.1: The vibrational entropy at four characteristic temperatures for alloy clathrate  $\text{Si}_{128}\text{Ge}_8$ .

Now it turns out to revisit the NTE by figuring out the entropy-driven effect.

Figure 6.2 shows a series of predicted  $-S^{\text{vib}}T$ . Among them, the slope of vibrational entropy concerning variation of lattice volume is found to be positive at  $T = 40\text{K}$ ,  $80\text{K}$ , negative at  $T = 130\text{K}$  and  $T = 300\text{K}$ . Therefore, the minimum of Gibbs free energy is shifted to a smaller value of volume at  $T = 40\text{K}$ , but to a larger value of geometry at  $T = 130\text{K}$ ,  $T = 300\text{K}$ . Slope changes its sign from positive to negative at some finite temperature between  $T = 80\text{K}$  and  $T = 130\text{K}$ , resulting in termination of NTE phenomenon. This is fair agreement with the predicted NTE temperature range ( $0 \sim 115\text{K}$ ) for  $\text{Si}_{128}\text{Ge}_8$  material after computing the overall Grüneisen parameters, and remains comparable to previous DFT data on  $\text{Si}_{136}$  [78].



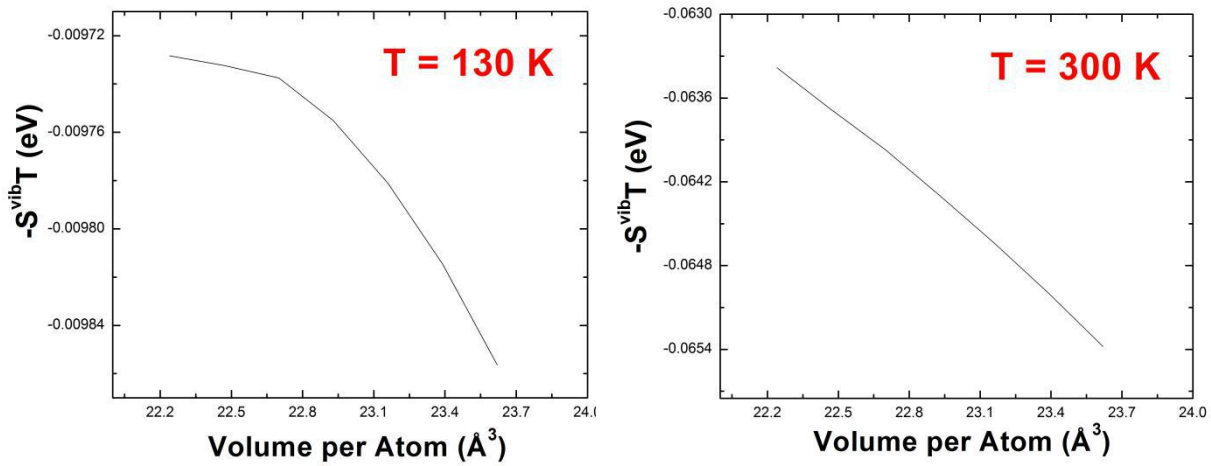


Figure 6.2: The predominant temperature-dependent contributions to Gibbs free energy per atom, at four characteristic temperatures for alloy clathrate  $\text{Si}_{128}\text{Ge}_8$ .

Using the harmonic approximation based scheme, our predicted vibrational free energy (Figure 6.3) including zero-point eigenmodes for  $\text{Si}_{136}$  is consistent with the reported result by Miranda et al. [129]. Their data emphasizes Gibbs free energy at zero pressure, making it reasonable to be compared with our calculated vibrational free energy.

We here show the thermodynamic feature lying within low-temperature regime which ranges from 10 to 400 K.

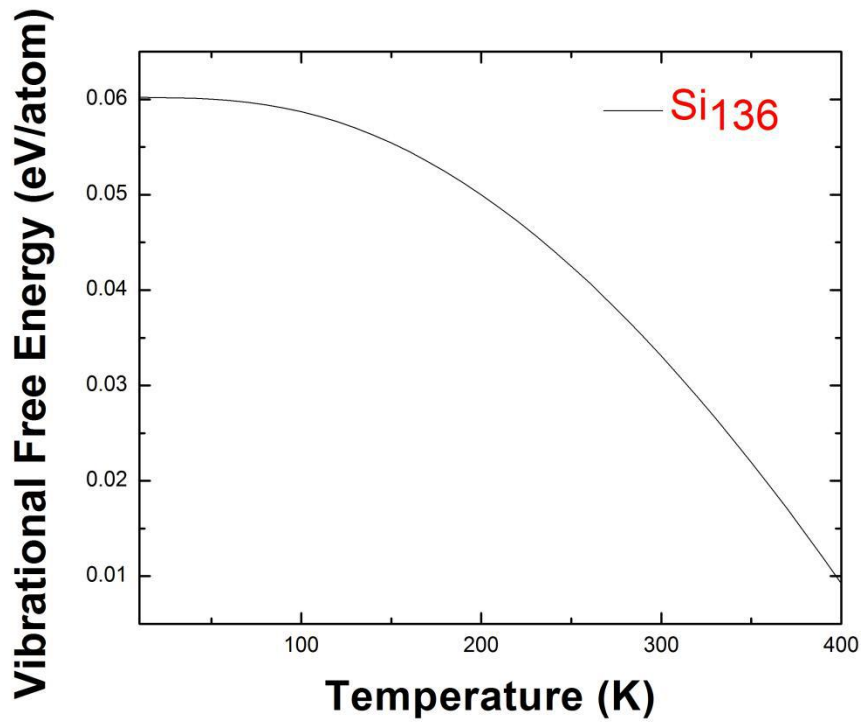


Figure 6.3: Predicted vibrational free energy including zero-point contribution for Si<sub>136</sub>, subjected to the range 10 ~ 400 K.

At present, volume derivative with respect to vibrational entropy is revisited for Si<sub>104</sub>Ge<sub>32</sub>, as is expected to possess somewhat slight NTE behavior. Figure 6.4 (a) & (b) show predicted vibrational entropy at  $T = 60$  K, 120 K. According to the slope which regulates the sign of  $\partial S / \partial V$ , it is predicted that the NTE behavior has upper limit of temperature lying within 60 K and 120 K, in the case of Si<sub>104</sub>Ge<sub>32</sub>.

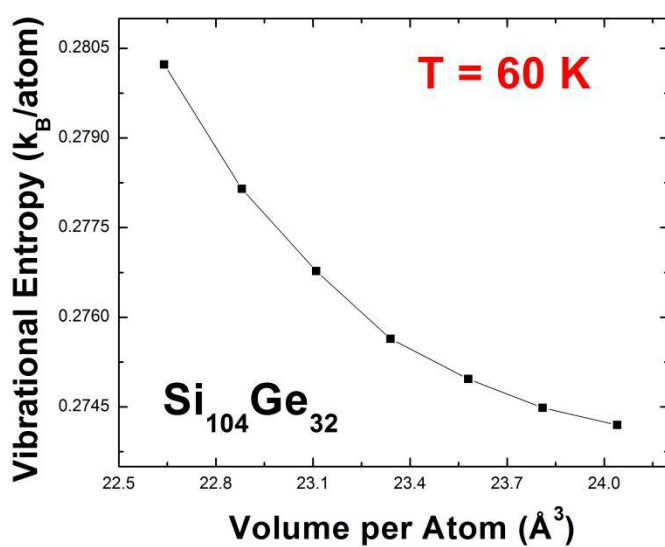


Figure 6.4(a): Predicted vibrational entropy at  $T = 60\text{ K}$  for  $\text{Si}_{104}\text{Ge}_{32}$ .

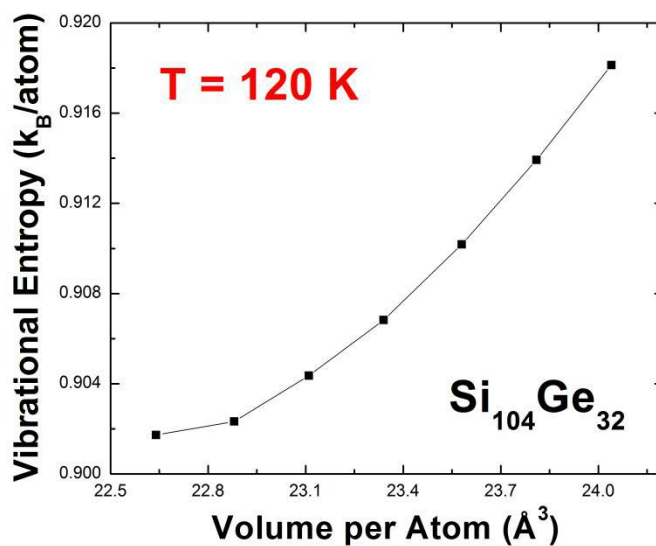


Figure 6.4(b): Predicted vibrational entropy at  $T = 120\text{ K}$  for  $\text{Si}_{104}\text{Ge}_{32}$ .

## CHAPTER VII

### ALUMINIUM AND ALKALI-DOPED TERNARY AND QUATERNARY CLATHRATE COMPOUNDS

#### 7.1 Structural, Electronic and Vibrational Study on Al-substituted Ternary Clathrate Compounds

The terminology "ternary" is traditionally from the Latin word "ternarius" which serves as an adjective meaning "composed of three items". Consequently, the so-called ternary compound refers to a chemical substance that contains three distinct elements. Within the past two decades, one has seen growing research attention in Type-II ternary clathrate [27-28,98,112,130]. Some of these work proposed by K. Biswas *et. al.* [27,28,98] emphasizes the electronic and thermal performances of  $(\text{Na},\text{K})_{16}\text{Rb}_8\text{Si}_{136}$ ,  $(\text{Rb},\text{Cs})_8\text{Ga}_8\text{Si}_{128}$  and  $\text{Na}_{16}(\text{Rb},\text{Cs})_8\text{Ge}_{136}$ , using first-principle density functional theory (DFT). There are many reasons that account for why these class of materials remain remarkably attractive. One of the primary concern might be relevant to the unique "cage-structured" framework, which is able to encapsulate guest impurity. Besides, studying semiconducting clathrate in ternary form also paves a potential way to manufacture desired thermoelectrics (TE), of which the lattice thermal conductivity is minimized via interaction between guest "rattling" and scattered, heat-carrying acoustic phonons.

From here we see, it is necessary and meaningful to theoretically explore the underlying dynamical mechanism that governs guest-framework coupling in ternary

clathrate, not only for the search of promising TE material candidate, but also for convenience and motivation of experimenter's work.

Alkaline metals are intensively studied in many types of clathrate, due to their “rattler’s” role and resonant vibration with composite atom of cage. Two kinds of encapsulated guest impurity can simultaneously exist in the same compound but from different type of polyhedral cage ( $\text{Si}_{20}/\text{Si}_{28}$ ), to tune physical and chemical properties of framework. For example, previous discussion on  $\text{Na}_{16}\text{Rb}_8\text{Si}_{136}$  and  $\text{Na}_{16}\text{Cs}_8\text{Si}_{136}$  occurs in [5,28,72,112]. Meanwhile, the gallium-substituted framework chosen to accommodate heavy guest impurity such as Rb (or Cs) has been undergoing intensive study [98]. Among them, electronic, vibrational, and thermal properties of  $\text{Na}_{16}(\text{Rb,Cs})_8\text{Ge}_{136}$  are characterized by *ab-initio* approach [102-104].

Below Table 7.1 lists LDA-calculated lattice constant, bulk modulus and cohesive energy per atom, in the case of Al-substituted and Ga-substituted ternary compounds as well as binary clathrate. Here, Ga appearing in  $(\text{Cs,Rb})_8\text{Ga}_8\text{Si}_{128}$  has  $s^2p^1$  valence electronic configuration, making it possible to behave as an electron acceptor while compensating for excess valence electron that arise from guest impurity. Semiconducting features are thus manifested due to Zintle-Klemm criteria [131]. It is similarly expected that all Al atoms subjected to their occupied  $8a$  Wyckoff sites can form Al-Si bond, in the case of  $(\text{Rb,Cs})_8\text{Al}_8\text{Si}_{128}$ . Intriguingly, our DFT work shows the entire lattice structure experiences slight expansion, when all Si atoms at  $8a$  Wyckoff sites are completely replaced by Al. From fundamental chemistry point of view, aluminum is classified as Group III element which has

reduced atomic mass (about 4% lighter than Si) and small radius. On the contrary, the lattice constant of  $\text{Cs}_8\text{Al}_8\text{Si}_{128}$  (14.676Å) is computed to remain approximately 0.64% larger than that of  $\text{Cs}_8\text{Si}_{136}$  (14.583 Å). This discrepancy on structural change is anticipated to correlate with framework bonding formation Al-Si and its impact on guest-host coupling. Our results give rise to about 41.1  $\text{cm}^{-1}$  for Cs vibration frequency in  $\text{Cs}_8\text{Al}_8\text{Si}_{128}$  (see Figure 7.1), leading to about 5.9% lower than that of Cs rattling mode in  $\text{Cs}_8\text{Si}_{136}$ . The suppressed Cs vibration frequency in Al-substituted compound is an indicative of its relatively weakly bound behavior, with respect to cage constituents. In other words, guest gets a bit larger room to move around inside the cage, resulting in geometry dilation to some extent.

Table 7.1: Equation of state (EOS) parameters obtained for filled ternary clathrate  $(\text{Rb,Cs})_8\text{Ga}_8\text{Si}_{128}$ ,  $(\text{Rb,Cs})_8\text{Al}_8\text{Si}_{128}$  and  $(\text{Cs,Rb})_8\text{Si}_{136}$ .

	$a$ (Å)	$E_0$ (eV/atom)	$K$ (Gpa)	$dK/dP$
$\text{Rb}_8\text{Al}_8\text{Si}_{128}$	14.669	-5.555	78.428	4.172
$\text{Cs}_8\text{Al}_8\text{Si}_{128}$	14.676	-5.573	80.385	3.082
$\text{Rb}_8\text{Ga}_8\text{Si}_{128}$	14.644	-5.536	79.063	5.054
$\text{Cs}_8\text{Ga}_8\text{Si}_{128}$	14.651	-5.555	79.735	4.085
$\text{Cs}_8\text{Si}_{136}$	14.583	-5.694	82.783	5.205
$\text{Rb}_8\text{Si}_{136}$	14.572	-5.681	83.115	4.955

In the same table, our results which describe structural property of Rb-containing compounds yield lattice constant of 14.670 Å and 14.644 Å for  $\text{Rb}_8\text{Al}_8\text{Si}_{128}$  and  $\text{Rb}_8\text{Ga}_8\text{Si}_{128}$  respectively. Similar to Cs-containing counterparts, structural expansion occurs again upon substitution of Group III element when all Si atoms at  $8a$  sites are replaced by Al atoms in  $\text{Rb}_8\text{Si}_{136}$ . Continuing the discussion which states

the suppressed guest vibration indirectly relates to structural expansion, it is further expected that formation of Al-Si bond other than Si-Si bond might participate in minimizing effective force constant of Rb rattler. Figure 7.1 displays localized flat bands lying in the low-frequency region, which is near  $41\text{cm}^{-1}$  for Cs vibration mode.

Accordingly, the decreased guest-host coupling is accompanied by reduced effective force constant of rattler. Using harmonic oscillator model,  $\omega = \sqrt{\phi/M}$  where  $M$  represents the mass of guest, the estimated effective force constant  $\phi$  of Cs turns out to be  $0.85\text{ eV/\AA}$  in  $\text{Cs}_8\text{Al}_8\text{Si}_{128}$  and  $0.96\text{ eV/\AA}$  for in  $\text{Cs}_8\text{Si}_{128}$ . The values of  $\phi$  for Rb in  $\text{Rb}_8\text{Al}_8\text{Si}_{128}$  (see Figure 7.2) and  $\text{Rb}_8\text{Si}_{128}$  are calculated to be  $0.31$  and  $0.46\text{ eV/\AA}$ . Further, estimation on Al-Si bond length and Si-Si bond length are based on nearest neighbouring distance table from LDA calculation. The average Al-Si bond length is computed to be  $2.42\text{ \AA}$  while average Si-Si bond length shows  $2.32\text{ \AA}$ . This difference has been identified to be relevant with structural change upon partial framework substitution.

Therefore, physical origin of lattice response upon framework substitution might be connected to the altered guest-host interaction strength due to Al-Si formation. In Figure 7.3, one of the notable features for low-frequency ( $< 200\text{ cm}^{-1}$ ) vibration spectrum appears as the non-dispersive and flat optic modes, showing nearly  $41\text{ cm}^{-1}$  and  $31\text{ cm}^{-1}$  for  $\text{Cs}_8\text{Al}_8\text{Si}_{128}$  and  $\text{Rb}_8\text{Al}_8\text{Si}_{128}$  respectively. But meanwhile, the group velocity for the lowest-lying acoustic phonons in ternary compound are almost independent of guest type, remains unaffected when compared with  $\text{Al}_8\text{Si}_{128}$ .

Numerical calculation involving diagonalization of the dynamical matrix verifies that, these localized bands are basically due to the guest motion. Comparing these low-lying optic modes to that of dispersion relation of the very right in Figure 7.3, one sees the “bending” of the acoustic branches which frequency is supposed to extend into about  $120\text{ cm}^{-1}$ . Here exists indicative of strong coupling between localized Cs (or Rb) modes and acoustic phonon bands, which carry thermal energy. Therefore, these resonant couplings are identified as “avoided-crossing effect”, allowing phonon branches of Cs(or Rb) and  $\text{Al}_8\text{Si}_{128}$  framework to meet and avoid each other near  $41\text{ cm}^{-1}$  and  $31\text{ cm}^{-1}$  in  $\text{Cs}_8\text{Al}_8\text{Si}_{128}$  and  $\text{Rb}_8\text{Al}_8\text{Si}_{128}$  material.

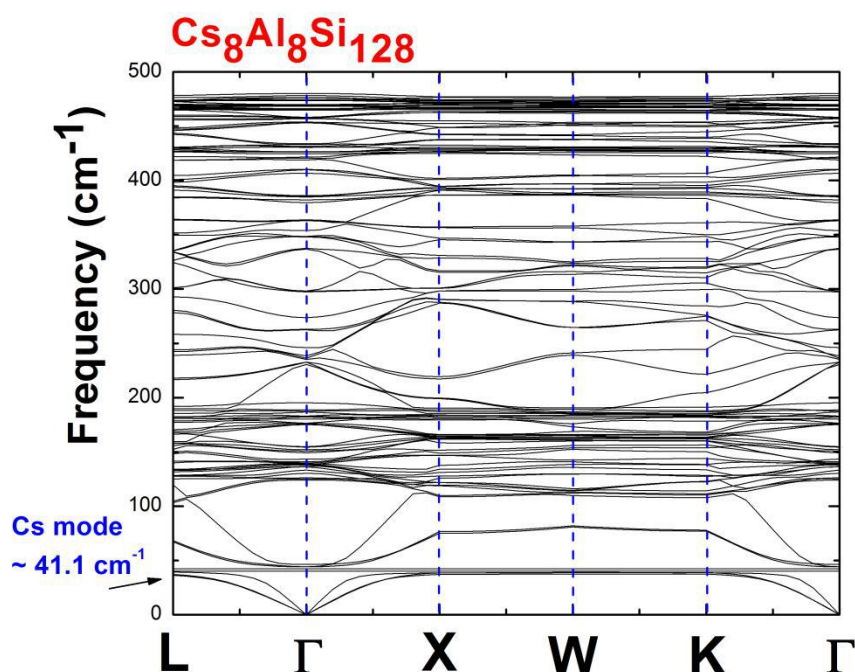


Figure 7.1: Predicted LDA-calculated phonon dispersion curves of  $\text{Cs}_8\text{Al}_8\text{Si}_{128}$ .

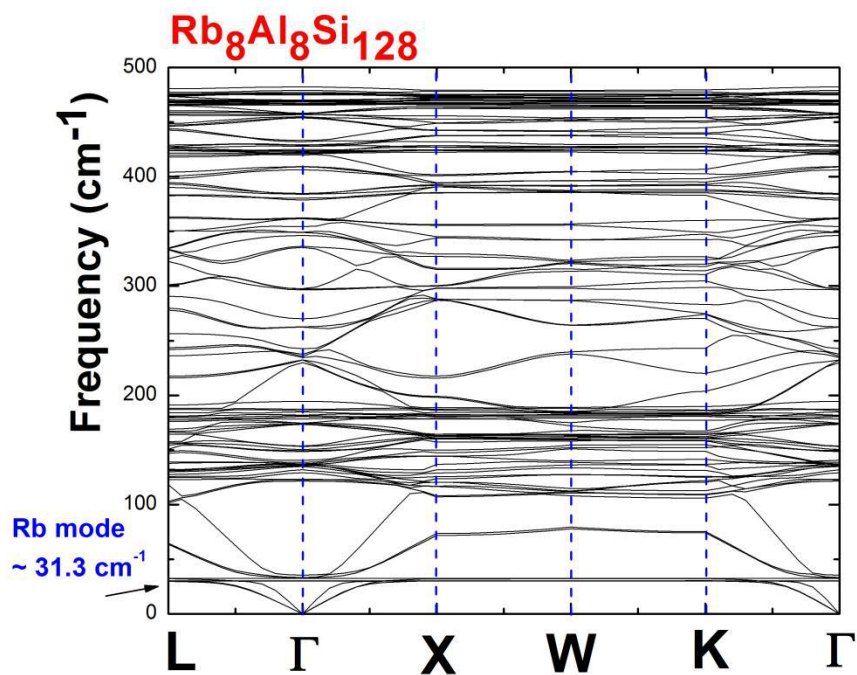


Figure 7.2: Predicted LDA-calculated phonon dispersion curves of Rb<sub>8</sub>Al<sub>8</sub>Si<sub>128</sub>.

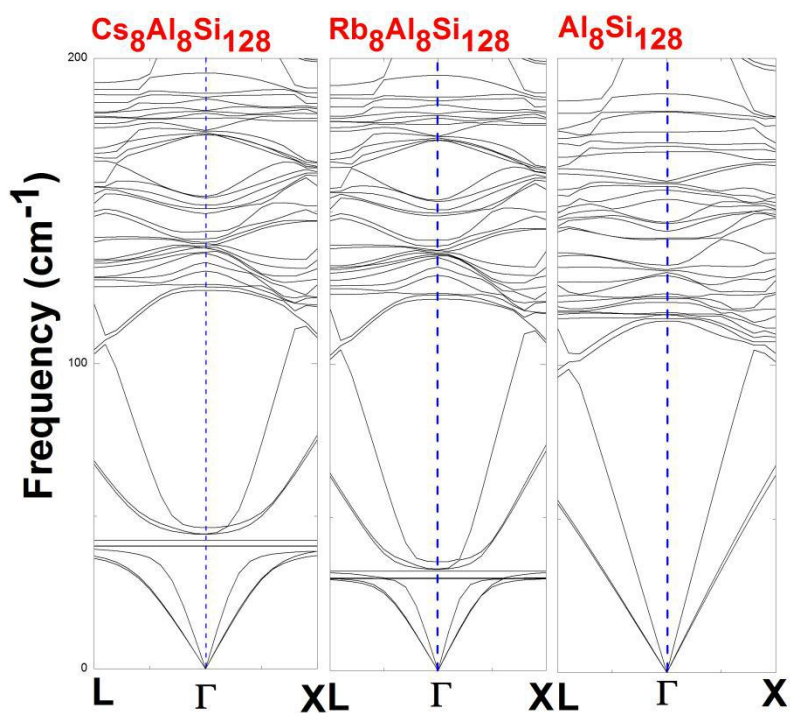


Figure. 7.3 Predicted low-frequency vibration spectrum of Cs<sub>8</sub>Al<sub>8</sub>Si<sub>128</sub>, Rb<sub>8</sub>Al<sub>8</sub>Si<sub>128</sub> and Al<sub>8</sub>Si<sub>128</sub>.

Lattice vibration contribution to thermal conductivity in some semiconducting clathrate compounds were found to play a dominant role, in comparison with relatively small electronic contribution [36,37,132]. Evaluation on electronic thermal conductivity can be facilitated by combining resistivity  $\rho$  measurements and the Wiedemann-Franz relation ( $\kappa_e = L_0 T \rho$ , where  $L_0 = 2.45 \times 10^{-8} \text{ W}\Omega\text{K}^{-2}$ ). Negligible  $\kappa_e$  is normally characterized by quite large resistivity which value remains beyond scope of  $10 \text{ m}\Omega\cdot\text{cm}$  [36,37]. For ternary clathrate  $(\text{Cs,Rb})_8\text{Al}_8\text{Si}_{128}$  of interest, only their lattice thermal conductivity is paid with essential importance here. Inspired by the suggested “rattling” model [5] where guest impurity resonantly vibrates with cage constituent, one gets familiar with the minimization of lattice thermal conductivity, which is furnished when the crystalline phonons while carrying thermal energy are scattered by a large scale of loosely bound “rattlers”. Accordingly, our estimated lattice vibration contribution to thermal conductivity are captured from simple kinetic equation  $\kappa_L = \frac{1}{3} C_v v_s \lambda$  [3], where the mean free path  $\lambda$  are taken as the separation distance between the neighboring guests encapsulated in different hexakeidacahedron cage.  $C_v$  is specific heat per unit volume and  $v_s$  appears as the isotropic sound velocity. On such basis, we predict the lattice thermal conductivity (see Table 7.2), which remains lower than experimental data of similar ternary compound  $\text{Cs}_8\text{Na}_{16}\text{Si}_{136}$ ,  $\text{Rb}_8\text{Na}_{16}\text{Si}_{136}$  [72]. To account for this increased  $\kappa_L$  arising from observed measurement, we anticipate that lattice thermal conductivity is strongly effected by avoided crossing caused by flat localized phonons rather than guest atoms serving as scattering centers. That is to say, the mean free path of acoustic phonons (TA & LA)

near the avoided-crossing point needs to be recalculated because of predominant three-phonon processes. Previously used separation of rattlers (Cs-Cs distance  $\sim 6.34$  Å) shows underestimation on mean free path. It is noted the relation  $\lambda_q = v_q \tau_q$  helps to find mean free path  $\lambda_q$  of acoustic phonons, in the presence of computed phonon lifetime  $\tau_q$  considering cubic anharmonicity due to three-phonon interaction [133]. Some reports computed  $\kappa_L$  relying on phonon lifetime of TA, LA mode are given somewhere, and their results agree quantitatively well with the experimental data [133-136].

Following figure 7.4 shows the “avoided-crossing” effect due to guest-host coupling with respect to  $\text{Cs}_8\text{Al}_8\text{Si}_{128}$  along the  $\Gamma$ -X line. The dotted lines describing dispersive LA and TA phonons of  $\text{Al}_8\text{Si}_{128}$  are also given for comparison. It is shown that those crossings due to “intersection” of flat localized Cs modes appear roughly at  $40$ - $41$   $\text{cm}^{-1}$ . Specifically, crossings of TA phonons and LA phonons occur at about  $3/5$  and  $3/10$  along the  $\Gamma$ -X line. Consequence of these “avoided-crossing” is attributable to strong interactions between acoustic phonons and rattling modes. Near the crossing point which is below optic band of Cs, group velocity of TA and LA phonons is facing substantial reduction ( $v \rightarrow 0$ ). This indicates the phonon-rattler coupling is dominantly modeled by three-phonon processes at crossings. The suggested  $\lambda_q = v_q \tau_q$  can be used to evaluate mean free path in a more reasonable way, resulting in good agreement with experimentally determined  $\kappa_L$ .

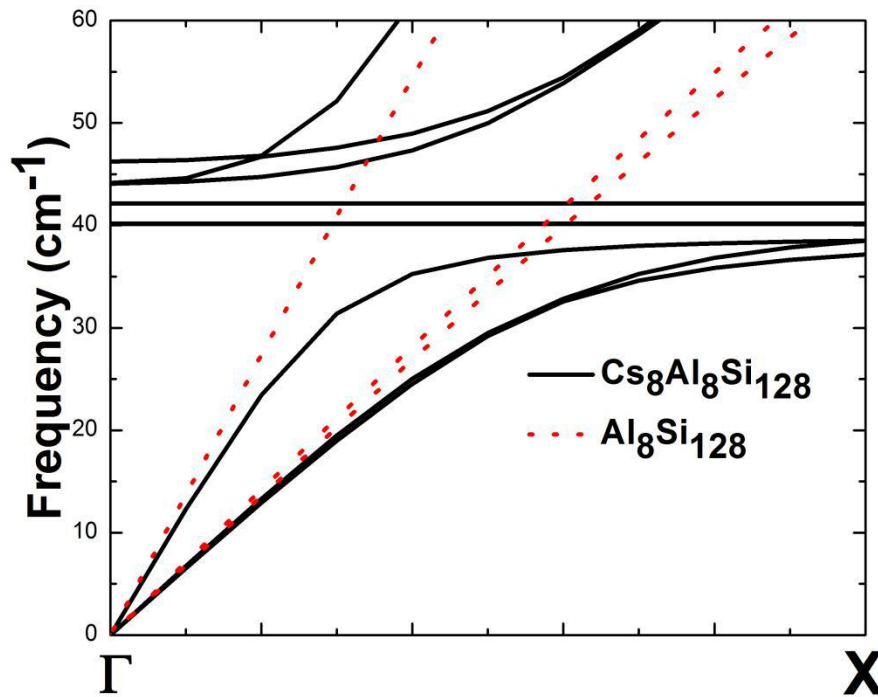


Figure 7.4: “Avoided-crossing” effect due to encapsulated Cs introduced into  $\text{Al}_8\text{Si}_{128}$ . Solid line shows low-frequency dispersion relation curves of  $\text{Cs}_8\text{Al}_8\text{Si}_{128}$  along  $\Gamma$ -X direction. Dotted lines give dispersion relation curves of  $\text{Al}_8\text{Si}_{128}$ .

Another feature regarding to guest resonant vibration is the rattler’s impact on sound velocity. It is found by our first-principles calculation that, suppressed  $v_s$  of acoustic phonons is pertinent to framework substitution upon Al which replaces Si host on  $8a$  Wyckoff sites. Meanwhile, no appreciable difference is found with group velocities of TA & LA phonons in  $\text{Cs}_8\text{Al}_8\text{Si}_{128}$  and  $\text{Rb}_8\text{Al}_8\text{Si}_{128}$ . Following table demonstrates our predicted phonon group velocity and lattice thermal conductivity for a series of clathrate compounds.

Table 7.2: LDA-performed rattling mode  $\omega$ , group velocity of TA phonons  $v_{TA}$ , group velocity of LA phonons  $v_{LA}$ , sound velocity  $v_s$ , phonon mean free path  $\lambda$  and lattice thermal conductivity  $\kappa_L$  for filled ternary clathrate  $(Rb,Cs)_8Al_8Si_{128}$ ,  $Cs_8Na_{16}Si_{136}$  and  $(Cs,Rb)_8Si_{136}$ .

	$\omega$ (cm <sup>-1</sup> )	$v_{TA}$ (m/s)	$v_{LA}$ (m/s)	$v_s$ (m/s)	$\lambda$ (Å)	$\kappa_L$ (W/m/K)
$Rb_8Al_8Si_{128}$	31.1	3010	5179	3161	6.35	1.05
$Cs_8Al_8Si_{128}$	41.1	2744	5134	3065	6.35	1.01
$Cs_8Na_{16}Si_{136}$	45.5	2728	4895	3038	6.34	1.15 (1.9*)
$Cs_8Si_{136}$	43.7	2983	5373	3322	6.31	1.10
$Rb_8Si_{136}$	37.9	3028	5496	3375	6.31	1.12

From Table 7.2, our LDA-predicted lattice thermal conductivity of  $Cs_8Na_{16}Si_{136}$  yield 1.15 W/m/K for  $Cs_8Na_{16}Si_{136}$  which stays lower than that of the experimental work (1.9 W/m/K). It is and indicative of the fact the phonon mean free path is underestimated. This induced underestimation is due to inappropriate usage of neighboring guest-guest distance (6<sup>th</sup> column of Table 7.2). As discussed in some reports [134-136], the dominant “three-phonon” processes were here proposed to govern phonon-rattling interaction due to “avoided-crossing”, leading to reasonable evaluation on mean free path. Therefore, it seems necessary to compute phonon lifetime of acoustic phonons near the avoided crossing point and to obtain more reliable estimation on  $\kappa_L$ .

7.2 The Quaternary Clathrate Compound  $\text{Cs}_8\text{Na}_{16}\text{Al}_{24}\text{Si}_{112}$ 

Quaternary clathrate  $\text{Cs}_8\text{Na}_{16}\text{Al}_{24}\text{Si}_{112}$  can be favorably formed by kinetically controlled thermal decomposition (KCTD) approach [100]. Our performed LDA work presents some structural, vibrational and thermodynamics properties of this compound for comparison. According to both Rietveld refinement and elemental analysis, the crystallographic site details about Al and atomic displacement parameter (ADPs) of Cs(Na) are measured. The suggested refinement of framework site occupancy shows Al/Si ratio values of 0.2/0.8 for  $8a$ , 0.1/0.9 for  $32e$ , and 0.2/0.8 for  $96g$  Wyckoff site. To closely simulate the occupancy of Al on these crystallographic sites using LDA approach, we testify limited number of possible ways (see Table 7.3) of arranging such substituted Group III atom. It is found that the lowest energy configuration possesses total energy of -200.68 eV per unit cell. For the most energetically stable structure of  $\text{Al}_{24}\text{Si}_{112}$  framework, we theoretically consider zero Al atoms on  $8a$  sites, while  $32e$  and  $96g$  sites are partially occupied by four and twenty Al atoms respectively. Taking the occupancy of Al on  $96g$  sites into account, our calculation shows the favored configuration that yields the highest Al/Si ratio value of 0.208/0.792.

In addition to that, the energy difference  $\Delta E$  between the lowest energy and those of remaining configurations are listed in last column of Table 7.3. Our LDA calculations on seeking the most stable configuration nearly agree fairly well with the refined data about the Al occupancy on each framework site, according to PXRD measurements [100]. The parameters in parentheses of Table 7.3 were obtained from

Rietveld refinement, characterizing crystal compositions of  $\text{Cs}_8\text{Na}_{16}\text{Al}_{24}\text{Si}_{112}$ .

Moreover, we found that decreased number of occupied 96g sites by Al element causes total energy to increase, considering last column of the table. Accordingly, structural contraction accompanied by descendant lattice constant occurs with the reduced occupancy ratio of Al/Si residing on 96g site.

Table 7.3: The occupancy of framework atoms (Al,Si) on different Wyckoff sites including 8*a*, 32*e* and 96*g*. The LDA-determined structural properties such as lattice constant, bulk modulus and energy difference between the lowest total energy of the energetically stable configuration (the second row) per unit cell and the total energy of other configuration.

8 <i>a</i> (Al1/Si1)	32 <i>e</i> (Al2/Si2)	96 <i>g</i> (Al3/Si3)	<i>a</i> (Å)	<i>K</i> (GPa)	$\Delta E$ (meV)
0/1 (0.2/0.8)*	0.125/0.875 (0.1/0.9)*	0.208/0.792 (0.2/0.8)*	14.9147 (14.9153*)	70.41	0
0/1	0.25/0.75	0.167/0.833	14.9103	70.92	157
0.5/0.5	0.25/0.75	0.125/0.875	14.8947	71.00	520
1/0	0.5/0.5	0/1	14.8861	71.35	914

We also compared our first-principle prediction on host-host (or host-guest) bond length to the XRD data. Table 7.4 shows the detailed calculation on average Si/Al-Si/Al distances as well as average Si/Al-Na distances, while taking 8*a*, 32*e* and 96*g* framework sites into consideration. The digit 1 appearing in bond length notation Si1/Al1 denotes the 8*a* site, while 2 and 3 are corresponding to 32*e* and 96*g* sites. Most of the theoretical computation and experimental results are in fair agreement with each other, except for the bond length which evaluates host-guest distance. The

disagreement can be ascribed to anharmonic effects and static disorder, in view of Na vibration within  $\text{Si}_{20}$  cage.

Table 7.4: Comparison of nearest-neighbor distances obtained by VASP with that of experimental work for  $\text{Cs}_8\text{Na}_{16}\text{Al}_{24}\text{Si}_{112}$  [100].

	Si1/Al1-Si2/Al2 (Å)	Si2/Al2-Si3/Al3 (Å)	Si3/Al3-Si3/Al3 (Å)
LDA Result	2.36-2.38	2.35-2.36	2.370-2.380
Experiment	2.415	2.389	2.398-2.445
	Si1/Al1-Na (Å)	Si2/Al2-Na (Å)	Si3/Al3-Na (Å)
LDA Result	3.10-3.35	3.26-3.48	3.31-3.61
Experiment	3.229	3.326	3.418

Our predicted thermal performance such as isotropic atomic displacement parameters (ADPs) and lattice thermal conductivity are illustrated in below figures (Figure 7.5 & Figure 7.6). The dependence on substituted Al composition of lattice thermal conductivity is given at  $T = 300$  K. It is found that overestimation on  $U_{\text{iso}}$  for quaternary compound  $\text{Cs}_8\text{Na}_{16}\text{Al}_{24}\text{Si}_{112}$  occurs between DFT-result and XRD data, making it possible to reconsider the validity of quantized harmonic oscillator model. Like what we discussed in Chapter IV, temperature-dependent quartic anharmonicity results in increased rattling frequency of guest impurity at  $T = 300\text{K}$ , leading to reduced  $U_{\text{iso}}$  value. This also accounts for deviation of rattling behavior concerning Cs from the harmonic oscillator model, in the case of  $\text{Cs}_8\text{Na}_{16}\text{Al}_{24}\text{Si}_{112}$ . In addition, the given nominal composition with respect to Al occupancy on each framework site is anticipated to influence the  $U_{\text{iso}}$  in a slight fashion.

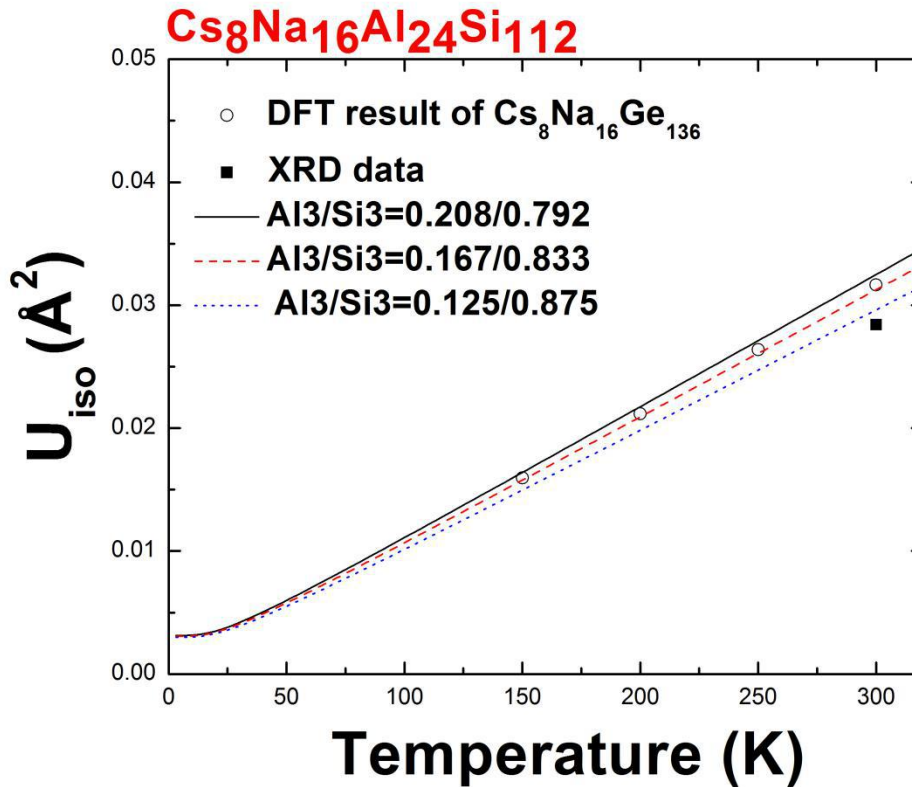


Figure 7.5: Theoretically and experimentally estimated isotropic atomic displacement parameters ( $U_{\text{iso}}$ ) of Cs in 28-cage. The open symbols represent the data corresponding to Cs vibration in  $\text{Cs}_8\text{Na}_{16}\text{Ge}_{136}$  [99]. The solid symbol denotes the measured value of  $U_{\text{iso}}$  regarding to Cs rattling in  $\text{Cs}_8\text{Na}_{16}\text{Al}_{24}\text{Si}_{112}$ .

It is noticeable that the predicted  $\kappa_L$  is not sensitive to different Al occupancy on host sites ( $8a$ ,  $32e$ ,  $96g$ ). It has been seen that the dotted line exhibits the Al3-composition independence, approximately yielding 1 W/m/K for lattice thermal conductivity. In contrast to the measured  $\kappa_L$  ( $\sim 4.5$  W/m/K) by Kaya *W. et. al.* [100], the 4-fold reduction of lattice thermal conductivity still questions the validity of “resonant” scattering model relating to acoustic phonons. Instead, the cubic anharmonicity effect needs to be reviewed in order to achieve quantitative agreement between first-principles calculation and experimentally observed  $\kappa_L$ .

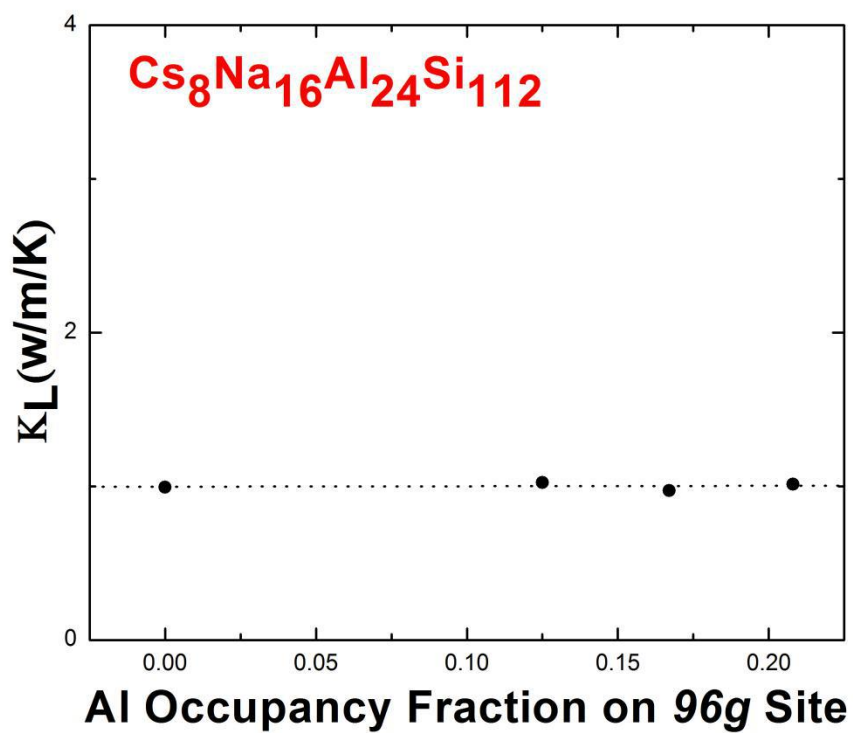


Figure 7.6: Predicted lattice thermal conductivity as a function of Al occupancy on 96g Wyckoff site. The dotted line is used for comparison.

## CHAPTER VIII

### CONCLUSIONS

Recently, intensive explorations on Type-II clathrate compounds have shown their promise role of acting as high-performance thermoelectric candidate [20-27,31-36]. Motivated by growing interest in these bulk stoichiometric materials, our work surveys several Si-based clathrates ranging from “guest-free” alloy, binary, ternary to quaternary formation. Based on unique “cage-structured” configuration studied in open framework  $\text{Si}_{136}$ ,  $\text{Ge}_{136}$ ,  $\text{Sn}_{136}$  [43,78,96], the “guest” impurity can be housed in their polyhedron, leading to many “tuned” features of clathrates from both chemical and physics point of view. Therefore, we initiated *ab initio* computations within LDA scheme to explore structural, electronic, vibrational and thermodynamic performances of some Type-II clathrate in a systematic manner.

One of the notable properties of binary clathrate  $\text{A}_x\text{Si}_{136}$  ( $\text{A}$  = alkali metal atom,  $0 < x \leq 24$ ) arises from their unique structural response upon guest filling. For instance, the lattice framework in  $\text{Na}_x\text{Si}_{136}$  is calculated to contract for  $0 < x < 8$  and expands for  $8 < x < 24$  upon Na filling. This theoretical prediction results in agreement with X-ray diffraction (XRD) data [25]. Further, to understand how “tightly” or “loosely” the sodium atom can fit inside the  $\text{Si}_{20}$  or  $\text{Si}_{28}$  polyhedron, we carried out the evaluations on “excess” radius of these cages. Consequently, performing estimation on how tight-fitting of a guest is inside “over-sized” cage (e.g.  $\text{Si}_{28}$ ) helps to review guest-host coupling strength from different perspective. Using

effective potential-energy curve to predict Na vibration in Si<sub>28</sub> cage, we point out existence of dynamically unstable state in the picture of “double-well” structure. This is also an indicative of “off-centering” displacement for guest at elevated temperatures. In addition to that, the isotropic guest vibrations are irrelevant to composition  $x$  of Na <sub>$x$</sub> Si<sub>136</sub> ( $x = 4, 8, 12, 24$ ). It is noted that the quartic anharmonicity effect induced by guest-framework interaction becomes comparably weakened, when the ratio of lowest-even anharmonic coefficient to spring constant decreases in K <sub>$x$</sub> Si<sub>136</sub>, Rb <sub>$x$</sub> Si<sub>136</sub> and Cs <sub>$x$</sub> Si<sub>136</sub> ( $0 < x \leq 24$ ).

Unlike diamond-phase silicon ( $\alpha$ -Si), “guest-free” Si<sub>136</sub> has cagelike lattice formed by dodecahedra and hexakeidacahedra connected periodically in a 4 to 2 ratio. Due to abundant first-principles and experimental studies on pristine Si<sub>136</sub>, we noticed that Si-Ge binary framework in Type-II clathrate phase serves as a new field to attract research attention. Early report suggesting germanium arrangements on  $8a, 32e, 96g$  Wyckoff sites of Si <sub>$x$</sub> Ge<sub>34- $x$</sub>  ( $x = 2, 8, 10, 24, 26, 32$ ) has been done by K. Moriguchi et al. [77]. For the same material, some structural and electronic properties obtained by our VASP-based calculation agrees quantitatively with experimental data [115] and other first-principles work [77].

We here continue to implement DFT predictions on phonon anharmonicity and thermodynamic performances, in order to explore physical origin that accounts for predicted negative thermal expansion (NTE) behavior in Si<sub>136- $x$</sub> Ge <sub>$x$</sub>  ( $0 \leq x < 136$ ). Our predicted upper temperature for NTE to occur in Si<sub>136</sub> is about 115 K, which is in good agreement with old DFT work stating about 130 K [78]. Among Si-Ge clathrate

alloys of interest,  $\text{Si}_{128}\text{Ge}_8$  is calculated to possess negative overall Grüneisen parameter  $\gamma(T)$  below about 105 K. This predicted low- $T$  NTE phenomenon is expected to be primarily attributable to negative mode Grüneisen parameters (MGPs) of phonons localized within low-frequency regime ( $\leq 75 \text{ cm}^{-1}$ ), of which the maximum has comparable temperature scale when examining upper temperature limit of NTE. Additionally, NTE effect becomes weaker and weaker when Ge fraction starts to dominate ( $\geq 70.59\%$ ) in view of  $[\text{Si}_{1-x}\text{Ge}_x]_{136}$ . This resembles the fact that, amorphous  $\text{Si}_{1-x}\text{Ge}_x$  is found to exhibit apparent NTE for  $x = 0$  but vanishing NTE for  $x = 1$  [124-125]. It is anticipated that, different number of Ge-Ge bond formation may effect the lattice geometry response upon temperature ( $0 < T \leq 120\text{K}$ ) change. In other words, the more the number of Ge-Ge bond, the weaker the NTE effect. Another developed approach to testify lattice contraction when facing elevated temperature is

to make use of thermodynamic relation  $\alpha_V \sim \left. \frac{\sum_{j,\vec{q}} \partial S_j(\vec{q})}{\partial V} \right|_T$ . It has been seen that the vibrational entropy  $S (= \sum_{j,\vec{q}} S_j(\vec{q}))$  must increase with decreasing volume for NTE to appear.

Previous DFT work [97,98] about vibrational properties of  $(\text{Rb,Cs})_8\text{Ga}_8\text{Si}_{128}$  states that Rb is more loosely bound in  $\text{Si}_{28}$  cage than Cs, although Rb is 33.3% lighter than Cs. We similarly found that vibration of Rb in Al-substituted ternary clathrate  $\text{Rb}_8\text{Al}_8\text{Si}_{128}$  produces lower rattling modes than that of Cs in  $\text{Cs}_8\text{Al}_8\text{Si}_{128}$ . It is also anticipated that Al-Si bond formation might participate in minimization of guest rattling frequency in  $(\text{Cs,Rb})_8\text{Al}_8\text{Si}_{128}$ , compared to that of  $(\text{Cs,Rb})_8\text{Si}_{136}$ . Moreover,

the validity of “resonant” rattling model where acoustic phonon can travel between neighboring scattering center to exchange thermal energy is questioned. Due to our underestimation on lattice thermal conductivity using simple kinetic theory [3], the determination on phonon mean free path needs to be reconsidered. This is to say, “avoided-crossing” effect caused by localized rattling modes and heat-carrying phonons allows us to reexamine three-phonon processes near crossings. Calculation employing recalculated mean free path  $\lambda_q = v_q \tau_q$  (phonon lifetime  $\tau_q$  depends on cubic anharmonicity) can yield reasonable agreement on lattice thermal conductivity with experimental results in some clathrates [133-135].

Adding Na atoms to fill all 20-atom cages of  $\text{Cs}_8\text{Al}_8\text{Si}_{128}$  may form semiconducting quaternary clathrate, if excess valence electrons are entirely compensated through subsequent aluminum substitution. Further, K. Wei and coworkers experimentally investigated structural, thermal and transport properties of  $\text{Cs}_8\text{Na}_{16}\text{Al}_{24}\text{Si}_{112}$  by means of XRD approach, while pointing out the refined Al occupancy regarding to framework sites [100]. In their study, suggested refinement leads to Al/Si ratio values of 0.2/0.8 for  $8a$  Wyckoff sites, 0.1/0.9 for  $32e$  Wyckoff sites and 0.2/0.8 for  $96g$  Wyckoff sites. At present, our performed LDA calculations on this quaternary clathrate initially testify some possible arrangements with respect to Al atom occupancy, which facilitates us to look for the most energetically favorable composition. Our LDA work eventually determines the optimized geometry, in which Al/Si ratio values resemble to that of experiment data discussed before. The calculated atomic displacement parameters (ADPs) of Cs for every possible

composite system  $\text{Cs}_8\text{Na}_{16}\text{Al}_{24}\text{Si}_{112}$  is larger than XRD-determined result at  $T = 300$  K. This overestimation is attributable to temperature-dependent quartic anharmonicity effect. Also, in comparison with measurement on thermal conductivity of  $\text{Cs}_8\text{Na}_{16}\text{Al}_{24}\text{Si}_{112}$ , nearly 4-fold reduction of our predicted  $\kappa_L$  is seen because of significant underestimation on phonon mean free path. Instead, computing phonon lifetime governed by three-phonon processes near crossing is preferred, yielding remodeled mean free path and lattice thermal conductivity which agrees well with experimental result.

## APPENDIX

### Theoretical Preparation on Phonon Anharmonicity

Generally speaking, harmonic approximation approach are implemented by many lattice dynamic codes, including VASP, Quantum ESPRESSO, ABINIT, WIEN2K and etc. [89-91], through retaining only the leading non-vanishing term in the expansion of the ionic interaction energy  $U$ . Meanwhile, consideration of assimilating anharmonic terms to  $U$  develops, while allowing small-oscillation assumption to prevail in order to keep only the dominant corrections to the harmonic terms in the expansion of  $U$ . Our starting point is to examine the ionic interaction energy at the ground state in the following [92]:

$$U = U_0 + U_H + U_A \quad (\text{A.1})$$

where the first two terms correspond to equilibrium potential energy and harmonic contribution to  $U$  in the spirit of dynamical variable  $\mathbf{u}(\mathbf{R})$  via following relation:

$$U_0 = \frac{N}{2} \sum \phi(\bar{\mathbf{R}}) \quad (\text{A.2})$$

$$U_H = \frac{1}{2} \sum_{\substack{\bar{\mathbf{R}}, \bar{\mathbf{R}}' \\ \mu\nu}} u_\mu(\bar{\mathbf{R}}) D_{\mu\nu}(\bar{\mathbf{R}} - \bar{\mathbf{R}}') u_\nu(\bar{\mathbf{R}}') \quad (\text{A.3})$$

$$D_{\mu\nu}(\bar{\mathbf{R}} - \bar{\mathbf{R}}') = \delta_{\bar{\mathbf{R}}, \bar{\mathbf{R}}'} \sum_{\bar{\mathbf{R}}''} \phi_{\mu\nu}(\bar{\mathbf{R}} - \bar{\mathbf{R}}'') - \phi_{\mu\nu}(\bar{\mathbf{R}} - \bar{\mathbf{R}}'), \phi_{\mu\nu}(\bar{\mathbf{r}}) = \frac{\partial^2 \phi(\bar{\mathbf{r}})}{\partial r_\mu \partial r_\nu}$$

$$U_A = \sum_{n=3}^{\infty} \frac{1}{n!} \sum_{\bar{\mathbf{R}}_1 \dots \bar{\mathbf{R}}_n} \left[ \partial^n U / \partial u_{\mu_1}(\bar{\mathbf{R}}_1) \dots \partial u_{\mu_n}(\bar{\mathbf{R}}_n) \Big|_{\bar{\mathbf{u}}=0} \right] u_{\mu_1}(\bar{\mathbf{R}}_1) \dots u_{\mu_n}(\bar{\mathbf{R}}_n) \quad (\text{A.4})$$

Here, it is necessary to mention that the force constant matrix  $D(\vec{q})$  constructed from VASP when determining vibrational frequencies is just the Fourier transform of  $D_{\mu\nu}(\vec{R} - \vec{R}')$  in real space.

Now, the lattice Hamiltonian of crystalline solid is described in terms of vibrational displacement around the lattice equilibrium positions, by means of Taylor series:

$$\begin{aligned}
H(\vec{x}_{lk_1} \cdots \vec{x}_{lk_n}) &= H(\vec{x}_{lk_1}^0 \cdots \vec{x}_{lk_n}^0) + \sum_{k_1=1}^N \sum_{l,\mu=1}^3 \left( \frac{\partial H}{\partial x_{lk_1,\mu}} \right)_0 \Delta x_{lk_1,\mu} + \frac{1}{2} \sum_{k_1,k_2=1}^N \sum_{l,l',\mu,\nu=1}^3 \left( \frac{\partial^2 H}{\partial x_{lk_1,\mu} \partial x_{l'k_2,\nu}} \right)_0 \Delta x_{lk_1,\mu} \Delta x_{l'k_2,\nu} \\
&+ \frac{1}{6} \sum_{k_1,k_2,k_3=1}^N \sum_{l,l',l'',\mu,\nu,\zeta=1}^3 \left( \frac{\partial^3 H}{\partial x_{lk_1,\mu} \partial x_{l'k_2,\nu} \partial x_{l''k_3,\zeta}} \right)_0 \Delta x_{lk_1,\mu} \Delta x_{l'k_2,\nu} \Delta x_{l''k_3,\zeta} + h.o. \quad (A.5)
\end{aligned}$$

Firstly, a crystal is composed of an infinite number of primitive unit cells in three dimensions labeled by  $l = (l_1, l_2, l_3)$  where  $l_\alpha, \alpha = 1, 2, 3$  are integers.

$\vec{x}_{lk_n}^0$  and  $\vec{x}_{lk_n}$  represent the  $n$ -th equilibrium position and displaced atomic coordinates (referred to subscript  $k_1, k_2, \dots, k_n$ ), respectively. And  $\Delta x_{lk_n,\mu} = x_{lk_n,\mu} - x_{lk_n,\mu}^0$ ,  $\mu = 1, 2, 3$  is the related component of displacement along fixed direction. Here, the  $n$ -th order atomic force constant matrix which is the so-called derivatives of the energy  $H$  reads :

$$\phi_{k_1 k_2 \cdots k_n}(\mathbf{x}_{lk_1}, \mathbf{x}_{lk_2}, \cdots, \mathbf{x}_{lk_n}) \equiv \left( \frac{\partial^n H}{\partial x_{lk_1} \partial x_{l'k_2} \cdots \partial x_{l''k_n}} \right)_0 \quad (A.6)$$

In order to construct the diagonalized dynamical matrix  $D(\vec{q})$  of direct space, one firstly carries out the second-order force constant  $\phi_{k_1 k_2}$  according to (A.6) while neglecting all odd-order anharmonic terms plus contributions from fourth and higher

order terms. In the computing scheme, VASP applies finite differences to determination of the Hessian matrix involving the second derivatives of the energy  $H$  with respect to the atomic positions ( $\phi_{k_1 k_2}$ ), within the LDA framework. It is the Fourier transform of  $\phi_{k_1 k_2}$  that gives the dynamical matrix

$$D_{\mu\nu}(\vec{q}) = \frac{1}{\sqrt{M_\mu M_\nu}} \sum_{k_1 k_2=1}^N \sum_{l, l'=1}^3 \phi_{k_1, \mu k_2, \nu} e^{-i\vec{q} \cdot (\vec{r}_{lk_1} - \vec{r}_{l'k_2})},$$
 leading to the eventually diagonalized

dynamical matrix  $D(\vec{q})$  containing  $3N$  oscillators through the calculational process:

$$\left| D_{\mu\nu}(\vec{q}) - \delta_{\mu\nu} \delta_{k_1 k_2} [\omega_i^0(\vec{q})]^2 \right| = 0 \quad (\text{A.7})$$

On the other hand, the corresponding phonon eigenvector  $\vec{e}_\mu(\vec{q})$  of the  $i$ -th oscillator ( sometimes referred as  $i$ -th phonon branch) is defined from the dispersion relation

$$[\omega_i^0(\vec{q})]^2 \vec{e}_\mu(\vec{q}) = \sum_\nu D_{\mu\nu}(\vec{q}) \vec{e}_\nu(\vec{q}), \quad (\text{A.8})$$

where  $\omega_i^0(\vec{q})$  can be related to DFT-calculated phonon frequency eigenvalues obtained by VASP, in the presence of harmonic approximation (HA) at  $T = 0$ .

### Mode Grüneisen Parameter (MGP)

To describe the thermal expansion and introduce the mode Grüneisen parameter by means of QHA method, one always concentrates on the second term including the knowledge of force constant matrix.

According to standard statistical mechanics, the volumetric coefficient of thermal expansion is existing to be valid as equilibrium volume varies with temperature at fixed pressure:

$$\alpha_V = \frac{1}{V} \left( \frac{\partial V}{\partial T} \right)_P \quad (\text{A.9})$$

But in the rigorously harmonic lattice structure, there exists absence of thermal expansion. In other words, harmonic approximation method implies that the force constant matrix  $D_{\mu\nu}(\vec{q})$  is irrelevant to volume change. Having noticed that the phonon frequencies of a real crystal do depend on the equilibrium volume, one might start with analysis on the equation of state. We adopt the definition of thermal expansion of crystal which is related by the bulk modulus  $B$  under the condition that the Gibbs free energy has achieved its minimum:

$$\left( \frac{\partial V}{\partial T} \right)_P = - \frac{(\partial P / \partial T)_V}{(\partial P / \partial V)_P} = \frac{V}{B} \left( \frac{\partial P}{\partial T} \right)_V \quad (\text{A.10})$$

On the basis of fundamental thermodynamics, the pressure is given as negative volume derivative with respect to Helmholtz free energy  $F \equiv U - TS$  at constant temperature:

$$P = - \left( \frac{\partial F}{\partial V} \right)_T \quad (\text{A.11})$$

Inserting the relation  $T \left( \frac{\partial S}{\partial T} \right)_V = \left( \frac{\partial U}{\partial T} \right)_V$  into (A.11) yields:

$$P = - \frac{\partial}{\partial V} \left[ U - T \int_0^T \frac{dT'}{T'} \frac{\partial}{\partial T'} U(T', V') \right] \quad (\text{A.12})$$

Assuming small-oscillation is always valid in a harmonic crystal, the simple classical expression for the internal energy  $U$  is shown in the harmonic approximation form [92]:

$$U = U_0 + \frac{1}{2} \sum_{\vec{q}i} \hbar \omega_i^0(\vec{q}) + \sum_{\vec{q}i} \frac{\hbar \omega_i^0(\vec{q})}{e^{\beta \hbar \omega_i^0(\vec{q})} - 1} \quad (\text{A.13})$$

Hence, recognizing the volume-dependent behavior of phonon frequency and substituting this form of internal energy into (A.12), (A.10) and (A.9), one finds that the volumetric coefficient of thermal expansion reads:

$$\alpha_V = \frac{1}{B} \left( \frac{\partial P}{\partial T} \right)_V = \frac{1}{B} \sum_{\vec{q}i} \left( -\frac{\partial}{\partial V} \hbar \omega_i^0(\vec{q}) \right) \frac{\partial}{\partial T} \left( \left[ e^{\beta \hbar \omega_i^0(\vec{q})} - 1 \right]^{-1} \right) \quad (\text{A.14})$$

Comparing above expression with the well-defined macroscopic specific heat given by

$$C_V = \sum_{\vec{q}i} \frac{\hbar \omega_i^0(\vec{q})}{V} \frac{\partial}{\partial T} \left( \left[ e^{\beta \hbar \omega_i^0(\vec{q})} - 1 \right]^{-1} \right) \quad (\text{A.15})$$

one may find the partial normal mode contributions to the specific heat

$$c_{V,i}(\vec{q}) = \frac{\hbar \omega_i^0(\vec{q})}{V} \frac{\partial}{\partial T} \left( \left[ e^{\beta \hbar \omega_i^0(\vec{q})} - 1 \right]^{-1} \right). \quad (\text{A.16})$$

After introducing the description of MGP

$$\gamma_i(\vec{q}) \equiv -\frac{V}{\omega_i^0(\vec{q})} \frac{\partial \omega_i^0(\vec{q})}{\partial V} = -\frac{\partial (\ln \omega_i^0(\vec{q}))}{\partial (\ln V)}, \quad (\text{A.17})$$

the macroscopic Grüneisen parameter is the weighted average shown in the following form

$$\gamma(T) = \frac{\sum_{\vec{q}i} \gamma_i(\vec{q}) c_{V,i}(\vec{q})}{\sum_{\vec{q}i} c_{V,i}(\vec{q})}. \quad (\text{A.18})$$

Finally, the overall Grüneisen parameter ( $\gamma(T)$ ) is related by volumetric coefficient of thermal expansion after using the quasi-harmonic approximation for atomic vibrations via the relation :

$$\alpha_V = \frac{\gamma(T)C_V}{B} \quad (\text{A.19})$$

Within our lattice dynamics code scheme, the method to calculate MGP continues

with (A.17) given by

$$\gamma_i(\vec{q}) = -\frac{V}{\omega_i^0(\vec{q})} \frac{\partial \omega_i^0(\vec{q})}{\partial V} = -\frac{V}{2[\omega_i^0(\vec{q})]^2} \left\langle e_\mu(\vec{q}) \left| \frac{\partial D(\vec{q})}{\partial V} \right| e_\mu(\vec{q}) \right\rangle \quad (\text{A.20})$$

where  $e_\mu(\vec{q})$  is the eigenvector regarding to dynamical matrix  $D(\vec{q})$ . This is then

approximated by finite difference method in order to determine the QHA-derived

MGP trends

$$\gamma_i(\vec{q}) \cong -\frac{V}{2[\omega_i^0(\vec{q})]^2} \left\langle e_\mu(\vec{q}) \left| \frac{\Delta D(\vec{q})}{\Delta V} \right| e_\mu(\vec{q}) \right\rangle \quad (\text{A.21})$$

Sophisticated computational approach typically requires three calculations at corresponding three volume points. One point is for eigenvectors at the equilibrium volume ( $V|_{T=0}$ ) while the remaining two points for  $\Delta D(\vec{q})$  with slightly larger and smaller volumes than  $V|_{T=0}$ .

As temperature approaches absolute zero ( $\beta \rightarrow \infty$ ), it is shown in (A.15) that the macroscopic heat capacity is infinitely close to zero. Thus the corresponding volumetric coefficient of thermal expansion becomes close to zero while the macroscopic Grüneisen parameter  $\gamma(T)$  remains somehow finite and non-zero, in analogy to some previously obtained experimental results [93-95]. Specifically, the finite difference method allows us to approximate  $\frac{\partial D(\vec{q})}{\partial V}$  as  $\frac{\Delta D(\vec{q})}{\Delta V}$ , while the original MGP is written as  $\gamma_i = -\frac{\partial \ln \omega_i^0(\vec{q})}{\partial \ln V}$ .

## BIBLIOGRAPHY

- [1] M. Von Stackelberg: *Feste gashydrate, Naturwiss.* **36**, p. 327-333 (1949)
- [2] J. Dong, O. F. Sankey, C. W. Myles, G. Ramachandran, P. F. McMillan, J. Gryko: *Materials Research Society Symposium.* **626** (2000) Z6.1.1
- [3] J. Dong, O. F. Sankey, C. W. Myles: *Phys. Rev. Lett.* **86** (2001) 2361
- [4] C. W. Myles, J. J. Dong, O. F. Sankey: *Proc. 3<sup>rd</sup> Motorola Workshop on Computational Materials Science.* (2002) 53
- [5] C. W. Myles, J. J. Dong, O. F. Sankey: *Physica Status Solidi B* **239** (2003) 26
- [6] M. A. Avila, K. Suekuni, K. Umeo, H. Fukuoka, S. Yamanaka, T. Takabatake: *Appl. Phys. Lett.* **92** (2008) 041901
- [7] P. Norouzzadeh, C. W. Myles, D. Vashaee: *J. Appl. Phys.* **114** (2013) 163509
- [8] D. Huo, T. Sakata, T. Sasakawa, M. A. Avila, M. Tsubota, F. Iga, H. Fukuoka, S. Yamanaka, S. Aoyagi, T. Takabatake: *Phys. Rev. B* **71** (2005) 075113
- [9] Y. Saiga, K. Suekuni, S. K. Deng, T. Yamanaka, Y. Kono, N. Ohya, T. Takabatake: *Journal of Alloys and Compounds* **507**, p. 1-5 (2010)
- [10] Norouzzadeh, C. W. Myles, D. Vashaee: *Journal of Physics: Condensed Matter* **25** (2013) 475502
- [11] S. K. Deng, Y. Saiga, K. Suekuni, T. Takabatake: *J. Appl. Phys.* **108** (2010)
- [12] R. P. Hermann, W. Schweika, O. Leupold, R. Ruffer, G. S. Nolas, F. Grandjean, G. J. Long: *Phys. Rev. B* **72** (2005) 174301
- [13] M. Imai, K. Nishida, T. Kimura, K. Yamada: *Journal of Alloys and Compounds* **335**, p. 270-276 (2002)
- [14] J. Kim, N. L. Okamoto, K. Kishida, K. Tanaka, H. Inui: *J. Appl. Phys.* **102** (2007) 094506

- [15] H. Fukuoka, K. Iwai, S. Yamanaka, H. Abe, K. Yoza, L. Hämning: *J. Solid State Chem.* **151** (2000) 117
- [16] J. S. Kasper, P. Hagenmuller, M. Pouchard, C. Cros: *Science* **150**, p.1713-1714 (1965) 3704
- [17] S. I. Kurganskii, N. A. Borshch, N. S. Pereslavitseva: *Semiconductors* **39**, p. 1218-1223 (2005) 10
- [18] G. K. Ramachandran, P. F. McMillan, J. Diefenbacher, J. Gryko, J. Dong, O. F. Sankey: *Phys. Rev. B* **60** (1999) No. 17
- [19] K. Moriguchi, M. Yonemura, A. Shintani, S. Ymanaka: *Phys. Rev. B* **61** (1999) 15
- [20] L. Qiu, M. A. White, Z. Li, J. S. Tse, C. I. Ratcliffe, C. A. Tulk, J. Dong, O. F. Sankey: *Phys. Rev. B* **64** (2001) 024303
- [21] G. K. Ramachandran, J. Dong, J. Diefenbacher, J. Gryko, R. F. Marzke, O. F. Sankey, P. F. McMillan: *J. Solid State Chem.* **145**, p. 716-730 (1999)
- [22] S. Stefanoski, C. D. Malliakas, M. G. Kanatzidis, G. S. Nolas: *Inorg. Chem.* **51**, p. 8686-8692 (2012)
- [23] J. Gryko, P. F. McMillan, R. F. Marzke, G. K. Ramachandran, D. Patton, S. K. Deb, O. F. Sankey: *Phys. Rev. B* **62** (2000) No. 12
- [24] S. Stefanoski, G. S. Nolas: *Cryst. Growth Des.* **11**, p. 4533-437 (2011)
- [25] M. Beekman, E. N. Nenghabi, K. Biswas, C. W. Myles, M. Baitinger, Y. Grin, G. S. Nolas: *Inorg. Chem.* **49**, p. 5338-5340 (2010)
- [26] J. S. Tse, K. Uehara, R. Rousseau, A. Ker, C. I. Ratcliffe, M. A. White, G. MacKay: *Phys. Rev. Lett.* **85** (2001) 114
- [27] K. Biswas, C. W. Myles: *Phys. Rev. B* **74** (2006) 115113
- [28] K. Biswas, C. W. Myles: *Phys. Rev. B* **75** (2007) 245205
- [29] S. Stefanoski, M. Beekman, W. Wong-Ng, P. Zavalij, G. S. Nolas: *Chem. Mater.* **23**, p. 1491-1495 (2011)
- [30] M. Beekman, M. Baitinger, H. Bormann, W. Schnelle, K. Meier, G. S. Nolas, Y. Grin: *J. Am. Chem. Soc.* **131** (2009) 9642

- [31] G. A. Slack: *CRC Handbook of Thermoelectrics*, p. 407-440: CRC press, Boca Raton (1995)
- [32] B. C. Sales, B. C. Chakoumakos, R. Jin, J. R. Thompson, D. Mandrus: *Phys. Rev. B* **63** (2001) 245113
- [33] G. S. Nolas, T. J. R. Weakley, J. L. Cohn, R. Sharma: *Phys. Rev. B* **61** (2000) No. 6
- [34] M. A. Avila, K. Suekuni, K. Umeo, H. Fukuoka, S. Yamanaka, T. Takabatake: *Phys. Rev. B* **74** (2006) 125109
- [35] M. Christensen, F. Juranyi, B. B. Iversen: *Physica B: Condensed Matter* **385-386**, p. 505-507 (2006)
- [36] G. S. Nolas, J. L. Cohn, G. A. Slack, S. B. Schujman: *Appl. Phys. Lett.* **73** (1998) 178
- [37] J. L. Cohn, G. S. Nolas, V. Fessatidis, T. H. Metcalf, G. A. Slack: *Phys. Rev. Lett.* **82** (1999) 779
- [38] T. M. Tritt, M. A. Subramanian: *MRS Bulletin* **31** (2006)
- [39] H. B. Callen: *Phys. Rev.* **73** (1948) No. 11
- [40] M. Tan, Y. Deng, Y. Hao: *J. Phys. Chem.* **117**, p. 20415-20420 (2013)
- [41] A. P. Goncalves, C. Godart: *Eur. Phys. J. B* **87:42** (2014)
- [42] B. Yang, P. Wang: *Thermoelectric Microcoolers*, 1<sup>st</sup> Edition, World Scientific Publishing Company, Singapore (2013)
- [43] C. W. Myles, J. Dong, O. F. Sankey, C. A. Kendziora, G. S. Nolas: *Phys. Rev. B* **65** (2002) 235208
- [44] S. Yamanaka, E. Enishi, H. Fukuoka, M. Yasukawa: *Inorg. Chem.* **39** p.56-58 (2000)
- [45] H. Fukuoka, J. Kiyoto, S. Yamanaka: *Journal of Physics and Chemistry of Solids* **65** p.333-336 (2004)
- [46] A. Kitano, K. Moriguchi, M. Yonemura, S. Munetoh, A. Shintani, H. Fukuoka, S. Yamanaka, E. Nishibori, M. Takata, M. Sakata: *Phys. Rev. B* **64** (2001) 045206

- [47] K. Kishimoto, N. Ikeda, K. Akai, T. Koyanagi: *Appl. Phys. Express* **1** (2008) 031201
- [48] H. Shimizu, Y. Takeuchi, T. Kume, S. Sasaki, K. Kishimoto, N. Ikeda, T. Koyanagi: *Journal of Alloys and Compounds* **487**, p. 47-51 (2009)
- [49] Y. Imaeda, T. Kume, S. Sasaki, H. Shimizu, K. Kishimoto, N. Ikeda, T. Koyanagi: *J. Phys.: Conf. Ser.* **377** (2012) 012037
- [50] K. Kishimoto, T. Koyanagi, K. Akai, M. Matsuura: *J. Appl. Phys.* **46**, p. 29-32 (2007)
- [51] Y. Liang, B. Böhme, M. Reibold, W. Schnelle, U. Schwarz, M. Baitinger, H. Lichte, Y. Grin: *Inorg. Chem.* **50**, p. 4523-4528 (2011)
- [52] B. Sun, X. Jia, D. Huo, X. Guo, H. Sun, Y. Zhang, B. Liu, H. Ma: *Mod. Phys. Lett. B* **29** (2015) 1550214
- [53] M. M. Shatruk, K. A. Kovnir, A. V. Shevelkov, I. A. Presniakov, B. A. Popovkin: *Inorg. Chem.* **38**, p. 3455-3457 (1999)
- [54] J. S. Tse, M. A. White: *J. Phys. Chem.* **92**, p. 5006-5011 (1988)
- [55] T. Tadano, Y. Gohda, S. Tsuneyuki: *Phys. Rev. Lett.* **114** (2015) 095501
- [56] E. N. Nenghabi, C. W. Myles: *J. Phys.: Condens. Matter* **20** (2008) 415214
- [57] W. Gou, Y. Li, J. Chi, J. H. Ross, M. Beekman, G. S. Nolas: *Phys. Rev. B* **71** (2005) 174307
- [58] R. P. Hermann, V. Keppens, P. Bonville, G. S. Nolas, F. Grandjean, G. J. Long, H. M. Christen, B. C. Chakoumakos, B. C. Sales, D. Mandrus: *Phys. Rev. Lett.* **97** (2006) 017401
- [59] G. S. Nolas, J. L. Cohn, J. S. Dyck, C. Uher, G. A. Lamberton, T. M. Tritt: *Journal of Materials Research* **19**, p. 3556-3559 (2004) 12
- [60] T. Ban, T. Ogura, Y. Ohashi, R. Himeno, F. Ohashi, T. Kume, Y. Ohya, H. Natsuhara, T. Iida, H. Habuchi, S. Nonomura: *J. Mater. Sci.* **48**, p. 989-996 (2013)
- [61] J. C. Conesa, C. Tablero, P. Wahnou: *J. Chem. Phys.* **120** (2004) 6142
- [62] C. Cros, M. Pouchard, P. Hagenmuller: *J. Solid State Chem.* **2** (1970) 570

- [63] E. Reny, P. Gravereau, C. Cros, M. Pouchard: *J. Mater.Chem.* **8** (1998) 2839
- [64] H. Horie, T. Kikudome, K. Teramura, S. Yamanaka: *J. Solid State Chem.* **182** (2009) 129
- [65] S. B. Roy, K. E. Sim, A. D. Kaplin: *Philos. Mag. B* **65** (1992) 1445
- [66] C. Kittel: *Introduction to Sol. Stat. Phys.*, 6<sup>th</sup> Edition p.76: John Wiley & Sons, New York (1986)
- [67] S. Lattner, B. B. Iversen, J. Sepa, V. Srdanov, G. Stucky: *Phys. Rev. B* **63** (2001) 125403
- [68] J. Gryko, P. F. McMillan, R. F. Marzke, A. P. Dodokin, A. A. Demkov, O. F. Sankey: *Phys. Rev. B* **57** (1998) 4172
- [69] S. Bobev, S. C. Sevov: *J. Solid State Chem.* **152** (2000) 92
- [70] C. W. Myles, J. Dong, O. F. Sankey, *Phys. Rev. B* **64** (2001) 165202
- [71] D. Xue, C. W. Myles, C.Higgins: *Materials* **9** (2016) 691
- [72] G. S. Nolas, D. G. Vanderveer, A. P. Wilkinson, J. L. Cohn: *J. Appl. Phys.* **91** (2002) 8970
- [73] M. Beekman, R. P. Hermann, A. Möchel, F. Juranyi, G. S. Nolas: *J. Phys.: Condens. Matter* **22** (2010) 355401
- [74] A. D. Ritchie, M. B. Johnson, J. F. Niven, M. Beekman, G. S. Nolas, J. Griko, M. A. White: *J. Phys.: Condes. Matter* **25** (2013) 435401
- [75] F. Tournus, B. Masenelli, P. Melinon, D. Connetable, X. Blase, A. M. Flank, P. Lagarde, C. Cros, M. Pouchard: *Phys. Rev. B* **69** (2004) 035208
- [76] H. Libotte, J. P. Gaspard, M. A. San, P. Melinon: *Euro. Phys. Lett.* **64**, p. 757-762 (2003)
- [77] K. Moriguchi, S. Munetoh, A. Shintani: *Phys. Rev. B* **62** (2000) 7138
- [78] X. Tang, J. Dong, P. Hutchins, O. Shebanova, J. Gryko, P. Barnes, J. K. Cockcroft, M. Vickers, P. F. McMillan: *Phys. Rev. B* **74** (2006) 014109
- [79] S. Wei, C. Li, M. Y. Chou: *Phys. Rev. B* **50** (1994) 14587

- [80] Y. Guyot, L. Grosvalet, B. Champagnon, E. Reny, C. Cros, M. Pouchard: *Phys. Rev. B* **60** (1999) 14507
- [81] D. Connetable: *Phys. Rev. B* **82** (2010) 075209
- [82] A. Weinstein, R. Zallen: *Topics in Applied Physics* **54**: Springer-Verlag, Berlin (1984)
- [83] C. Martinek, F. A. Hummel: *J. Am. Ceram. Soc.* **51**, p. 227-228 (1968)
- [84] J. S. O. Evans, T. A. Mary, T. Vogt, M. A. Subramanian, A. W. Sleight: *Chem. Mater.* **8** (1996) 2809
- [85] T. A. Mary, J. S. O. Evans, T. Vogt, A. W. Sleight: *Science* **272** (1996) 90
- [86] V. J. Härkönen, A. J. Karttunen: *Phys. Rev. B* **89** (2014) 024305
- [87] V. J. Härkönen, A. J. Karttunen: *Phys. Rev. B* **93** (2016) 024307
- [88] C. H. Lee, C. K. Gan: *Phys. Rev. B* **96** (2017) 035105
- [89] P. Norouzzadeh, C. W. Myles: *J. Mater. Sci.* **51**, p. 4538-4548 (2016)
- [90] Y. Takasu, T. Hasegawa, N. Ogita, M. Udagawa, M. A. Avila, K. Suekuni, I. Ishii, T. Suzuki, T. Takabatake: *Phys. Rev. B* **74** (2006) 174303
- [91] G. K. H. Madsen, A. Katre, C. Bera: *Physica Status Solidi A* **213**, p. 802-807 (2016)
- [92] N. W. Ashcroft, N. D. Mermin: *Solid State Physics*, p. 422-425, 454 (1976)
- [93] R. W. Roberts, R. Ruppin: *Phys. Rev. B* **4** (1971) No. 6
- [94] S. Tolpadi: *J. Phys. F: Metal Phys.* **4** (1974)
- [95] T. F. Smith, G. K. White: *J. Phys. C : Solid State Phys.* **8** (1975)
- [96] K. Biswas, C. W. Myles, M. Sanati, G. S. Nolas: *J. Appl. Phys.* **104** (2008) 033535
- [97] K. Biswas, C. W. Myles, *Phys. Rev. B* **75** (2007) 245205
- [98] C. W. Myles, K. Biswas, E. N. Nengahabi: *Physica B* **401** (2007) p. 695-698

- [99] K. Biswas, C. W. Myles: *J. Phys.: Condes. Matter* **19** (2007) 466206
- [100] K. Wei, Y. Dong, G. S. Nolas, *J. Solid State Chem.* **237**, p. 81-85 (2016)
- [101] T. M. Tritt: *Thermal Conductivity*, p. 118-119 (2004)
- [102] G. Kresse, J. Furthümler: *Comput. Mater. Sci.* **6** (1996) 15
- [103] G. Kresse, J. Hafner: *Phys. Rev. B* **47** (1993) 558
- [104] G. Kresse, J. Furthümler: *Phys. Rev. B* **54** (1996) 11169
- [105] F. Birch: *J. Geophys. Res.* **57** (1952)
- [106] H. J. Monkhorst, J. D. Pack: *Phys. Rev. B* **13** (1976)
- [107] J. Dong, O. F. Sankey, G. Kern: *Phys. Rev. B* **60** (1999) 950
- [108] D. M. Ceperley, B. J. Alder: *Phys. Rev. Lett.* **45** (1980) 566
- [109] N. Melnychenko-Koblyuk, A. Grytsiv, P. Rogl, M. Rotter, R. Lackner, E. Bauer, L. Fornasari, F. Marabelli, G. Giester: *Phys. Rev. B* **76** (2007) 195124
- [110] H. Zhang, *et. al.*: *Inorg. Chem.* **50(4)** (2011) p. 1250-1257
- [111] X. Zheng, S. Y. Rodriguez, J. H. Ross: *Phys. Rev. B* **84** (2001) 024303
- [112] G. S. Nolas, C. A. Kendziora, J. Gryko, J. Dong, C. W. Myles, A. Poddar, O. F. Sankey: *J. Appl. Phys.* **92** (2002) 7225
- [113] E. N. Nenghabi, C. W. Myles: *Phys. Rev. B* **78** (2008) 195202
- [114] T. Ban, *et. al.*: *J. Matter Sci.* **48** (2013) p. 989-996
- [115] L. L. Baranowski, *et. al.*: *J. Mater. Chem. C* (2014)
- [116] D. Santamaria-Perez, A. Vegas: *Acta Cryst. B* **59** (2003) p. 305-323
- [117] D. Kahn, J. P. Lu: *Phys. Rev. B* **56** (1997) 13 898
- [118] Y. Guyot, *et. al.*: *Phys. Rev. B* **57** (1998) 9475
- [119] J. Chen, *et. al.*: *Phys. Rev. Lett.* **110** (2013) 115901

- [120] T. Chatterji, P. F. Henry, R. Mittal, S. L. Chaplot: *Phys. Rev. B* **78** (2008) 134105
- [121] B. K. Greve, *et. al.*: *J. Am. Chem. Soc.* **132**(44) (2010) p. 15496-15498
- [122] J. S. O. Evans, T. A. Mary, M. A. Subramanian, A. W. Sleight: *Chem. Mater.* **8**(12) (1996) p. 2809-2823
- [123] C. Lind, A. P. Wilkinson, Z. Hu, S. Short, J. D. Jorgensen: *Chem. Mater.* **10**(9) (1998) p. 2335-2337
- [124] W. B. Gauster: *Phys. Rev. B* **4** (1971)
- [125] G. Dolling, R. A. Cowley: *Proc. Phys. Soc. Lond.* **88** (1966) 463
- [126] G. S. Nolas, M. Beekman, J. Gryko, G. A. Lamberton, T. M. Tritt, P. F. McMillan: *Appl. Phys. Lett.* **82** (2003)
- [127] A. Ammar, *et. al.*: *Solid State Sciences* **6** (2004) p. 393-400
- [128] N. W. Ashcroft, N. Mermin: *Solid State Physics* (1981)
- [129] C. R. Miranda, A. Amtonelli, *Phys. Rev. B* **74** (2006) 153203
- [130] S. Mano, T. Onimaru, S. Yamanaka, T. Takabatake: *Phys. Rev. B* **84** (2011) 214101
- [131] G. D. Hyushin: *Struct. Chem.* **23** (2012) p. 997-1043
- [132] B.C. Chakoumakos, B. C. Sales, D. G. Mandrus, G. S. Nolas: *Journal of Alloys and Compounds* **296** (2000) p.80-86
- [133] T. Tadano, S. Tsuneyuki: *Phys. Rev. Lett.* **120** (2018) 105901
- [134] H. Euchner, S. Pailhes, V. M. Giordano, M. De Boissieu: *Phys. Rev. B* **97** (2018) 014304
- [135] P. Norouzzadeh, J. S. Krasinski, T. Tadano: *Phys. Rev. B* **96** (2017) 245201
- [136] C. Chen, Z. Zhang, J. Chen: *Front. Energy Res.* **6** (2018)